High-Field Functional MRI from the Perspective of Single Vessels in Rats and Humans

Dissertation

zur Erlangung des Grades eines
Doktors der Naturwissenschaften

der Mathematisch-Naturwissenschaftlichen Fakultät
und
der Medizinischen Fakultät
der Eberhard-Karls-Universität Tübingen

vorgelegt
von

Yi He
aus Jiangxi, China

December 2017

Tag der mündlichen Prüfung : May 8th, 2018

Dekan der Math.-Nat. Fakultät : Prof. Dr. W. Rosenstiel

Dekan der Medizinischen Fakultät : Prof. Dr. I. B. Autenrieth

1. Berichterstatter : Dr. Xin Yu

2. Berichterstatter : Prof. Dr. Andreas Bartels

Prüfungskommission : Dr. Xin Yu
Prof. Dr. Andreas Bartels
Prof. Dr. Klaus Scheffler
Prof. Dr. Dr. Bernd Nürnberg

Erklärung / Declaration:

Ich erkläre, dass ich die zur Promotion eingereichte Arbeit mit dem Titel:

„High-Field Functional MRI from the Perspective of Single Vessels in Rats and Humans“

selbständig verfasst, nur die angegebenen Quellen und Hilfsmittel benutzt und wörtlich oder inhaltlich bernommene Stellen als solche gekennzeichnet habe. Ich versichere an Eides statt, dass diese Angaben wahr sind und dass ich nichts verschwiegen habe. Mir ist bekannt, dass die falsche Abgabe einer Versicherung an Eides statt mit Freiheitsstrafe bis zu drei Jahren oder mit Geldstrafe bestraft wird.

I hereby declare that I have produced the work entitled “High-Field Functional MRI from the Perspective of Single Vessels in Rats and Humans”, submitted for the award of a doctorate, on my own (without external help), have used only the sources and aids indicated and have marked passages included from other works, whether verbatim or in content, as such. I swear upon oath that these statements are true and that I have not concealed anything. I am aware that making a false declaration under oath is punishable by a term of imprisonment of up to three years or by a fine.

Tübingen, den ....
....
Datum / Date Unterschrift /Signature

Contents

1. SUMMARY

Functional MRI (fMRI) has been employed to map brain activity and connectivity based on the neurovascular coupled hemodynamic signal. However, in most cases of fMRI studies, the cerebral vascular hemodynamic signal has been imaged in a spatially smoothed manner due to the limit of spatial resolution. There is a need to improve the spatiotemporal resolution of fMRI to map dynamic signal from individual venule or individual arteriole directly. Here, the thesis aims to provide a vascular-specific view of hemodynamic response during active state or resting state. To better characterize the temporal features of task-related fMRI signal from different vascular compartments, we implemented a line-scanning method to acquire vessel-specific blood-oxygen-level-dependent (BOLD) / cerebral-blood-volume (CBV) fMRI signal at 100-ms temporal resolution with sensory or optogenetic stimulation. Furthermore, we extended the line-scanning method with multi-echo scheme to provide vessel-specific fMRI with the higher contrast-to-noise ratio (CNR), which allowed us to directly map the distinct evoked hemodynamic signal from arterioles and venules at different echo time (TE) from 3 ms to 30 ms. The line-scanning fMRI methods acquire single k-space line per TR under a reshuffled k space acquisition scheme which has the limitation of sampling the fMRI signal in real-time for resting-state fMRI studies. To overcome this, we implemented a balanced Steady-state free precession (SSFP) to map task-related and resting-state fMRI (rsfMRI) with high spatial resolution in anesthetized rats. We reveal venule-dominated functional connectivity for BOLD fMRI and arteriole-dominated functional connectivity for CBV fMRI. The BOLD signal from individual venules and CBV signal from individual arterioles show correlations at an ultra-slow frequency (< 0.1 Hz), which are correlated with the intracellular calcium signal measured in neighboring neurons. In complementary data from awake human subjects, the BOLD signal is spatially correlated among sulcus veins and specified intracortical veins of the visual cortex at similar ultra-slow rhythms. This work provides a high-resolution fMRI approach to

resolve brain activation and functional connectivity at the level of single vessels, which opened a new avenue to investigate brian functional connectivity at the scale of vessels.

2. SYNOPSIS

2.1 Introduction

2.1.1 BOLD & CBV fMRI

fMRI has been one of the most popular techniques for measuring hemodynamic responses induced by neural activity (Logothetis, 2008). The most commonly used BOLD fMRI (Bandettini et al., 1992; Kwong et al., 1992; Ogawa et al., 1992) reflects composite changes in cerebral blood flow (CBF), cerebral blood volume (CBV) and blood oxygenation (Ogawa et al., 1993). Besides the BOLD contrast, CBV coupled to neural activity can be quantified as a crucial physiological indicator by MRI with intravascular contrast agents (Mandeville, 2012; Kim et al., 2013). An agent, ultra-small super-paramagnetic iron oxide (USPIO) nanoparticles, has been widely utilized for CBV-weighted fMRI in animal studies (Chen et al., 2001; Li et al., 2005; Keilholz et al., 2006; Zhou et al., 2012; Zhao et al., 2015).

2.1.2 Functional Connectivity from Resting-State fMRI

Resting-state fMRI (rsfMRI) has been used to investigate functional connections by using synchronous spontaneous fluctuations from different regions of the brain as an indicator of synchronous neural activity (Murphy et al., 2013).

In early rsfMRI studies, the patterns of connectivity were often characterized by seed-based correlation (Biswal et al., 1995; Greicius et al., 2003; Fransson, 2005; Smitha et al., 2017), which temporally correlates the fMRI time series from one seed region with the time series from every other voxel. Another widely-used approach independent component analysis (ICA) aims at finding independent patterns in multivariate data (Beckmann et al., 2009; Smith et al., 2009; Du et al., 2015).

The Human Connectome Project (Glasser et al., 2016b) employed three complementary MR methods (task fMRI, rsfMRI, diffusion MRI) to measure brain architecture, function and connectivity (Ugurbil et al., 2013). Task-based fMRI (tfMRI) can identify functional parcellations to assist analyses of rsfMRI data (Young et al., 2014; Sair et al., 2016). Smith and colleagues employed ICA to decompose tfMRI and rsfMRI data, illustrating the close correspondence between the spatial patterns of resting and activation brain dynamics (Smith et al., 2009).

2.1.3 Spatial Specificity of High-resolution fMRI

Ultra-high-field MR (7T and above) can provide higher spatial specificity to investigate brain function with high-resolution fMRI (Harel, 2012; Ugurbil, 2014; De Martino et al., 2017). The resolutions of fMRI from 50 μm to a few 100 μm in animals and submillimeter in humans are considered high-resolution fMRI (Goense et al., 2016). High-resolution fMRI studies have demonstrated functional mapping of fine-scale organizations at the level of cortical columns (Zhao et al., 2005; Yacoub et al., 2007; Yacoub et al., 2008; Chaimow et al., 2011), cortical layers (Silva and Koretsky, 2002; Polimeni et al., 2010; Goense et al., 2012; Yu et al., 2014; Huber et al., 2017) and subcortical nuclei (Maass et al., 2015; Torrisi et al., 2015; Bianciardi et al., 2016).

In most fMRI studies, a typical voxel usually covers different vascular compartments (arteries, arterioles, venules, and veins), while high-resolution fMRI makes vascular structure distinct. By using time-of-flight MR angiography and T_2*-weighted imaging, intracortical arteries and veins were distinguished with high specificity in ultra-high magnetic fields (Bolan et al., 2006). Recently, a high-resolution fMRI study was reported to demonstrate the peak BOLD fMRI signal was primarily located at the penetrating venules in the rat somatosensory cortex. This work indicated the capabilities of high-field MRI to resolve vascular features if sufficient signal-to-noise ratio (SNR) could be achieved with high spatiotemporal resolution (Harel, 2012; Yu et al., 2012; Yu, 2017).

2.1.4 The Perspective of Single Vessels

Since fMRI signals originate from vessels, it is crucial to examine neural activity-induced hemodynamic changes in different vascular compartments (Kim et al., 2010; Kim and Ogawa, 2012). This thesis focuses on providing technical approaches for investigating the function activity and connectivity from the perspective of single vessels (Figure 1).

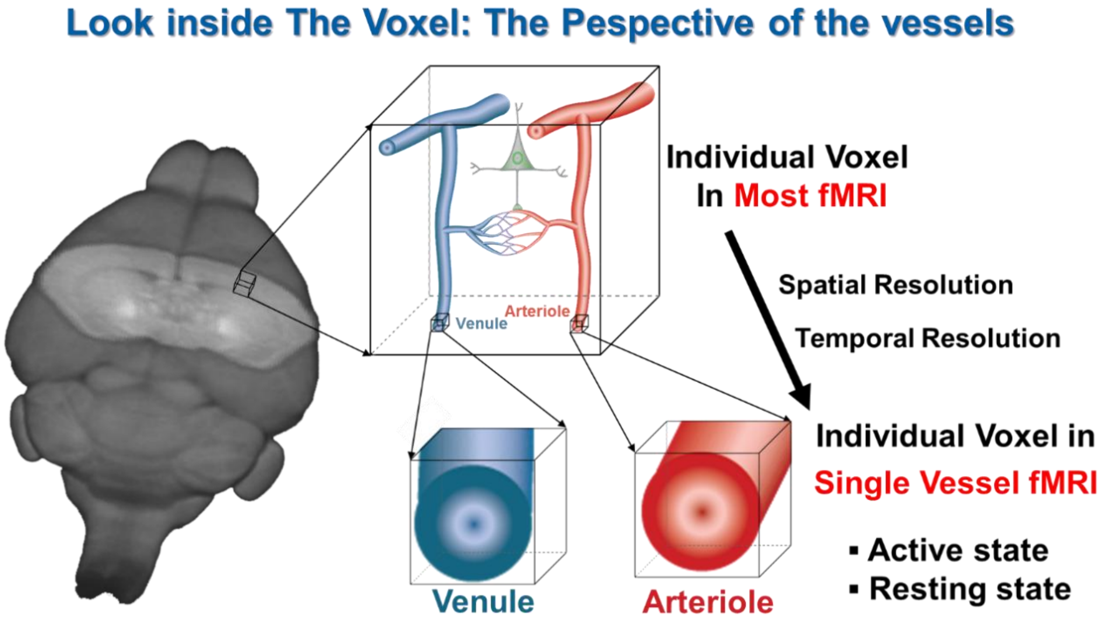

Figure 1. Look inside the voxel: The perspective of the vessels

To characterize the temporal features of fMRI at the level of single vessels, task fMRI requires both high spatial and temporal resolution. Recently, a line-scanning fMRI method was developed to characterize the temporal features of the laminar fMRI with 20 Hz sampling rate in the rat cortex (Yu et al., 2014). Here, the line-scanning method was further developed to map the sensory and optogenetically driven BOLD/CBV fMRI signals from individual arterioles and venules in the deep cortical layers (***A.1***). To improve the CNR, we extended the line-scanning method with multi-echo scheme, which allowed us to directly map the distinct evoked TE-dependent hemodynamic signal from arterioles and venules (***A.2***).

Conventionally, the temporal resolution of rsfMRI is 2 s or slower (Zalesky et al., 2014). Similarly, the high temporal resolution (subsecond) is not necessary for detecting the vessel-specific fluctuations in fMRI signals during the resting state. Here, we provide a single-vessel resting-state fMRI mapping approach (temporal resolution: 1 s) to investigate the temporal dynamic features and the spatial distribution of fluctuations in both arteriolar and venous networks of rat brain. To verify the neural basis of functional connectivity at the level of single vessels, we measured these fluctuations concurrently with calcium signal recordings from neighboring neurons. At last, the single-vessel rsfMRI mapping approach was extended to map the vessel-specific long-range correlation patterns in the gray matter of the human brain (***A.3***).

2.2 List of Papers/Manuscripts

This thesis comprises three manuscripts that are either published or under revision/re-review. Details about these manuscripts are presented in the following.

2.2.1 Summarized Papers/Manuscripts

A.1

Yu, X., **He, Y.**, Wang, M., Merkle, H., Dodd, S.J., Silva, A.C., and Koretsky, A.P.

Sensory and optogenetically driven single-vessel fMRI.

Nat Methods, 2016, 13, 337-340, doi: 10.1038/nmeth.3765.

A.2

He, Y., Wang, M., Yu, X.

Directly mapping the single-vessel hemodynamic signal with Multi-echo Line-scanning fMRI (MELS-fMRI).

Journal of Cerebral Blood Flow and Metabolism, 2017, under revision.

A.3

He, Y., Wang, M., Chen, X., Pohmann, R., Polimeni, J., Scheffler, K., Rosen, B., Kleinfeld, D. and Yu, X.

Ultra-slow single vessel BOLD and CBV-based fMRI spatiotemporal dynamics and their correlation with neuronal intracellular calcium signals.

Neuron, 2017, under re-review.

2.3 Thesis Overview

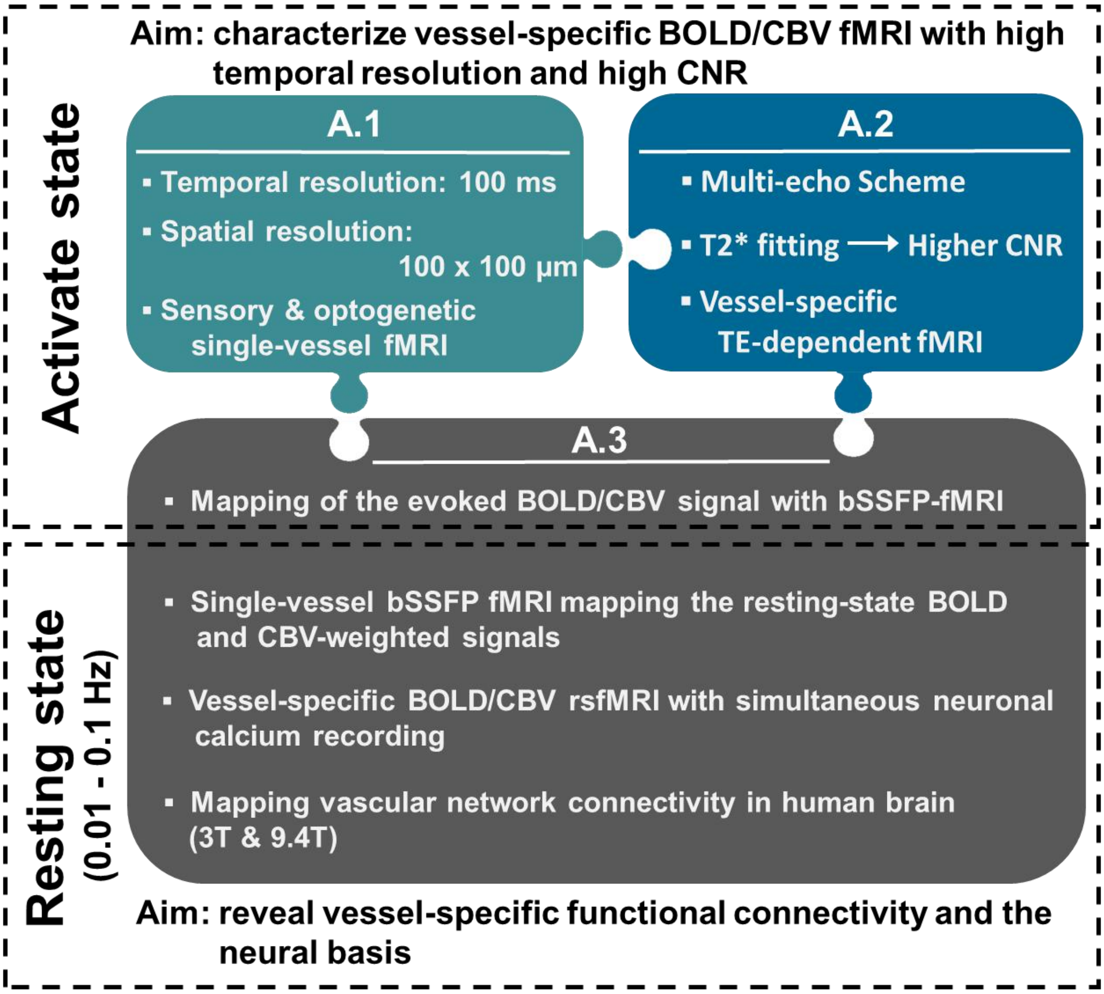

Figure 2. The overview of the thesis.

The overall goal of the thesis is to probe brain activity and connectivity from the perspective of single vessels (Figure 2). The first part of the thesis aims to characterize vessel-specific BOLD/CBV fMRI with high temporal resolution and high CNR during active state (***A.1 & A.2***). Another purpose of the thesis is to reveal vessel-specific functional connectivity during resting-state and verify the neural basis of functional connectivity at the level of single vessels (***A.3***).

2.3.1 Part one (A.1 & A.2): ultra-fast vessel-specific task fMRI

To better characterize the vascular hemodynamic signal during active state, we used a line-scanning method to acquire evoked BOLD/CBV fMRI signal with 100 ms temporal resolution and 100 μm spatial resolution. Temporal features of sensory and optogenetically driven BOLD/CBV fMRI signals were characterized in different vascular compartments (***A.1***).

To improve the contrast-to-noise ratio (CNR) of line-scanning fMRI method, we have implemented a multiple-echo scheme to develop an advanced method, called Multi-Echo Line Scanning fMRI method. The advantage of this method is to acquire fMRI signal with multi-echo which can be used to do T_2* fitting. T_2* mapping could provide a higher CNR compared with the fMRI method with one echo, which allowed us to directly map the distinct evoked hemodynamic signal from arterioles and venules at different TEs from 3 ms to 30ms with a sampling rate of 100ms. (***A.2***)

The line-scanning fMRI methods acquire single k-space line per TR under a reshuffled k space acquisition scheme. It makes it possible to sample the fMRI signal every 100ms, but it could not acquire the fMRI images in real-time for resting-state fMRI studies.

2.3.2 Part two (A.3): rsfMRI at the level of single vessels

To overcome this, we made efforts to implement a balanced Steady-state free precession (SSFP) to map the single vessel fMRI signal in 14T pre-clinical MR scanner, which allowed us to obtain task-related and resting-state fMRI signal with high spatial resolution in anesthetized rats. By using seed-based analysis method and coherence, we reveal venule-dominated functional connectivity for BOLD fMRI and arteriole-dominated functional connectivity for CBV fMRI. Meanwhile, the BOLD signal is spatially correlated among sulcus veins (3T Siemens MR) and specified intracortical veins (9.4 T Siemens MR) of the human visual cortex. To identify the basis of the vessel-specific functional connectivity, we acquired the SSFP-fMRI signal with fiber-optic calcium recording simultaneously, showing strong neuronal correlations of the low-frequency oscillation of both single-vessel fMRI and calcium signal. (***A.3***)

2.4 General Discussion

2.4.1 Technical limitations and advances

Few studies have both high temporal resolution and high spatial resolution. Kim *et al.* measured arterial CBV and total CBV changes using a single-shot EPI technique with in-plane resolution = 312 μm × 312 μm and 1-second temporal resolution (Kim and Kim, 2011). Yu *et al.* acquired the EPI fMRI images with in-plane resolution 150 × 150 μm at every 200 ms under the high field (11.7 T) (Yu et al., 2012). The peak BOLD fMRI signal was primarily located at the penetrating venules in the rat somatosensory cortex. Here, we pushed the fMRI technique to 100 ms temporal resolution and 100 × 100 μm spatial resolution.

The paramagnetic agents (iron oxides) in CBV fMRI of this work are not approved for human MRI applications (Mandeville, 2012). Vascular-Space-Occupancy (VASO) fMRI was developed to measure CBV changes in human brain without introducing paramagnetic agents (Lu et al., 2003; Huber et al., 2016). Recently, VASO fMRI on a 7T scanner was implemented to measure laminar activity and layer-dependent functional connectivity patterns in the human motor cortex, which demonstrated that laminar rsfMRI can reveal directional connectivity between brain areas (Huber et al., 2017). Here, single-vessel CBV rsfMRI has not been translated to the human brain. Future efforts will need to implement VASO fMRI in investigating arterial connectivity of human brain.

2.4.2 The neural basis of functional connectivity at the level of single vessels

We found vessel-specific fMRI signal fluctuation was correlated with ultra-slow calcium oscillation (< 0.1 Hz), which demonstrates the neural basis of functional connectivity at the level of single vessels. Previously, studies combined fMRI and electrophysiological illustrate that the resting-state fMRI signal correlates with neuronal activity oscillation (He et al., 2008; Shmuel and Leopold, 2008; Scholvinck et al., 2010; Pan et al., 2013). Here, we extended the spatial resolution of resting-state fMRI to the scale of single vessels. The coherence of the ultra-slow oscillations from both intracellular [Ca^{2+}] and vessel-specific fMRI signals demonstrates the source of vascular fluctuation is the calcium event indicating the underlying neural activity.

Particularly the BOLD signal from individual venules and the CBV signal from individual arterioles represented varied lag times relative to the calcium signal, ranging from 0.5 to 6 s. Previous studies calculated the cross-correlation of the gamma-band LFP power and the global resting-state fMRI signal, showing the neural signal led the hemodynamic signal by 5 to 6 s (Scholvinck et al., 2010). Surface draining veins dominated fluctuations caused the long lag time.

In the thesis, our high-resolution fMRI technique provides spatial specificity to demonstrate the fMRI signal from draining veins also showed longer lag time, which is consistent with the lag time between the calcium and hemoglobin signal oscillation (~ 0.1 Hz) detected from the cortical surface (Du et al., 2014). In contrast to surface draining veins, penetrating vessels at the deep cortical layers showed shorter lag times of 1.8 ± 0.2 s for the arteriole CBV signal and 2.3 ± 0.2 s for the venule BOLD signal. This result is in concordance with the signaling order of arteriole dilation followed by oxygen saturation changes in venules for neurovascular coupling (Devor et al., 2003; Iadecola, 2004).

2.5 Conclusion and Outlook

In this thesis, we provided a high spatial-temporal resolution fMRI approach for mapping vessel-specific hemodynamic signal at 10 Hz sampling rate with sensory or optogenetic stimulation. The temporal features of evoked BOLD/CBV fMRI were characterized in different distinct vasculature with high spatial specificity. Furthermore, we revealed venule-dominated functional connectivity for BOLD fMRI and arteriole-dominated functional connectivity for CBV fMRI in anesthetized rats. Meanwhile, we translated functional connectivity at the level of single vessels to human visual cortex, illustrating that the BOLD signal is spatially correlated among sulcus veins and specified intracortical veins. The simultaneous SSFP-fMRI with fiber-optic calcium recording demonstrated vessel-specific fluctuations during the resting state are correlated with the intracellular calcium signal measured in neighboring neurons. Overall, we have provided researchers two complementary approaches (ultra-fast vessel-specific task fMRI, rsfMRI at the level of single vessels) for investigating the brain activity and connectivity from the perspective of single vessels.

Many studies have made efforts in developing clinical applications of fMRI, such as guiding diagnosis, clinical management (Matthews et al., 2006; Lee et al., 2013; Pievani et al., 2014; Dickerson et al., 2016; Matthews and Hampshire, 2016). Initially, localization of brain activation by task fMRI was applied to be an adjunctive diagnosis to support neurosurgical resection planning in epilepsy or brain tumors (Haberg et al., 2004; Pittau et al., 2014). As a complementary approach of task fMRI, rsfMRI was cooperated to improve the assessment of the sensorimotor area in subjects with brain tumors (Kokkonen et al., 2009) and the epileptogenic zone in patients with epilepsy (Bettus et al., 2010). Further, several rsfMRI studies have demonstrated functional connectivity as the potential biomarkers for degenerative diseases (Zhou et al., 2010; Binnewijzend et al., 2012; Pievani et al., 2014; Guo et al., 2016) and the evaluation approach for treatment in stroke patients (Park et al., 2011; Dacosta-Aguayo et al., 2014). By taking advantage of the spatial specificity of high-resolution fMRI, future studies need to integrate vessel-specific brain activity and functional connectivity at the level of single vessels to link vascular biomarkers with dynamic indicators in patients with cerebral small vessel diseases or degenerative diseases.

There is a growing trend in integrating multi-modal and multi-scale MRI to examine how the brain works (Zhu and Majumdar, 2014; Jung et al., 2016; Masch et al., 2016; Reid et al., 2017; Van den Heuvel and Yeo, 2017). The recent study from the Allen Institute for Brain Science presented a highly detailed human brain atlas, incorporating multi-modal ex vivo information from diffusion MRI and structural MRI of a post-mortem female brain, high-resolution histology, microscale cellular Nissl and immunohistochemistry staining (Ding et al., 2016). Glasser and colleagues (Glasser et al., 2016a) provided a multi-modal parcellation of human cerebral cortex in vivo by combining multiple properties at the macroscale level (cortical function using task fMRI, function connectivity from rsfMRI, cortical thickness) and microscale level (myelin maps derived from T1-weighted and T2-weighted structural imaging). They trained a machine-learning classifier to identify 180 (97 new areas) cortical regions, demonstrating the power of integrating multi-modal MRI. In future, we will make the efforts to combine ultra-fast vessel-specific task fMRI, functional connectivity at the level of single vessels, calcium imaging with other complementary information (myelin imaging, diffusion-weighted imaging) to probe the healthy and diseased brain structure, function and metabolism.

2.6 References

Bandettini, P.A., Wong, E.C., Hinks, R.S., Tikofsky, R.S., and Hyde, J.S. (1992). Time course EPI of human brain function during task activation. Magn Reson Med 25, 390-397.

Beckmann, C.F., Mackay, C.E., Filippini, N., and Smith, S.M. (2009). Group comparison of resting-state FMRI data using multi-subject ICA and dual regression. NeuroImage 47, S148.

Bettus, G., Bartolomei, F., Confort-Gouny, S., Guedj, E., Chauvel, P., Cozzone, P.J., Ranjeva, J.P., and Guye, M. (2010). Role of resting state functional connectivity MRI in presurgical investigation of mesial temporal lobe epilepsy. J Neurol Neurosur Ps 81, 1147-1154.

Bianciardi, M., Toschi, N., Eichner, C., Polimeni, J.R., Setsompop, K., Brown, E.N., Hamalainen, M.S., Rosen, B.R., and Wald, L.L. (2016). In vivo functional connectome of human brainstem nuclei of the ascending arousal, autonomic, and motor systems by high spatial resolution 7-Tesla fMRI. Magn Reson Mater Phy 29, 451-462.

Binnewijzend, M.A.A., Schoonheim, M.M., Sanz-Arigita, E., Wink, A.M., van der Flier, W.M., Tolboom, N., Adriaanse, S.M., Damoiseaux, J.S., Scheltens, P., van Berckel, B.N.M., and Barkhof, F. (2012). Resting-state fMRI changes in Alzheimer's disease and mild cognitive impairment. Neurobiol Aging 33, 2018-2028.

Biswal, B., Yetkin, F.Z., Haughton, V.M., and Hyde, J.S. (1995). Functional connectivity in the motor cortex of resting human brain using echo-planar MRI. Magn Reson Med 34, 537-541.

Bolan, P.J., Yacoub, E., Garwood, M., Ugurbil, K., and Harel, N. (2006). In vivo micro-MRI of intracortical neurovasculature. NeuroImage 32, 62-69.

Chaimow, D., Yacoub, E., Ugurbil, K., and Shmuel, A. (2011). Modeling and analysis of mechanisms underlying fMRI-based decoding of information conveyed in cortical columns. NeuroImage 56, 627-642.

Chen, Y.C.I., Mandeville, J.B., Nguyen, T.V., Talele, A., Cavagna, F., and Jenkins, B.G. (2001). Improved mapping of (pharmacologically induced neuronal activation using the IRON technique with superparamagnetic blood pool agents. J Magn Reson Imaging 14, 517-524.

Dacosta-Aguayo, R., Grana, M., Savio, A., Fernandez-Andujar, M., Millan, M., Lopez-Cancio, E., Caceres, C., Bargallo, N., Garrido, C., Barrios, M., *et al.* (2014). Prognostic Value of Changes in Resting-State Functional Connectivity Patterns in Cognitive Recovery After Stroke: A 3T fMRI Pilot Study. Hum Brain Mapp 35, 3819-3831.

De Martino, F., Yacoub, E., Kemper, V., Moerel, M., Uludag, K., De Weerd, P., Ugurbil, K., Goebel, R., and Formisano, E. (2017). The impact of ultra-high field MRI on cognitive and computational neuroimaging. NeuroImage.

Devor, A., Dunn, A.K., Andermann, M.L., Ulbert, I., Boas, D.A., and Dale, A.M. (2003). Coupling of total hemoglobin concentration, oxygenation, and neural activity in rat somatosensory cortex. Neuron 39, 353-359.

Dickerson, B.C., Agosta, F., and Filippi, M. (2016). fMRI in Neurodegenerative Diseases: From Scientific Insights to Clinical Applications. Fmri Techniques and Protocols, 2nd Edition 119, 699-739.

Ding, S.L., Royall, J.J., Sunkin, S.M., Ng, L., Facer, B.A.C., Lesnar, P., Guillozet-Bongaarts, A., McMurray, B., Szafer, A., Dolbeare, T.A., *et al.* (2016). Comprehensive cellular-resolution atlas of the adult human brain. J Comp Neurol 524, 3127-3481.

Du, C., Volkow, N.D., Koretsky, A.P., and Pan, Y. (2014). Low-frequency calcium oscillations accompany deoxyhemoglobin oscillations in rat somatosensory cortex. Proc Natl Acad Sci USA 111, E4677-4686.

Du, Y.H., Pearlson, G.D., Liu, J.Y., Sui, J., Yu, Q.B., He, H., Castro, E., and Calhoun, V.D. (2015). A group ICA based framework for evaluating resting fMRI markers when disease categories are unclear: application to schizophrenia, bipolar, and schizoaffective disorders. NeuroImage 122, 272-280.

Fransson, P. (2005). Spontaneous low - frequency BOLD signal fluctuations: An fMRI investigation of the resting - state default mode of brain function hypothesis. Hum Brain Mapp 26, 15-29.

Glasser, M.F., Coalson, T.S., Robinson, E.C., Hacker, C.D., Harwell, J., Yacoub, E., Ugurbil, K., Andersson, J., Beckmann, C.F., Jenkinson, M.*, et al.* (2016a). A multi-modal parcellation of human cerebral cortex. Nature 536, 171-178.

Glasser, M.F., Smith, S.M., Marcus, D.S., Andersson, J.L.R., Auerbach, E.J., Behrens, T.E.J., Coalson, T.S., Harms, M.P., Jenkinson, M., Moeller, S.*, et al.* (2016b). The Human Connectome Project's neuroimaging approach. Nat Neurosci 19, 1175-1187.

Goense, J., Bohraus, Y., and Logothetis, N.K. (2016). fMRI at high spatial resolution: implications for BOLD-models. Frontiers in computational neuroscience 10.

Goense, J., Merkle, H., and Logothetis, N.K. (2012). High-Resolution fMRI Reveals Laminar Differences in Neurovascular Coupling between Positive and Negative BOLD Responses. Neuron 76, 629-639.

Greicius, M.D., Krasnow, B., Reiss, A.L., and Menon, V. (2003). Functional connectivity in the resting brain: A network analysis of the default mode hypothesis. Proceedings of the National Academy of Sciences of the United States of America 100, 253-258.

Guo, C.C., Sturm, V., and Zhou, J. (2016). Dominant hemisphere lateralization of cortical parasympathetic control as revealed by frontotemporal dementia. Proc Natl Acad Sci USA 113, E3985.

Haberg, A., Kvistad, K.A., Unsgard, G., and Haraldseth, O. (2004). Preoperative blood oxygen level-dependent functional magnetic resonance imaging in patients with primary brain tumors: Clinical application and outcome. Neurosurgery 54, 902-914.

Harel, N. (2012). Ultra high resolution fMRI at ultra-high field. NeuroImage 62, 1024-1028.

He, B.J., Snyder, A.Z., Zempel, J.M., Smyth, M.D., and Raichle, M.E. (2008). Electrophysiological correlates of the brain's intrinsic large-scale functional architecture. Proc Natl Acad Sci USA 105, 16039-16044.

Huber, L., Handwerker, D.A., Jangraw, D.C., Chen, G., Hall, A., Stüber, C., Gonzalez-Castillo, J., Ivanov, D., Marrett, S., and Guidi, M. (2017). High-Resolution CBV-fMRI Allows Mapping of Laminar Activity and Connectivity of Cortical Input and Output in Human M1. Neuron 96, 1-11.

Huber, L., Ivanov, D., Handwerker, D.A., Marrett, S., Guidi, M., Uludağ, K., Bandettini, P.A., and Poser, B.A. (2016). Techniques for blood volume fMRI with VASO: From low-resolution mapping towards sub-millimeter layer-dependent applications. NeuroImage.

Iadecola, C. (2004). Neurovascular regulation in the normal brain and in Alzheimer's disease. Nat Rev Neurosci 5, 347-360.

Jung, W.B., Im, G.H., Chung, J.J., Ahn, S.Y., Jeon, T.Y., Chang, Y.S., Park, W.S., Kim, J.H., Kim, K.S., and Lee, J.H. (2016). Neuroplasticity for spontaneous functional recovery after neonatal hypoxic ischemic brain injury in rats observed by functional MRI and diffusion tensor imaging. NeuroImage 126, 140-150.

Keilholz, S.D., Silva, A.C., Raman, M., Merkle, H., and Koretsky, A.P. (2006). BOLD and CBV-weighted functional magnetic resonance imaging of the rat somatosensory system. Magn Reson Med 55, 316-324.

Kim, S.G., Harel, N., Jin, T., Kim, T., Lee, P., and Zhao, F. (2013). Cerebral blood volume MRI with intravascular superparamagnetic iron oxide nanoparticles. NMR Biomed 26, 949-962.

Kim, S.G., Jin, T., and Fukuda, M. (2010). Spatial Resolution of fMRI Techniques. Fmri: Basics and Clinical Applications, 15-21.

Kim, S.G., and Ogawa, S. (2012). Biophysical and physiological origins of blood oxygenation level-dependent fMRI signals. J Cereb Blood Flow Metab 32, 1188-1206.

Kim, T., and Kim, S.G. (2011). Temporal dynamics and spatial specificity of arterial and venous blood volume changes during visual stimulation: implication for BOLD quantification. J Cereb Blood Flow Metab 31, 1211-1222.

Kokkonen, S.M., Nikkinen, J., Remes, J., Kantola, J., Starck, T., Haapea, M., Tuominen, J., Tervonen, O., and Kiviniemi, V. (2009). Preoperative localization of the sensorimotor area using independent component analysis of resting-state fMRI. Magn Reson Imaging 27, 733-740.

Kwong, K.K., Belliveau, J.W., Chesler, D.A., Goldberg, I.E., Weisskoff, R.M., Poncelet, B.P., Kennedy, D.N., Hoppel, B.E., Cohen, M.S., and Turner, R. (1992). Dynamic magnetic resonance imaging of human brain activity during primary sensory stimulation. Proceedings of the National Academy of Sciences 89, 5675-5679.

Lee, M.H., Smyser, C.D., and Shimony, J.S. (2013). Resting-State fMRI: A Review of Methods and Clinical Applications. Am J Neuroradiol 34, 1866-1872.

Li, W., Tutton, S., Vu, A.T., Pierchala, L., Li, B.S.Y., Lewis, J.M., Prasad, P.V., and Edelman, R.R. (2005). First-pass contrast-enhanced magnetic resonance angiography in humans using ferumoxytol, a novel ultrasmall superparamagnetic iron oxide (USPIO)-based blood pool agent. J Magn Reson Imaging 21, 46-52.

Logothetis, N.K. (2008). What we can do and what we cannot do with fMRI. Nature 453, 869-878.

Lu, H., Golay, X., Pekar, J.J., and van Zijl, P.C.M. (2003). Functional magnetic resonance Imaging based on changes in vascular space occupancy. Magn Reson Med 50, 263-274.

Maass, A., Berron, D., Libby, L.A., Ranganath, C., and Duzel, E. (2015). Functional subregions of the human entorhinal cortex. Elife 4.

Mandeville, J.B. (2012). IRON fMRI measurements of CBV and implications for BOLD signal. NeuroImage 62, 1000-1008.

Masch, W.R., Wang, P.I., Chenevert, T.L., Junck, L., Tsien, C., Heth, J.A., and Sundgren, P.C. (2016). Comparison of Diffusion Tensor Imaging and Magnetic Resonance Perfusion Imaging in Differentiating Recurrent Brain Neoplasm From Radiation Necrosis. Acad Radiol 23, 569-576.

Matthews, P.M., and Hampshire, A. (2016). Clinical Concepts Emerging from fMRI Functional Connectomics. Neuron 91, 511-528.

Matthews, P.M., Honey, G.D., and Bullmore, E.T. (2006). Applications of fMRI in translational medicine and clinical practice. Nature Reviews Neuroscience 7, 732-744.

Murphy, K., Birn, R.M., and Bandettini, P.A. (2013). Resting-state fMRI confounds and cleanup. NeuroImage 80, 349-359.

Ogawa, S., Menon, R.S., Tank, D.W., Kim, S.G., Merkle, H., Ellermann, J.M., and Ugurbil, K. (1993). Functional Brain Mapping by Blood Oxygenation Level-Dependent Contrast Magnetic-Resonance-Imaging - a Comparison of Signal Characteristics with a Biophysical Model. Biophys J 64, 803-812.

Ogawa, S., Tank, D.W., Menon, R., Ellermann, J.M., Kim, S.G., Merkle, H., and Ugurbil, K. (1992). Intrinsic signal changes accompanying sensory stimulation: functional brain mapping with magnetic resonance imaging. Proceedings of the National Academy of Sciences 89, 5951-5955.

Pan, W.J., Thompson, G.J., Magnuson, M.E., Jaeger, D., and Keilholz, S. (2013). Infraslow LFP correlates to resting-state fMRI BOLD signals. NeuroImage 74, 288-297.

Park, C.H., Chang, W.H., Ohn, S.H., Kim, S.T., Bang, O.Y., Pascual-Leone, A., and Kim, Y.H. (2011). Longitudinal Changes of Resting-State Functional Connectivity During Motor Recovery After Stroke. Stroke 42, 1357-1362.

Pievani, M., Filippini, N., van den Heuvel, M.P., Cappa, S.F., and Frisoni, G.B. (2014). Brain connectivity in neurodegenerative diseases-from phenotype to proteinopathy. Nat Rev Neurol 10, 620-633.

Pittau, F., Grouiller, F., Spinelli, L., Seeck, M., Michel, C.M., and Vulliemoz, S. (2014). The role of functional neuroimaging in pre-surgical epilepsy evaluation. Front Neurol 5.

Polimeni, J.R., Fischl, B., Greve, D.N., and Wald, L.L. (2010). Laminar analysis of 7 T BOLD using an imposed spatial activation pattern in human V1. NeuroImage 52, 1334-1346.

Reid, L.B., Sale, M.V., Cunnington, R., Mattingley, J.B., and Rose, S.E. (2017). Brain Changes Following Four Weeks of Unimanual Motor Training: Evidence From fMRI-Guided Diffusion MRI Tractography. Hum Brain Mapp 38, 4302-4312.

Sair, H.I., Yahyavi-Firouz-Abadi, N., Calhoun, V.D., Airan, R.D., Agarwal, S., Intrapiromkul, J., Choe, A.S., Gujar, S.K., Caffo, B., Lindquist, M.A., and Pillai, J.J. (2016). Presurgical brain mapping of the language network in patients with brain tumors using resting-state fMRI: Comparison with task fMRI. Hum Brain Mapp 37, 913-923.

Scholvinck, M.L., Maier, A., Ye, F.Q., Duyn, J.H., and Leopold, D.A. (2010). Neural basis of global resting-state fMRI activity. Proc Natl Acad Sci USA 107, 10238-10243.

Shmuel, A., and Leopold, D.A. (2008). Neuronal correlates of spontaneous fluctuations in fMRI signals in monkey visual cortex: Implications for functional connectivity at rest. Hum Brain Mapp 29, 751-761.

Silva, A.C., and Koretsky, A.P. (2002). Laminar specificity of functional MRI onset times during somatosensory stimulation in rat. Proc Natl Acad Sci USA 99, 15182-15187.

Smith, S.M., Fox, P.T., Miller, K.L., Glahn, D.C., Fox, P.M., Mackay, C.E., Filippini, N., Watkins, K.E., Toro, R., Laird, A.R., and Beckmann, C.F. (2009). Correspondence of the brain's functional architecture during activation and rest. Proc Natl Acad Sci USA 106, 13040-13045.

Smitha, K.A., Arun, K.M., Rajesh, P.G., Thomas, B., and Kesavadas, C. (2017). Resting-State Seed-Based Analysis: An Alternative to Task-Based Language fMRI and Its Laterality Index. Am J Neuroradiol 38, 1187-1192.

Torrisi, S., O'Connell, K., Davis, A., Reynolds, R., Balderston, N., Fudge, J.L., Grillon, C., and Ernst, M. (2015). Resting State Connectivity of the Bed Nucleus of the Stria Terminalis at Ultra-High Field. Hum Brain Mapp 36, 4076-4088.

Ugurbil, K. (2014). Magnetic resonance imaging at ultrahigh fields. IEEE Trans Biomed Eng 61, 1364-1379.

Ugurbil, K., Xu, J.Q., Auerbach, E.J., Moeller, S., Vu, A.T., Duarte-Carvajalino, J.M., Lenglet, C., Wu, X.P., Schmitter, S., Van de Moortele, P.F.*, et al.* (2013). Pushing spatial and temporal resolution for functional and diffusion MRI in the Human Connectome Project. NeuroImage 80, 80-104.

Van den Heuvel, M.P., and Yeo, B.T.T. (2017). A Spotlight on Bridging Microscale and Macroscale Human Brain Architecture. Neuron 93, 1248-1251.

Yacoub, E., Harel, N., and Ugurbil, K. (2008). High-field fMRI unveils orientation columns in humans. Proceedings of the National Academy of Sciences of the United States of America 105, 10607-10612.

Yacoub, E., Shmuel, A., Logothetis, N., and Ugurbil, K. (2007). Robust detection of ocular dominance columns in humans using Hahn Spin Echo BOLD functional MRI at 7 Tesla. NeuroImage 37, 1161-1177.

Young, K.D., Zotev, V., Phillips, R., Misaki, M., Yuan, H., Drevets, W.C., and Bodurka, J. (2014). Real-Time fMRI Neurofeedback Training of Amygdala Activity in Patients with Major Depressive Disorder. Plos One 9.

Yu, X. (2017). When Photons Meet Protons: Optogenetics, Calcium Signal Detection, and fMRI in Small Animals. In Small Animal Imaging: Basics and Practical Guide, F. Kiessling, B.J. Pichler, and P. Hauff, eds. (Cham: Springer International Publishing), pp. 773-791.

Yu, X., Glen, D., Wang, S., Dodd, S., Hirano, Y., Saad, Z., Reynolds, R., Silva, A.C., and Koretsky, A.P. (2012). Direct imaging of macrovascular and microvascular contributions to BOLD fMRI in layers IV-V of the rat whisker-barrel cortex. NeuroImage 59, 1451-1460.

Yu, X., Qian, C., Chen, D.Y., Dodd, S.J., and Koretsky, A.P. (2014). Deciphering laminar-specific neural inputs with line-scanning fMRI. Nat Methods 11, 55-58.

Zalesky, A., Fornito, A., Cocchi, L., Gollo, L.L., and Breakspear, M. (2014). Time-resolved resting-state brain networks. Proceedings of the National Academy of Sciences of the United States of America 111, 10341-10346.

Zhao, F., Holahan, M.A., Houghton, A.K., Hargreaves, R., Evelhoch, J.L., Winkelmann, C.T., and Williams, D.S. (2015). Functional imaging of olfaction by CBV fMRI in monkeys: insight into the role of olfactory bulb in habituation. NeuroImage 106, 364-372.

Zhao, F.Q., Wang, P., Hendrich, K., and Kim, S.G. (2005). Spatial speciricity of cerebral blood volume-weighted fMRI responses at columnar resolution. NeuroImage 27, 416-424.

Zhou, I.Y., Cheung, M.M., Lau, C., Chan, K.C., and Wu, E.X. (2012). Balanced steady-state free precession fMRI with intravascular susceptibility contrast agent. Magn Reson Med 68, 65-73.

Zhou, J., Greicius, M.D., Gennatas, E.D., Growdon, M.E., Jang, J.Y., Rabinovici, G.D., Kramer, J.H., Weiner, M., Miller, B.L., and Seeley, W.W. (2010). Divergent network connectivity changes in behavioural variant frontotemporal dementia and Alzheimer's disease. Brain 133, 1352-1367.

Zhu, D.C., and Majumdar, S. (2014). Integration of Resting- State FMRI and Diffusion- Weighted MRI Connectivity Analyses of the Human Brain: Limitations and Improvement. J Neuroimaging 24, 176-186.

2.7 Author Contribution

A.1

Yu, X., ***He, Y.***, Wang, M., Merkle, H., Dodd, S.J., Silva, A.C., and Koretsky, A.P.
Sensory and optogenetically driven single-vessel fMRI.
Nat Methods, 2016, 13, 337-340, doi: 10.1038/nmeth.3765.

X.Y. and A.P.K. initiated the work, developed the method and wrote the paper. ***Y.H.*** and M.W. helped with 14-T MRI data acquisition and analysis. X.Y. performed MRI experiments at 11.7 T and 14 T. A.C.S. and S.J.D. helped set up the k-space reconstruction. H.M. and S.J.D. designed the radiofrequency coil.

A.2

He, Y., Wang, M., Yu, X.
Directly mapping the single-vessel hemodynamic signal with Multi-echo Line-scanning fMRI (MELS-fMRI).
Journal of Cerebral Blood Flow and Metabolism, 2017, under revision.

X.Y. designed the research. ***Y.H.***, M.W. performed animal experiments; ***Y.H.***, X.Y. acquired and analyzed data; X.Y., ***Y.H.*** wrote the paper.

A.3

He, Y., Wang, M., Chen, X., Pohmann, R., Polimeni, J., Scheffler, K., Rosen, B., Kleinfeld, D. and Yu, X.
Ultra-slow single vessel BOLD and CBV-based fMRI spatiotemporal dynamics and their correlation with neuronal intracellular calcium signals.
Neuron, 2018, 97 (4), 925-939. e5

X.Y., D.K. and B.R. designed the research, ***Y.H.***, X.Y., M.W. and X.C. performed animal experiments, ***Y.H.***, X.Y. and R.P. acquired data, ***Y.H.*** analyzed data, K.S., R.P., J.R. and M.W. provided key technical support, and X.Y., D.K. and ***Y.H.*** wrote the manuscript.

3. ACKNOWLEDGEMENTS

First of all, I especially appreciate my supervisor Dr. Xin Yu for his thoughtful guidance throughout my Ph.D. research studies and giving me the opportunity to work in the leading research organization: Max Planck Society. I particularly thank Dr. Rolf Pohmann and Prof. Dr. Klaus Scheffler for their excellent technical guidance and constructive comments. Besides, I would also like to sincerely thank my committee members Prof. Dr. Andreas Bartels and Prof. Dr. Bernd Nürnberg for their encouragement, valuable guidance and reviewing this thesis.

Furthermore, I would also like to thank all colleagues who provide us for technical support and animal maintenance support. I am very thankful for all the patience and professional assistance.

Last but not least, I am grateful to my family and friends for their love and continuous support when I am on the way to pursue my dreams.

4. APPENDIX

4.1 A.1: Sensory and optogenetically driven single-vessel fMRI

Sensory and optogenetically driven single-vessel fMRI

Yu, X., **He, Y.**, Wang, M., Merkle, H., Dodd, S.J., Silva, A.C., and Koretsky, A.P.

Nat Methods, 2016, 13, 337-340.

doi: 10.1038/nmeth.3765.

© 2016 Nature America, Inc. All rights reserved.

Sensory and optogenetically driven single-vessel fMRI

Xin Yu[1], Yi He[1], Maosen Wang[1], Hellmut Merkle[2], Stephen J Dodd[2], Afonso C Silva[2] & Alan P Koretsky[2]

Magnetic resonance imaging (MRI) sensitivity approaches vessel specificity. We developed a single-vessel functional MRI (fMRI) method to image the contribution of vascular components to blood oxygenation level–dependent (BOLD) and cerebral blood volume (CBV) fMRI signal. We mapped individual vessels penetrating the rat somatosensory cortex with 100-ms temporal resolution by MRI with sensory or optogenetic stimulation. The BOLD signal originated primarily from venules, and the CBV signal from arterioles. The single-vessel fMRI method and its combination with optogenetics provide a platform for mapping the hemodynamic signal through the neurovascular network with specificity at the level of individual arterioles and venules.

MAIN TEXT

fMRI maps brain activity by means of tight coupling of hemodynamic responses in the local vasculature to neural activity[1–4]. However, this neurovascular coupling limits fMRI specificity, because of the complexity of the hemodynamic response[3,5–7]. Given the large voxel size (on the order of millimeters) and slow acquisition time (on the order of seconds) of conventional fMRI, detailed high-resolution hemodynamic responses are usually not sampled[2–4]. The spatial discrepancy between the vascular origin of the fMRI signal and the neural source that produces the vascular response remains a concern for fMRI brain mapping.

Recently, high magnetic field strengths have made it possible to acquire high-spatiotemporal-resolution fMRI images with increased signal-to-noise ratios[8,9]. These increased signal-to-noise ratios have been used to improve spatial and/or temporal resolution in order to localize BOLD signal to venules in the rat somatosensory cortex[10] and correlate a punctate pattern of CBV signal to arterioles in the cat visual cortex[11]. Furthermore, very high-temporal-resolution fMRI has detected fMRI onset at specific cortical layers coinciding with neural projection inputs[5]. In human brains, layer-dependent fMRI signal was mapped by gradient-echo BOLD and vascular space occupancy–based CBV methodologies at submillimeter resolution[12]. However, no study has mapped the fMRI signal from individual vessels in deep cortical layers with sampling rates sufficient to define the response. Here we developed a strategy to enable direct imaging of both arteriole and venule responses to neural activity at 100-ms resolution.

Previously, a conventional fMRI–echo-planar imaging (EPI) method[13] was used to characterize BOLD signal from distinct vascular components in midcortical layers of the rat somatosensory cortex[10]. One can map different vascular responses by CBV fMRI with iron oxide–particle injection using the EPI method (**Supplementary Fig. 1** and **Supplementary Note 1**). Recently we adapted a line-scanning scheme to the fast low-angle shot (FLASH) fMRI method and achieved very high temporal resolution[5,9] (**Supplementary Fig. 2**). We used the FLASH fMRI method to map BOLD and CBV fMRI signal from 2D slices acquired perpendicular to the vessels penetrating the midcortical layers of somatosensory cortex of anesthetized rats (**Supplementary Figs. 3–5**, **Supplementary Video 1** and **Supplementary Note 1**). In contrast to the positive BOLD signal, which was mainly due to the increased ratio of oxygenated to deoxygenated blood in venules, the negative CBV signal was caused by activity-evoked vasodilation leading to increased blood volume, more iron oxide particles, a shorter T2* relaxation time and, therefore, less signal in the imaged vessels. Vasodilation has been attributed to arterioles, and there are reports of vein and venule dilation as well[14]. In addition, changes in capillary diameter could be a major contributor to or initiator of changes in cerebral blood volume[15]. To detect single-vessel responses driven by sensory (i.e., electrical stimulation of the forepaw or whisker pad) or optogenetic stimulation through a fiber optic directly targeting the cortex, we used a multigradient-echo (MGE) sequence to anatomically map individual arterioles and venules penetrating the midcortical layers of somatosensory cortex. The blood flow delineates vessels: unsaturated MRI signal from blood flowing into a slice can be detected as brighter signal in vessels[16]. In this study, the specific in-flow effect resulted in brighter signal in both arterioles and venules compared with surrounding voxels (**Fig. 1a**). The deoxygenated blood in venules has a shorter T2* than surrounding tissues and arterioles, which leads to less signal only in venules at longer TE (time to echo). Here arterioles and surrounding tissues had a similar but longer T2*, and thus brighter signal, compared with venules (**Fig. 1a** and **Supplementary Fig. 6**), consistent with previous results[17]. MGE images acquired at different TEs enabled us to create an anatomical map of penetrating arterioles and venules (A-V map) (**Fig. 1b**). Using the FLASH fMRI method, we were able to detect both BOLD and CBV fMRI signal from the same 2D slice for the A-V map. The peak BOLD signal overlapped primarily with penetrating venule regions of interest (ROIs), and the peak CBV signal overlapped primarily with penetrating arteriole ROIs (**Fig. 1c** and **Supplementary Videos 2–9**). 3D and 2D plots of the vessel-specific spatial distribution of BOLD and CBV fMRI signal as a function of the normalized signal intensity of individual voxels from the A-V map showed peak CBV signal on arteriole voxels, whereas the peak BOLD signal was on venule voxels (**Fig. 1d**,**e**

---

[1]High Field Magnetic Resonance Department, Max Planck Institute for Biological Cybernetics, Tuebingen, Germany. [2]Laboratory of Functional and Molecular Imaging, National Institute of Neurological Disorders and Stroke, US National Institutes of Health, Bethesda, Maryland, USA. Correspondence should be addressed to X.Y. (xin.yu@tuebingen.mpg.de) or A.P.K. (korestkya@mail.nih.gov).

RECEIVED 29 MAY 2015; ACCEPTED 7 JANUARY 2016; PUBLISHED ONLINE 8 FEBRUARY 2016; CORRECTED ONLINE 29 FEBRUARY 2016 (DETAILS ONLINE); DOI:10.1038/NMETH.3765

© 2016 Nature America, Inc. All rights reserved.

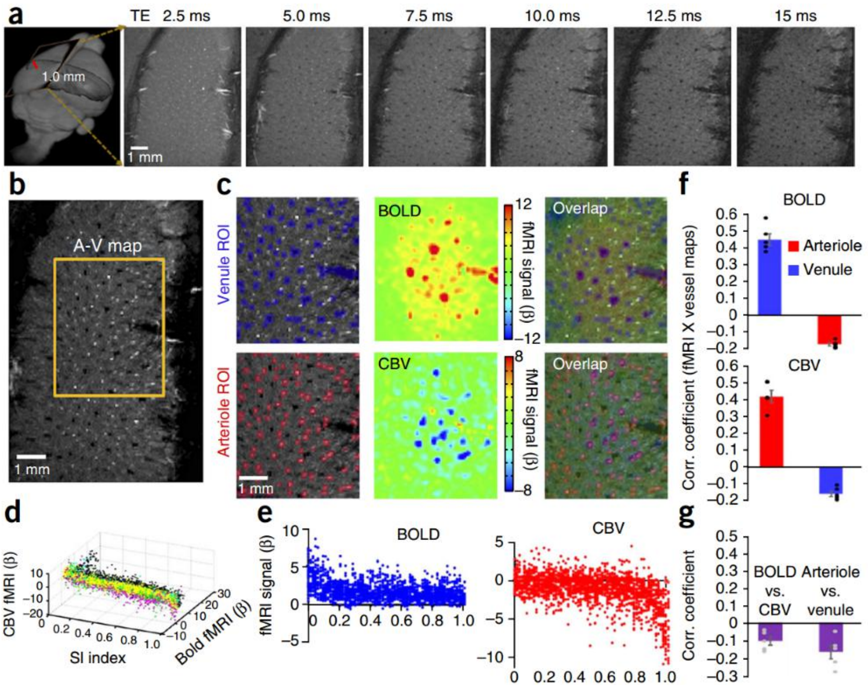

Figure 1 | Single-vessel fMRI overlaps with the A-V map. (**a**) 2D MGE slices from a deep layer of the forepaw S1 cortex (1.0–1.5 mm, left) at different TEs (representative images from experiments with seven rats). (**b**) The A-V map derived from the images in **a**. Arterioles and venules appear as bright and dark voxels, respectively. (**c**) Zoomed views of the area outlined in **b** with venule and arteriole ROIs highlighted, BOLD and CBV fMRI maps of the same 2D slice, and overlap (active voxels are in purple in overlap images). (**d**) Distribution of BOLD and CBV signals as a function of voxel normalized signal intensity (SI) in A-V maps ($n = 5$, denoted by different colors of plotted points). (**e**) A 2D plot of BOLD and CBV fMRI signals from individual voxels as a function of voxel signal intensity in A-V maps (representative of one data set from **d**). (**f**) The spatial correlation (Corr.) coefficients of BOLD and CBV functional maps with represent the coefficients of individual rats ($n = 5$); mean ± s.e.m.). Significant differences were noted between arterioles and venules for both signals (BOLD, $P = 0.00002$; CBV, $P = 0.0003$; Student's *t*-test). (**g**) The spatial correlation coefficients of the functional maps (BOLD versus CBV) and the single-vessel ROI maps (arteriole versus venule) (mean ± s.e.m.). Gray dots represent the coefficients of individual rats ($n = 5$). In **a** and **c**, scale bar applies to all images in the panel.

and **Supplementary Video 10**). The spatial correlation coefficient of BOLD functional maps with venule ROI maps was significantly higher than that with arteriole ROI maps, whereas the opposite was true for CBV functional maps (**Fig. 1f**). Spatial correlation was negative for BOLD with arterioles and for CBV with venules. Negative spatial correlation coefficients were also detected for BOLD versus CBV functional maps and for arteriole versus venule ROI maps (**Fig. 1g**), indicating that most of the BOLD responses came from venules (in agreement with recent work[10]) and that most of the CBV responses came from arterioles[11,12]. Thus the single-vessel method made it possible to identify the hemodynamic signal from individual arterioles and venules.

The discovery of channelrhodopsin 2 (ChR2) as a light-sensitive cation membrane channel has made it possible to control neural activity optogenetically by targeting specific cell types in neural circuits[18,19]. Optogenetics has been used to initiate fMRI signals[20]. The temporal and spatial features of the hemodynamic signal evoked by optogenetic stimulation were assessed by optical measurement of oxygenated versus deoxygenated hemoglobin in the somatosensory cortex[21], as well as with BOLD fMRI[22,23], although not at the single-vessel level. To determine whether the hemodynamic features of such fMRI signals are similar to those of signals evoked with more physiological stimulation, we optogenetically evoked neural activity with a fiber optic inserted into rat whisker barrel cortex expressing ChR2 (**Fig. 2a**). Recordings of the local field potential indicated robust responses upon optical stimulation (**Supplementary Fig. 7**). We mapped BOLD and CBV signal with EPI-fMRI in the region close to the tip of the fiber optic (**Fig. 2b** and **Supplementary Fig. 8**) and aligned the A-V map to specify individual arterioles and venules near the tip (**Fig. 2c**). The light-driven BOLD signal was located primarily at venule voxels, whereas the CBV signal was located primarily at arteriole voxels (**Fig. 2d** and **Supplementary Videos 11** and **12**). The average time courses of BOLD and CBV signal from venule and arteriole ROIs showed similar temporal patterns with both sensory and optogenetic stimuli (**Fig. 2e**,**f**).

To quantitatively compare optogenetically activated and sensory-evoked hemodynamic signals, we fit BOLD and CBV signals from individual arterioles and venules to estimate the onset time (t_0), the time to peak (ttp) and the full-width at half-maximum (FWHM) (**Supplementary Figs. 9–11**). The CBV signals of individual arterioles showed earlier onset (t_0) and ttp than did the BOLD signals of individual venules for both sensory stimulation and optogenetics (**Fig. 3a** and **Supplementary Fig. 9**). However, there were a few very early BOLD responding venules and a few arterioles with late onset of CBV signal (**Supplementary Fig. 12** and **Supplementary Note 1**). We analyzed the BOLD signals from individual arterioles (**Supplementary Fig. 10**) and the CBV signals from individual venules (**Supplementary Fig. 11**) to characterize specific vascular contributions to BOLD and CBV fMRI signal, respectively (discussed in **Supplementary Note 1**). The t_0, ttp and FWHM plots of the single-vessel BOLD and CBV signals readily separated into distinct clusters of arterioles and venules (**Fig. 3b**,**c** and **Supplementary Videos 13** and **14**). The temporal parameters of the optogenetically activated fMRI signal showed little difference in comparison to the sensory stimulation–evoked fMRI signal acquired via either 11.7-T or 14-T MRI (**Supplementary Fig. 13** and **Supplementary Table 1**; Student's *t*-test). Thus, the temporal features of hemodynamic signal propagating through the cerebrovascular network were similar for optogenetic and sensory stimulation–evoked neural activity.

Two-photon microscopy is increasingly used to image vessels in the cortex[24–26]. The single-vessel fMRI method has three potential benefits as compared to optical imaging. First, we were able to detect fMRI signal from individual penetrating vessels in midcortical layers. Using this strategy, it should be possible to map single vessels located in subcortical brain regions such as the hippocampus. Second, it is possible to use the full range of MRI techniques to enable

© 2016 Nature America, Inc. All rights reserved.

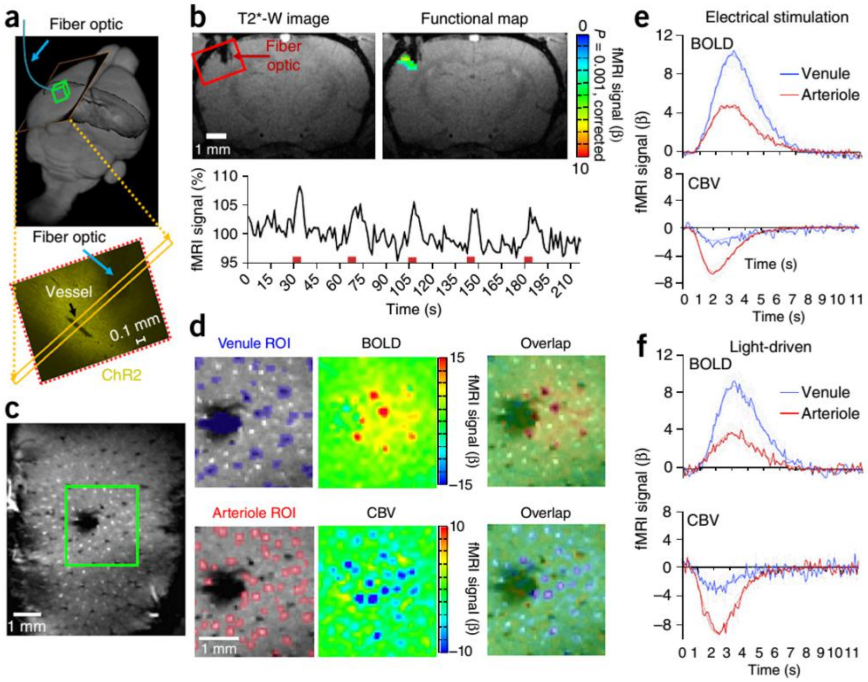

Figure 2 | Optogenetically induced fMRI signal from single vessels penetrating the barrel cortex. (**a**) Overview of optogenetically driven single-vessel fMRI and a histological section (from the boxed area in **b**) showing ChR2 expression. The blue arrows show the ic entry point; the black arrow points out a penetrating vessel. The yellow rectangle encloses the area imaged by single-vessel fMRI. Images are representative of experiments with nine rats. (**b**) Top left, T2*-weighted (T2*-W) image with the fiber optic inserted into the barrel cortex. Top right, overlay of the optogenetically induced fMRI signal on the T2*-weighted image. The average time course from the indicated cortical area (bottom) shows corresponding fMRI signal changes with the block-design paradigm (illumination: 5 s on/30 s off, 5 epoch, 20-ms light pulse, 10 Hz, 3.2 mw). (**c**) A-V map with venule (bright) and arteriole (dark) voxels. The dark area in the center indicates the position of the fiber optic. The green box outlines the area shown in **d**. (**d**) Venule and arteriole ROIs on the A-V maps (left) , BOLD and CBV fMRI maps (center) and overlap (BOLD, top; CBV, bottom). (e) The average BOLD and CBV fMRI time courses from individual arterioles and venules after sensory stimulation of the forepaw. (BOLD, *n* = 7 rats; CBV, *n* = 5 rats; all ROIs were averaged for each rat. The mean values shown are of the averages for all rats in each group; gray region denotes error (±s.e.m.).) (f) The average BOLD and CBV fMRI time courses from individual arterioles and venules driven by optogenetic stimulation of the barrel cortex (*n* = 4 rats; gray region denotes error (±s.e.m.); illumination: 20 ms, 10 Hz, 3.2 mw (light pulse on for 2 s)). In **b** and **d**, scale bar applies to all images in the panel.

coregistration of anatomy, connectivity and fMRI in order to obtain complementary information. It might even become possible to extend the single-vessel mappings to the human brain as sensitivity increases with the emerging high-field MRI. Third, fMRI can be performed without any invasive procedures on animal subjects, as opposed to optical imaging, which requires window or thin skull preparations and possibly the insertion of optical equipment into the brain. Moreover, the fMRI signal could be acquired with temporal resolution similar to that of optical microscopy. In the current study we acquired data at a 100-ms temporal interval, which represents a sampling rate similar to that of optical brain imaging methods, in which the temporal resolution ranges from 9–18 Hz for fields of view on the submillimeter scale.

A question that arose during this work was how well individual penetrating arterioles and venules were characterized in the cortex. The average distance between venule voxels measured in the present work was 372 ± 33 μm, and that between arterioles was 286 ± 15 μm (mean ± s.e.m.). These values are in agreement with the known spacing of these vessels, indicating that the majority of penetrating vessels were detected[26]. The established size of penetrating vessels separated by a few hundred micrometers ranges from 30 to 70 μm (ref. 26). We acquired the A-V map with an in-plane resolution of 75 × 75 μm or 50 × 50 μm, which is close to the mean size of the main penetrating vessels (**Fig. 2** and **Supplementary Fig. 8**). The brightest voxels of A-V maps were usually detected within a 2 × 2 voxel matrix, implying that the in-flow effect was sufficient to highlight individual arterioles smaller than the voxels. Darker voxels representing penetrating venules were larger than the actual venules because of the extravascular dephasing effect of deoxygenated hemoglobin in venule blood[27]. Different vessel sizes with potentially different orientation angles probably led to variation in the signal intensity of vessel voxels. The arterioles and venules were identified on the basis of a nearest-neighbor variation analysis; however, it is likely that some smaller penetrating vessels were not identified. It is important to note that in this study, “single vessel” refers to the arteriole or venule voxels in the A-V map that could be detected under the imaging condition used.

This work shows that the peak BOLD signal aligned with venule voxels and the peak CBV signal aligned with arteriole voxels. The t_0 and ttp of the CBV signal from arterioles was comparable to the temporal-onset estimates of arteriole dilation detected with two-photon microscopy at a 0.5-mm cortical depth[25]. This observation was also consistent with BOLD and CBV studies performed in cats[11] and humans[12] to show the early onset of CBV signals. The mean t_0 of BOLD signal in venules (0.96 ± 0.04 s, mean ± s.e.m.) was slightly faster than what was previously reported for macrovenules detected by EPI-fMRI methods[10]. In a previous study, Hutchinson *et al.* measured[24] the transit time (calculated using the time to half-maximum ($t_{1/2}$)) from surface arterioles to venules as 0.8–1.2 s with two-photon microscopy. The average transit time estimated in the present study was ~0.8 s on the basis of the mean time-to-peak difference from arteriole CBV to venule BOLD signal in the mid-cortical layers (**Supplementary Note 1**). The MRI-defined transit time was on the lower end of the range of transit times measured by optical microscopy[24], which may be explained by differences in the induction of vessel dilation, in the imaged capillary network and in the definition of transit time. The estimated transit time based on comparison of arteriole and venule fMRI signals illustrates that vessel-specific hemodynamic signal propagation can be measured with the single-vessel fMRI method.

In conclusion, we were able to characterize distinct arteriole CBV and venule BOLD signals with 100-ms temporal resolution. The vascular kinetics of light-driven and sensory-evoked fMRI

© 2016 Nature America, Inc. All rights reserved.

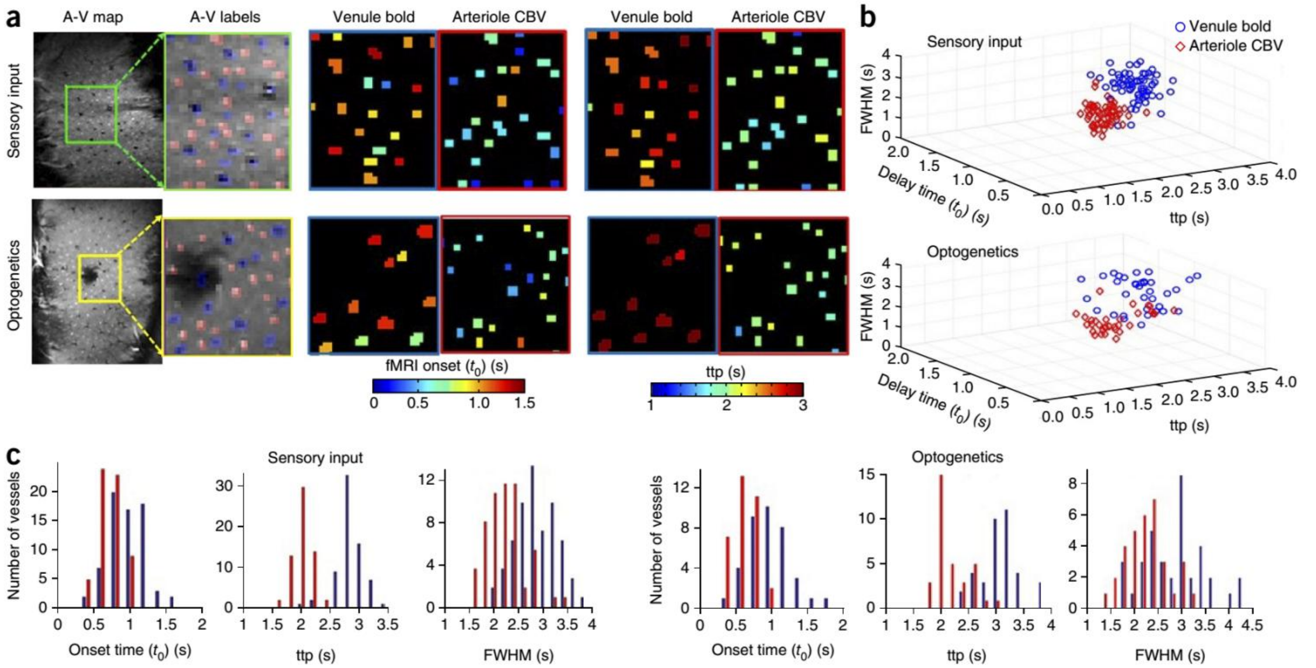

Figure 3 | Temporal features of sensory and optogenetically driven BOLD and CBV fMRI signals from individual arterioles and venules. (**a**) A-V maps of individual arteriole (red) and venule (blue) voxels, t_0 maps and ttp maps of a representative rat, each for either sensory stimulation ($n = 5$ rats) or fiber optic–mediated optical stimulation ($n = 4$ rats). (**b**) 3D plots of t_0, ttp and FWHM of sensory-evoked fMRI signal from individual arteriole ($n = 61$, $r^2 > 0.4$) and venule ($n = 69$, $r^2 > 0.5$) voxels ($n = 5$ rats) and of light-driven fMRI signal from individual arteriole ($n = 33$, $r^2 > 0.3$) and venule ($n = 37$, $r^2 > 0.35$) voxels ($n = 4$ rats). (**c**) Distribution of the number of venule (blue) and arteriole (red) voxels with different t_0, ttp and FWHM in rats with sensory stimulation ($n = 5$) or fiber optic–mediated optical stimulation by optogenetics ($n = 4$ rats).

signals in the deep cortical layers were similar, consistent with previous optogenetic fMRI studies[22,23], which we extended to the single-vessel level in the present study. The single-vessel fMRI method and its combination with optogenetics should enable researchers to decipher individual vascular coupling events in the neuron-glia-vessel network in both normal and diseased brain states.

METHODS

Methods and any associated references are available in the online version of the paper.

Note: Any Supplementary Information and Source Data files are available in the online version of the paper.

ACKNOWLEDGMENTS

This research was supported by the Intramural Research Program of the US National Institutes of Health, the US National Institute of Neurological Disorders and Stroke and internal funding from the Max Planck Society. We thank H. Schulz, S. Fischer, K. Sharer and N. Bouraoud for technical support and A. Bonci for help with the optogenetic setup.

AUTHOR CONTRIBUTIONS

X.Y. and A.P.K. initiated the work, developed the method and wrote the paper. A.C.S. and S.J.D. helped setup the *k*-space reconstruction. H.M. and S.J.D. designed the radiofrequency coil. X.Y. performed MRI experiments at 11.7 T and 14 T. Y.H. and M.W. helped with 14-T MRI data acquisition and analysis.

COMPETING FINANCIAL INTERESTS

The authors declare no competing financial interests.

Reprints and permissions information is available online at http://www.nature.com/reprints/index.html.

1. Belliveau, J.W. *et al. Science* **254**, 716–719 (1991).
2. Ogawa, S. *et al. Proc. Natl. Acad. Sci. USA* **89**, 5951–5955 (1992).
3. Kwong, K.K. *et al. Proc. Natl. Acad. Sci. USA* **89**, 5675–5679 (1992).
4. Bandettini, P.A., Wong, E.C., Hinks, R.S., Tikofsky, R.S. & Hyde, J.S. *Magn. Reson. Med.* **25**, 390–397 (1992).
5. Yu, X., Qian, C., Chen, D.Y., Dodd, S.J. & Koretsky, A.P. *Nat. Methods* **11**, 55–58 (2014).
6. Logothetis, N.K., Pauls, J., Augath, M., Trinath, T. & Oeltermann, A. *Nature* **412**, 150–157 (2001).
7. Uğurbil, K., Toth, L. & Kim, D.S. *Trends Neurosci.* **26**, 108–114 (2003).
8. Duyn, J.H. *Neuroimage* **62**, 1241–1248 (2012).
9. Silva, A.C. & Koretsky, A.P. *Proc. Natl. Acad. Sci. USA* **99**, 15182–15187 (2002).
10. Yu, X. *et al. Neuroimage* **59**, 1451–1460 (2012).
11. Moon, C.H., Fukuda, M. & Kim, S.G. *Neuroimage* **64**, 91–103 (2013).
12. Huber, L. *et al. Neuroimage* **107**, 23–33 (2015).
13. Jezzard, P. *et al. NMR Biomed.* **7**, 35–44 (1994).
14. Lee, S.P., Duong, T.Q., Yang, G., Iadecola, C. & Kim, S.G. *Magn. Reson. Med.* **45**, 791–800 (2001).
15. Hall, C.N. *et al. Nature* **508**, 55–60 (2014).
16. Wedeen, V.J. *et al. Science* **230**, 946–948 (1985).
17. Bolan, P.J., Yacoub, E., Garwood, M., Ugurbil, K. & Harel, N. *Neuroimage* **32**, 62–69 (2006).
18. Boyden, E.S., Zhang, F., Bamberg, E., Nagel, G. & Deisseroth, K. *Nat. Neurosci.* **8**, 1263–1268 (2005).
19. Zhao, S. *et al. Nat. Methods* **8**, 745–752 (2011).
20. Lee, J.H. *et al. Nature* **465**, 788–792 (2010).
21. Vazquez, A.L., Fukuda, M., Crowley, J.C. & Kim, S.G. *Cereb. Cortex* **24**, 2908–2919 (2014).
22. Iordanova, B., Vazquez, A.L., Poplawsky, A.J., Fukuda, M. & Kim, S.G. *J. Cereb. Blood Flow Metab.* **35**, 922–932 (2015).
23. Kahn, I. *et al. J. Neurosci.* **31**, 15086–15091 (2011).
24. Hutchinson, E.B., Stefanovic, B., Koretsky, A.P. & Silva, A.C. *Neuroimage* **32**, 520–530 (2006).
25. Tian, P. *et al. Proc. Natl. Acad. Sci. USA* **107**, 15246–15251 (2010).
26. Blinder, P., Shih, A.Y., Rafie, C. & Kleinfeld, D. *Proc. Natl. Acad. Sci. USA* **107**, 12670–12675 (2010).
27. Boxerman, J.L., Hamberg, L.M., Rosen, B.R. & Weisskoff, R.M. Magn. Reson. Med. 34, 555–566 (1995).

npg © 2016 Nature America, Inc. All rights reserved.

ONLINE METHODS

MRI image acquisition. All images were acquired with an 11.7 T/31 cm and 14.1 T/26 cm horizontal bore magnet (Magnex) interfaced to an Avance III console (Bruker) and equipped with a 12-cm gradient set capable of providing 100 G/cm with a rise time of 150 µs (Resonance Research). For the 11.7-T scanner, a custom-built 9-cm-diameter quadrature transmitter coil was placed in the gradient. Surface receive-only coils were used during image acquisition. For the 14-T scanner, a transceiver surface coil with a 6-mm diameter was used to acquire fMRI images.

Line-scanning fMRI. A 2D FLASH sequence was used to map the fMRI signal with the following parameters: TE, 4 ms (CBV) or 16 ms (BOLD); repetition time (TR), 100 ms; matrix, 80 × 32 (11.7 T) or 96 × 64 (14 T); in-plane resolution, 150 × 150 µm (11.7 T) or 100 × 100 µm (14 T); slice thickness, 500 µm; flip angle, 20°. As previously described[5,9], the single *k*-space line was acquired for each image of the block-design stimulation pattern. The on/off stimulation trials were repeated for the number of phase-encoding steps (**Supplementary Fig. 2**). The field of view (FOV) along the phase-encoding direction was aligned to cover the deep layers of the cortical regions of interest (**Supplementary Fig. 2b**) as previously described[10]. To reduce the potential aliasing effect along the phase-encoding direction, we used two saturation slices to nullify the signal out of the FOV as previously established for line-scanning fMRI[5]. The 2D FLASH slice image was reconstructed from the reshuffled *k*-space data with a 100-ms sampling rate[9]. As described previously[10], the in-flow effect contributes little to the BOLD signal detected from individual venules. For CBV fMRI signal, the in-flow effect from blood with a high concentration of iron oxides would likely be negligible.

Single-vessel MGE imaging. To detect individual arterioles and venules, we used a 2D MGE sequence with the following parameters for 11.7 T: TR, 30 ms; TE, 1.8, 4.3, 6.8 or 9.3 ms; flip angle, 50°; matrix, 160 × 128; in-plane resolution, 75 × 75 µm; slice thickness, 500 µm. The following parameters were used for 14 T: TR, 50 ms; TE, 2.5, 5, 7.5, 10, 12.5 or 15 ms; flip angle, 40°; matrix, 192 × 128; in-plane resolution, 50 × 50 µm; slice thickness, 500 µm. A single-vessel map is acquired by averaging of the MGE images acquired from the second echo to the forth echo, where the venule voxels show as dark dots because of the fast T2* decay but arteriole voxels remain bright owing to the in-flow effect.

EPI fMRI. For the EPI sequence, FASTMAP shimming, adjustments to echo spacing and symmetry, and B_0 compensation were set up first. Using the single surface coil, we ran a single shot sequence with a 64 × 64 matrix with the following parameters: effective TE, 18/9.6 ms; TR, 0.8 s; bandwidth, 138/300 kHz; flip angle, 45°; in-plane resolution, 150 × 150; slice thickness, 500 µm. A 3D gradient-echo EPI sequence with a 64 × 64 × 32 matrix was run with the following parameters: effective TE, 16 ms; TR, 1.5 s; bandwidth, 170 kHz; flip angle, 12°; FOV, 1.92 × 1.92 × 0.96 cm. For fMRI studies, we placed electrodes on the forepaw or whisker pads of rats to deliver a 2.0-mA pulse sequence (300-µs duration repeated at 3 Hz) via an isolated stimulator[10] (A360LA; WPI). For optical stimulation, we used a 473-nm laser (CNI, China) with a built-in FC/PC coupler to deliver the light pulse. The light pulse was triggered through an analog module to deliver optical stimulation with different durations ranging from 0.3 ms to 20 ms. The multimode optical fiber was 200 µm (FT200EMT; ThorLabs). The light power from the fiber tips was calibrated using optical power meters (PM20A; ThorLabs) and was controlled from 0.3 to 10 mw. The power levels used for light-driven fMRI studies (2 s or 5 s, 10 Hz, 20-ms light pulse, 3.2 mw) did not induce pseudo-BOLD signal due to heating effects, as shown by testing in cortical regions both without and with ChR2 expression after the rats died.

The 2D slice covered the forepaw and barrel S1 areas as defined by the Paxinos atlas[28]. The horizontal slice angle was set at 15° and 40°, and the center of the slice was positioned 1 mm from the cortical surface to cover layers 4 and 5. For FLASH fMRI, the forepaw and whisker pad stimulation experiment consisted of 60 dummy scans to reach steady state followed by 10 prestimulation scans, 20 scans during electrical stimulation, and 100 scans after stimulation (a total of 13 s for each on/off epoch for three times). The total time for each trial was 42 min. Each trial was repeated three or four times for both BOLD and CBV fMRI mapping. After the second trial for the CBV fMRI study, a small dosage of iron oxide particles (3–4 mg/kg) was injected to compensate for the potential washout of iron particles from the blood. The single-vessel map was acquired at the same slice orientation for further imaging registration. For EPI-fMRI, the forepaw and whisker stimulation experiment consisted of 10 dummy scans to reach steady state followed by 10 prestimulation scans, 3 scans during stimulation and 12 interstimulation scans for 8 epochs or 20 prestimulation scans, 5 scans during stimulation and 20 inter- stimulation scans for 5 epochs. The pulse sequence–based trigger and stimulation control was established using the BioPac system (Goleta, USA) and AD instruments (Oxford, UK).

Animal surgeries. All animal work was performed according to the guidelines of the Animal Care and Use Committee and the Animal Health and Care Section of the National Institute of Neurological Disorders and Stroke, National Institutes of Health (NIH; Bethesda, MD, USA), and the protocol was approved by the Animal Protection Committee of Tuebingen (Regierungspräsidium Tuebingen). A total of 24 male Sprague- Dawley rats were imaged at 2–3 months of age. Eight rats were imaged under 11.7 T (both BOLD and CBV FLASH fMRI data with A-V maps were acquired from five of eight rats) at NIH, seven rats were imaged under 14 T at the Max Planck Institute (both BOLD and CBV FLASH fMRI data with A-V maps were acquired from four of seven rats), and nine rats were imaged for optogenetic studies (both BOLD and CBV FLASH fMRI data with A-V maps were acquired from four of nine rats). The number of animals to be used was calculated by a power analysis with parameters acquired from our previous studies[5,10]. If a rat died during an fMRI experiment, the data acquired for that rat were not included in the statistical analysis.

Animal preparation for fMRI. The detailed procedure is described elsewhere[29]. Briefly, rats were initially anesthetized with isoflurane. Each rat was orally intubated with a mechanical ventilator throughout the surgical and imaging procedures. Plastic catheters were inserted into the right femoral artery and vein to allow monitoring of arterial blood gases and administration of drugs (anesthetics and iron oxide particles). After catheterization, all rats were given an i.v. bolus of α-chloralose (80 mg/kg). Isoflurane was discontinued after 3–5 min. Constant infusion of α-chloralose was set with a rate of 26.5 mg/kg/h. The rats' rectal temperature was maintained at ~37 °C while they were in the magnet. Rats were secured in a head holder with a bite bar to prevent head motion. All relevant physiological parameters, such as end-tidal CO_2, rectal temperature, heart rate, and arterial blood pressure, were continuously monitored during imaging. Arterial blood gas contents were checked regularly, and adjustments were made by tuning respiratory volume or administering sodium bicarbonate to maintain normal pH levels when required. An i.v. injection of pancuronium bromide (4 mg/kg) was administrated to reduce motion artifacts upon request. BOLD and CBV fMRI were performed on α-chloralose anesthetized rats. CBV fMRI was performed directly after BOLD fMRI. CBV-weighted signals were obtained after intravenous administration of 15 mg of Fe/kg dextran-coated iron oxide (Biopal, MA).

Viral vector injection and fiber optic implantation. The viral vectors (AAV5.CaMKIIa.hChR2 (H134R)-eYFP.WPRE.hGH) were obtained from the University of Pennsylvania Vector Core. Three- to four-week-old rats were injected with 200 nl of original viral vector solution in the barrel cortex with stereotactic coordinates: bregma, −2.35 mm; lateral, −4.8 mm; and ventral, 1.5 and 0.7 mm. For the stereotactic injection procedure, rats were initially anesthetized with isoflurane. A small burr hole was drilled after the skull was exposed. A nanoliter injector (WPI, FL) was used to place the 35-gauge needle at the proper coordinates in the stereotactic frame. Injections were performed slowly over 5–6 min, and the needle was slowly removed after being kept in the injection site for 10 min after the end of the injection. Within 5–6 weeks after the viral injection, a 200-µm fiber optic was inserted into the rat barrel cortex at stereotactic coordinates: bregma, −2.7 mm; lateral, −5.1 mm; ventral, 1.3 mm; tilt, 4°. The fiber optic was glued to the skull, and the skin around it was sutured after the glue had solidified (20–30 min).

In vivo electrophysiological recordings: Rats were placed in a stereotaxic frame for the in vivo recordings under similar anesthesia and surgical procedures to the fMRI experiments. The 200µm fiber optic was first inserted to target the barrel cortex previously injected with AVV viral vectors. The electrodes (Plastics One Inc, Roanoke, VA) was positioned to the barrel cortex (Bregma -2.7, lateral −5.1, and ventral 0.8 mm, tilt 5-6°). The intact whisker pad was electrically stimulated at 2.0mA (3Hz 300µs) by an isolated stimulator (A360LA, WPI). Or, the barrel cortex was directly activated by the light pulse exposure (0.3-20ms, 1, 3Hz, 10Hz, and 0.3 to 20mw). Stimulation trigger were delivered through the M150 Biopac system using the STM100C stimulator module with 10K sampling rate. The evoked potential was acquired through the EEG module of the Biopac system (gain factor: 5000, the band-pass filter 0.1-100 Hz). Mean profiles of evoked potential responses were subsequently obtained by averaging over the entire series with a time-window step of 300ms (synchronized to the start of a stimulation pulse). AcqKnowledge software package (Biopac Systems) was used to calculate the averaged profiles of evoked potential responses.

Animal perfusion and brain slice microscopic imaging: Immediately after the fMRI imaging, rats were deeply anesthetized with sodium pentobarbital (60mg/kg, per rat, subcutaneous admin- istration)). Then, animals were secured dorsally, and an incision was made along the chest. The heart was exposed, by incising through the rib cage and diaphragm. The left ventricle was be punctured with a sterile catheter, the right atrium was cut to allow fluid to drain, and heparanized saline was fed into the heart with a

© 2016 Nature America, Inc. All rights reserved.

doi:10.1038/nmeth.3765

perfusion pump. After the saline, 4% paraformaldehyde, 10% buffered formalin was fed into the heart. After perfusion, the brain was carefully extracted from the skull and frozen. A 30-µm brain slice was cut from the frozen rat brain using a cryostat (Leica-CM1860, Wetzlar, Germany). The floating slice was mounted on a glass slide with a coverslip. Fluorescent imaging was done using a Zeiss Axio Imager 2 (Zeiss, Göttingen, Germany).

Image processing and statistical analysis. Data analysis for both FLASH and EPI-fMRI data was performed using Analysis of Functional NeuroImages (AFNI) software (NIH)[30]. The relevant source codes can be downloaded at http://afni.nimh.nih.gov/afni/. A detailed description of the processing is provided elsewhere[10].

The FLASH fMRI data stored in the *k*-space format (**Supplementary Fig. 2**) were first reshuffled with a Matlab script for reconstruction using the built-in function of the Bruker Paravision software. For the AFNI analysis, a 2D registration function was first applied to register the reconstructed FLASH images to a template for multiple data sets acquired with the same orientation setup. To register the FLASH fMRI images with the single-vessel maps, we used the tag-based registration method. Ten to twelve tags were chosen from venule voxels distributed around the 2D slices of FLASH and single-vessel images. We normalized all time-series FLASH fMRI images by scaling the baseline images to 100. Multiple trials of block-design time courses were averaged for each animal. No smoothing procedure was included in the image-processing steps so that the single-vessel fMRI signal could be determined from the high-resolution FLASH fMRI images. The hemodynamic response function (HRF) was derived via linear regression using a tent function.

$$f(x) = \begin{cases} 1 - |x| \; for -1 < x < 1 \\ 0 \; for \; |x| > 1 \end{cases}$$

The tent function is also called “piecewise linear spline”, which is used for deconvolution of the HRF response with magnitude estimated as beta coefficient.

$$H(t) = \sum_{k=0}^{n} \left(\beta_k * \left(\frac{t - k * L}{L} \right) \right)$$

Or,

$$\mathrm{H(t)} = \beta_0 \times T(t/L) + \beta_1 \times T((t-L)/L) + \beta_2 \times T((t-2L)/L) + \cdots + \beta_k \times T((t-kL)/L)$$

Here $H(t)$ is the HRF response, k is the total number of tent parametric fittings, β_k is the response (tent height) at time $t = kL$ after stimulation, and L is the tent radius (L can be equal to TR). The value of β was calculated to estimate the amplitude of the fMRI response at each TR (L = TR). The voxel-wise β-map is presented to illustrate the spatial pattern of the fMRI response at different time points after the stimulus onset.

The individual arterioles and venules were characterized on the basis of the signal intensity of the voxels detected in the single-vessel map. We created the single-vessel map by averaging the MGE images from the second echo to the forth echo. The individual

doi:10.1038/nmeth.3765

vessel voxels were determined on the basis of their signal intensity, interpreted as either higher (arterioles) than the mean signal intensity plus two times the s.d. or lower (venules) than the mean signal intensity minus two times the s.d. of the local area in a 5 × 5 kernel[31] (**Supplementary Fig. 6a**). A 3dLocalstat function from the AFNI library was used to normalize the signal intensity of single-vessel maps. This allowed us to plot the BOLD and CBV β-values of all voxels to the normalized signal intensity of A-V maps (**Fig. 1d**,**e**). In addition, we performed a 2D spatial correlation between the single-vessel maps and the corresponding BOLD and CBV fMRI functional maps using the Matlab script corr2. The fMRI onset profile was determined on the basis of the full hemodynamic response function. As previously reported, a two-gamma-variate fitting step was applied to estimate the onset time from the averaged and normalized fMRI signal[5,30,32].

$$f(x) = \mathrm{a}\left(\frac{x}{pq}\right)^{p} \times e^{(p-(x/q))} - \mathrm{b}\left(\frac{x}{rs}\right)^{r} \times e^{(r-(x/s))}$$

where x is the variable and a, p, q, b, r and s are the coefficients for the two-gamma-variate function.

The two-gamma-variate function with optimized coefficients was fit to the hemodynamic responses of individual voxels. The fitting curve was plotted with the raw BOLD and CBV hemodynamic signals from individual vessels (**Fig. 3** and **Supplementary Figs. 9–12**). The mean r^2 value for each individual fitting of venule BOLD and arteriole CBV signal is shown for individual rats in a scatter plot (**Supplementary Fig. 13**). The ttp and FWHM were estimated from the fitting function. The onset time was derived from a t_0 coefficient from the modified two-gamma-variate function (3dNLfim function with ConvDiffGram module), which showed a reliable estimate of the hemodynamic signal onset in comparison to the noise threshold–based onset estimates[5].

Finally, Student's t-test was performed for group analysis; error bars indicate the standard error of the mean in graphs. No blinding design was needed in this work.

28. Paxinos, G. & Watson, C. The Rat Brain in Stereotaxic Coordinates 6th edn. (Academic Press, 2006).
29. Yu, X. et al. Neuroimage 49, 1667–1676 (2010).
30. Cox, R.W. Comput. Biomed. Res. 29, 162–173 (1996).
31. Qian, C. et al. Am. J. Physiol. Renal Physiol. 307, F1162–F1168 (2014).
32. Madesen, M. Phys. Med. Biol. 37, 1597–1600 (1992).

© 2016 Nature America, Inc. All rights reserved.

doi:10.1038/nmeth.3765

Erratum: Sensory and optogenetically driven single-vessel fMRI

Xin Yu, Yi He, Maosen Wang, Hellmut Merkle, Stephen J Dodd, Afonso C Silva & Alan P Koretsky

***Nat. Methods*; doi:10.1038/nmeth.3765; corrected online 29 February 2016**

In the version of this article initially published online, color labels in **Figure 1f** were erroneously switched. The error has been corrected for the print, PDF and HTML versions of this article.

© 2016 Nature America, Inc. All rights reserved.

Supplementary Figures (13)

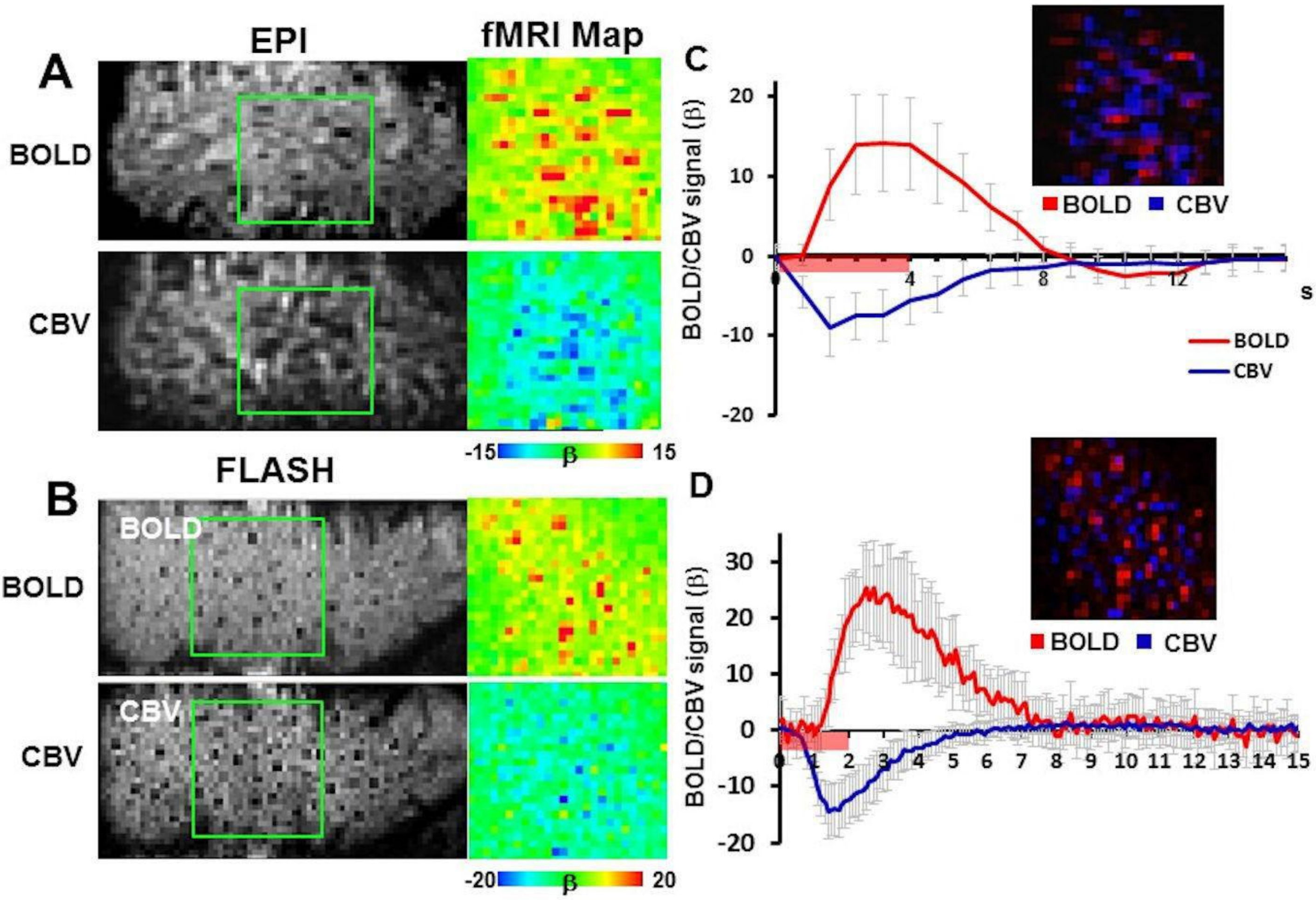

Supplementary Figure 1

BOLD and CBV functional maps showing EPI versus line-scanning FLASH fMRI.

A. Colored BOLD and CBV functional maps are shown in the highlighted window (green frame) of the raw EPI images (representative of 3 rats). **B**. Colored BOLD and CBV functional maps are shown in the highlighted window (green frame) of the raw FLASH images (representative of 5 rats). **C and D**. The BOLD (red) and CBV (blue) fMRI time courses were averaged from the sparsely distributed voxels with β values at thresholds (BOLD, β ≥ 5; CBV, β ≤ -5, mean±SD).

doi:10.1038/nmeth.3765

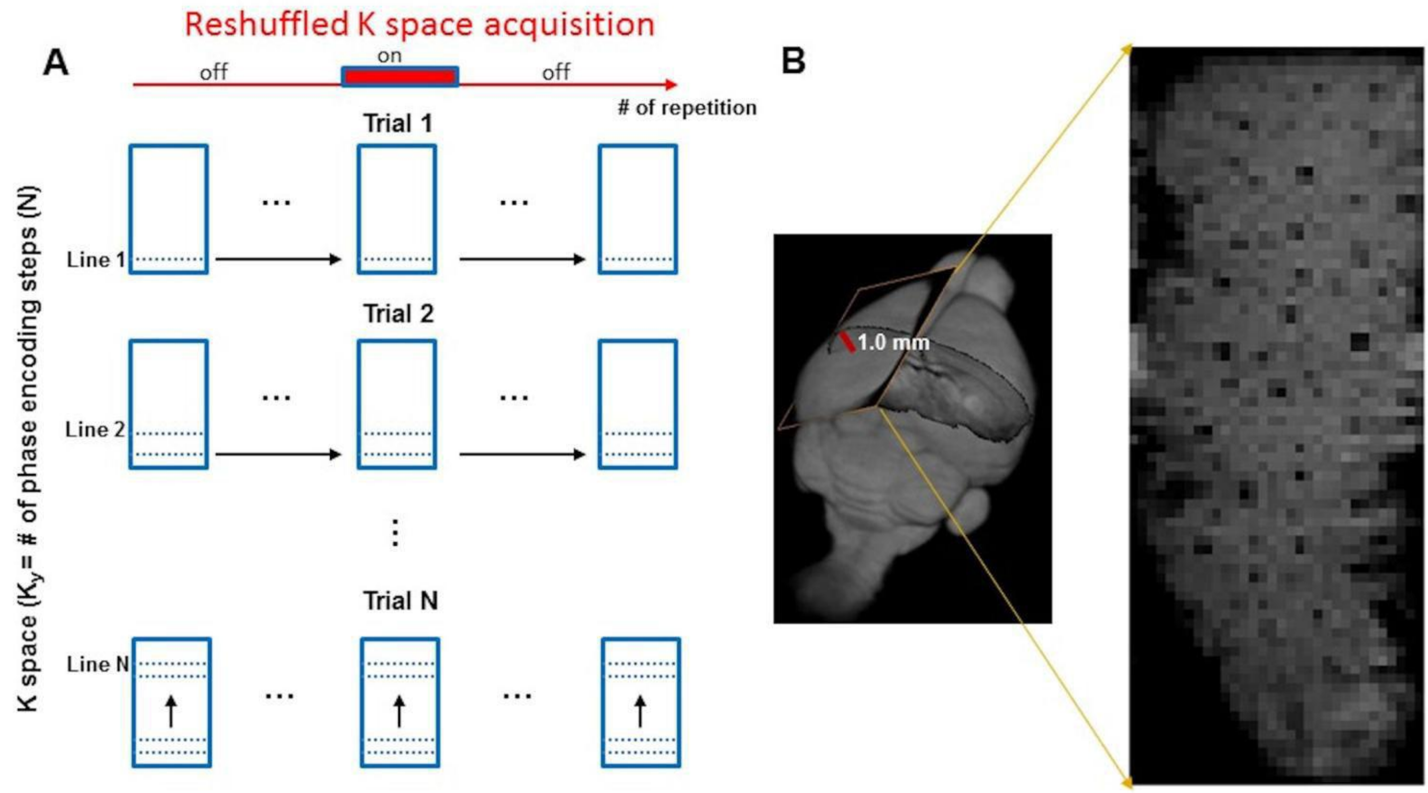

Supplementary Figure 2

The line-scanning–based FLASH fMRI method.

A. The overall view on the k-space acquisition of the FLASH-fMRI method. At each trial of the block-design experiment (red line), one k space line was acquired for each image. The k space for each image was filled with one line at each trial. Experimental trials were repeated for the number of phase-encoding steps (N=32/64). **B**. The k space map was reconstructed to produce the 2D image, which was located at the deep layer cortex (1.0mm to the cortical surface) covering the primary somatosensory cortex.

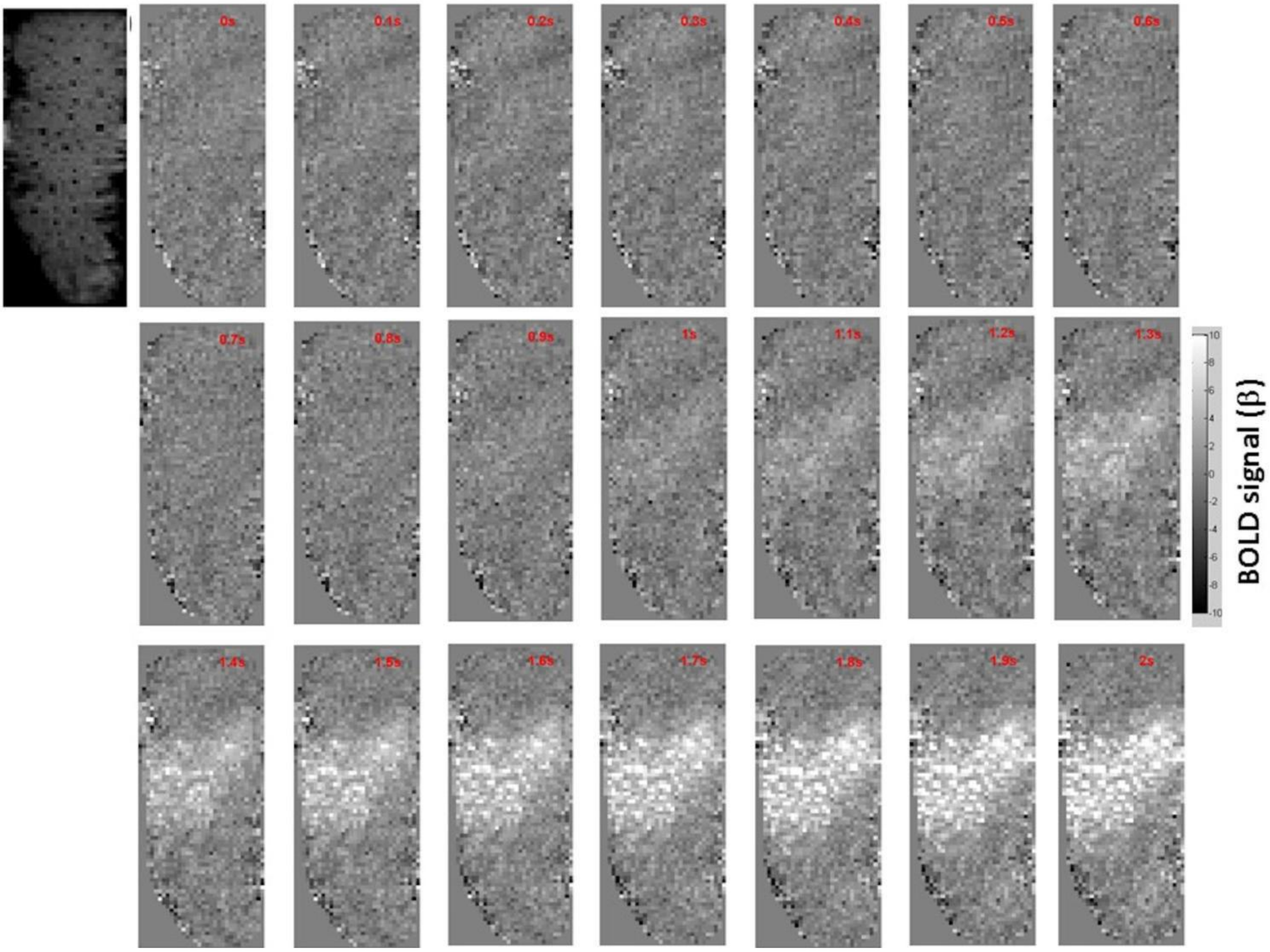

Supplementary Figure 3

Time-lapsed BOLD fMRI images with line-scanning fMRI.

The grey-scale BOLD functional maps are shown as the function of time at every 100ms from 0s to 2s following the stimulus onset. The raw image is shown in the upper left corner.

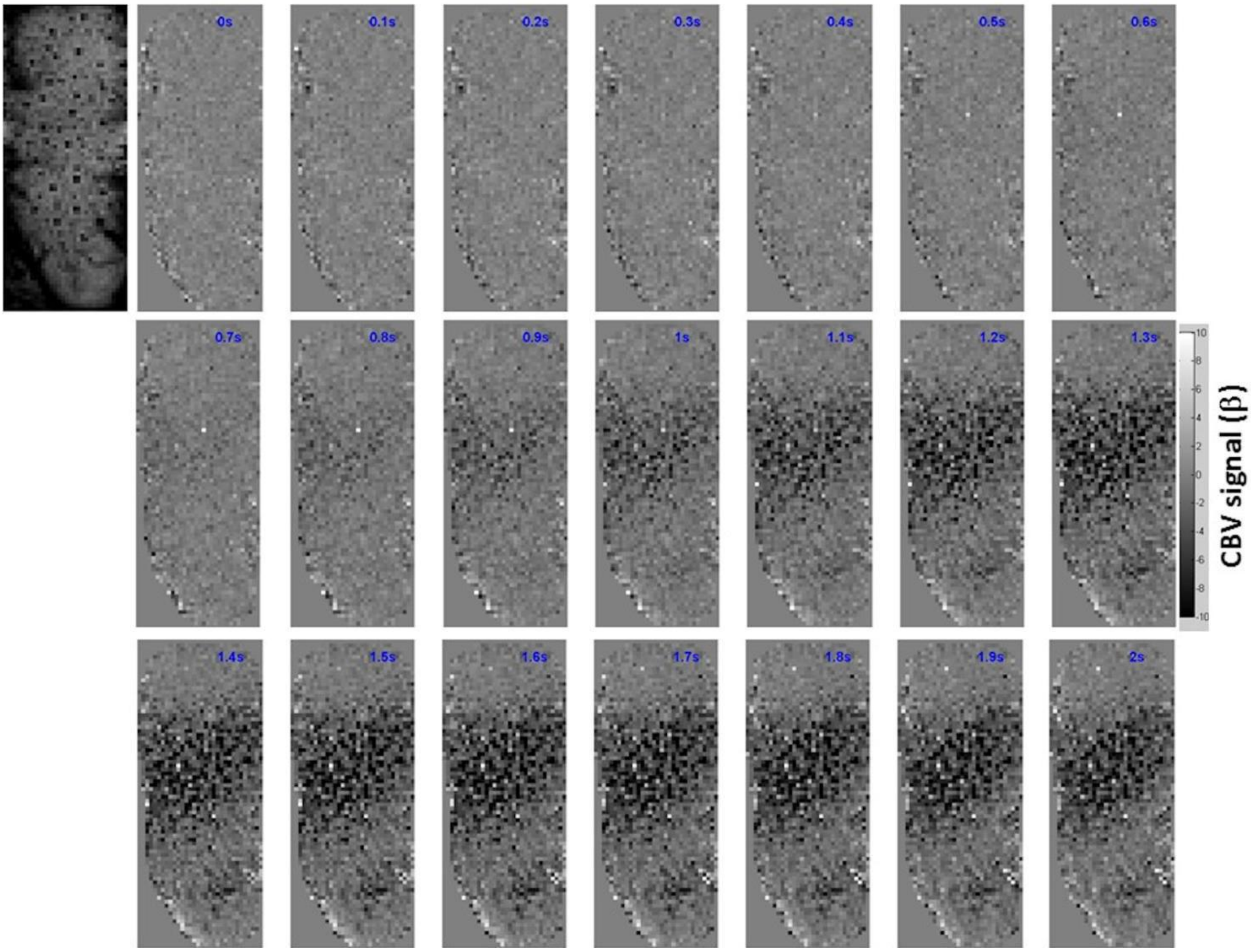

Supplementary Figure 4

Time-lapsed CBV fMRI images with line-scanning fMRI.

The grey-scale CBV functional maps are shown as the function of time at every 100ms from 0s to 2s following the stimulus onset. The raw image (after iron injection) is shown in the upper left corner.

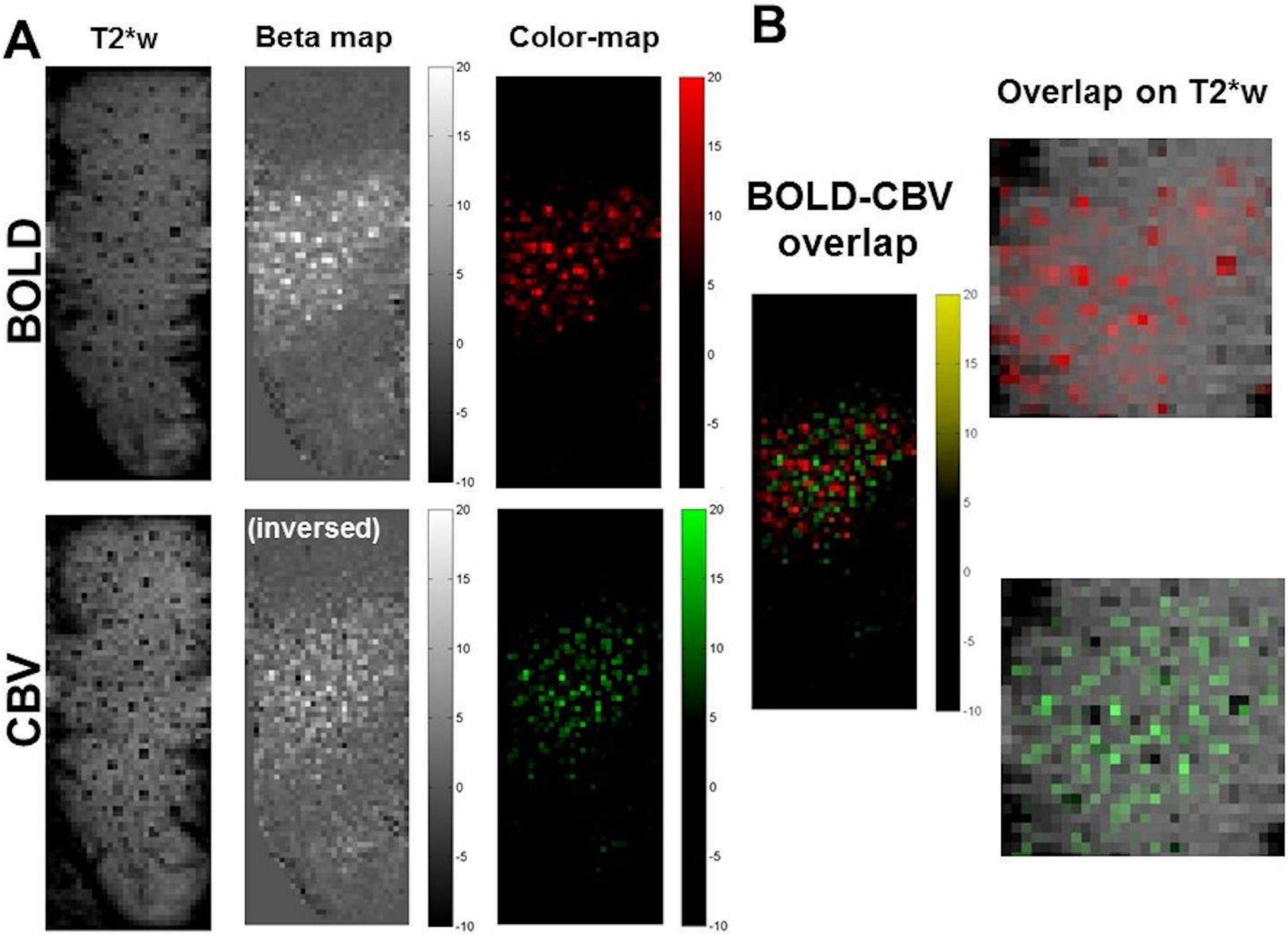

Supplementary Figure 5

Localization of BOLD and CBV fMRI voxels.

A. BOLD and CBV functional maps from the 2D anatomical image (T2*w) in gray-scale (middle) and color-scale (right; BOLD, red; CBV, green, inversed). **B.** The BOLD and CBV functional color-maps overlapped with the sparsely distributed active voxels in the same 2D slice (left). Both enlarged functional maps were overlapped on the anatomical T2*W images (right).

doi:10.1038/nmeth.3765

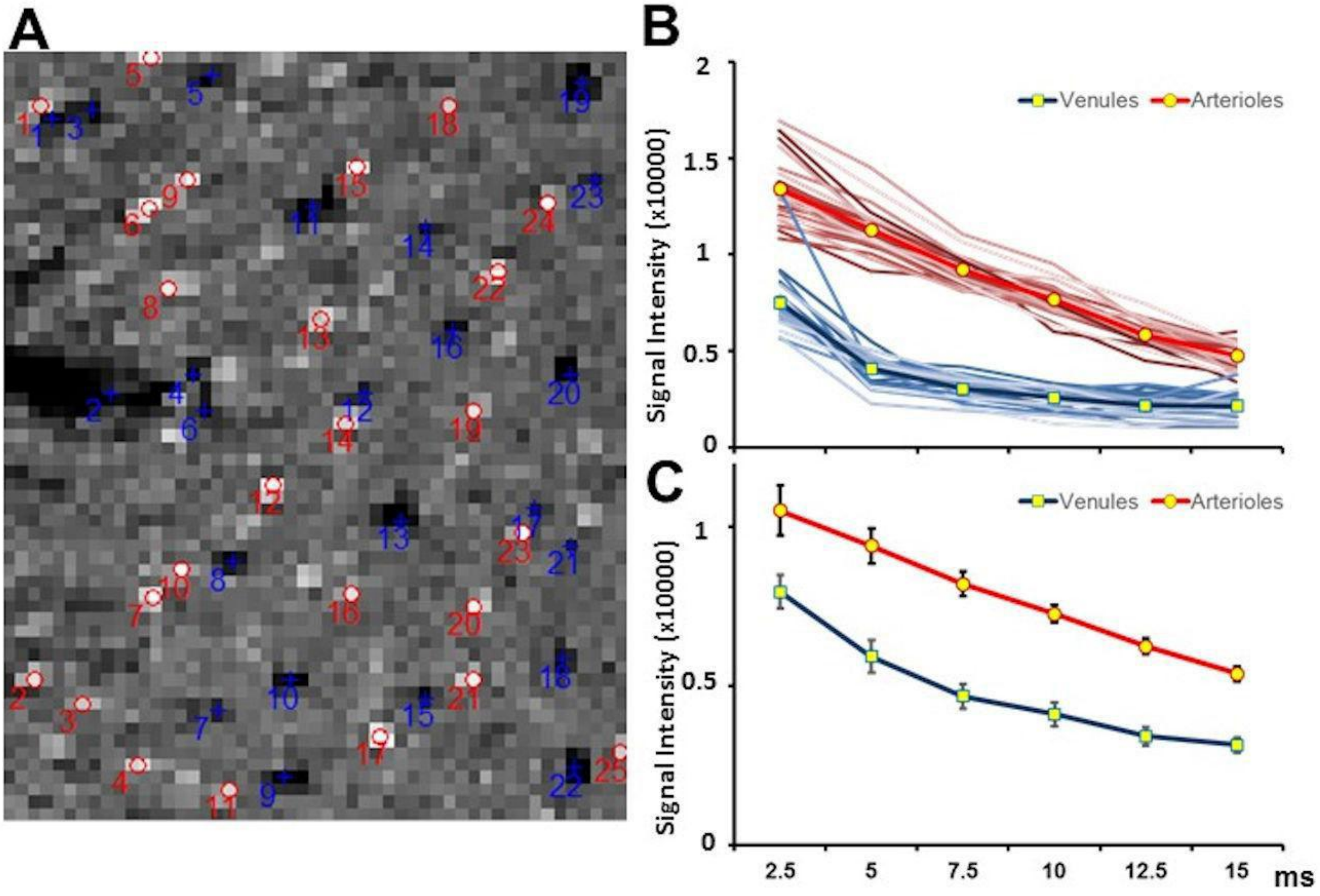

Supplementary Figure 6

The detection of individual penetrating arterioles and venules in the deep layer cortex.

A. The representative A-V map from 6 rats. The individual venules are shown as dark voxels (blue crosses). The individual arterioles are shown as bright voxels (red circles). **B.** The signal intensity of the venule (23) and arteriole (25) voxels was plotted as the function of different TEs from 2.5ms to 15ms (one representative rat from A. **C**. The averaged signal intensity of all venule and arteriole voxels was plotted as the function of different TEs (n=6, rats, mean±SEM).

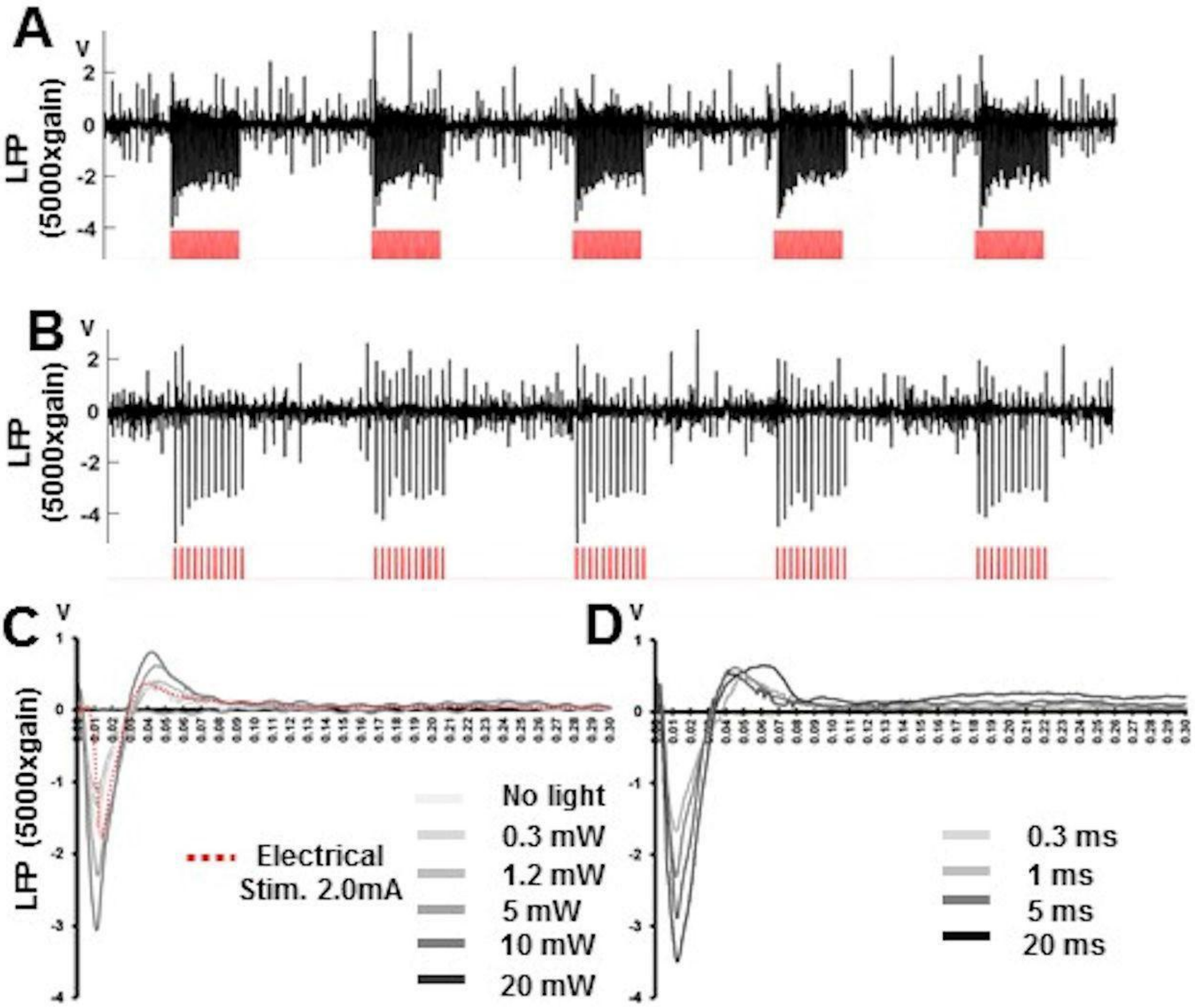

Supplementary Figure 7

The light-driven local field potential (LFP) by optogenetics.

A. The LFP trace by optical stimulation (upper panel: 1ms light pulse, 3Hz, 10mw; lower panel, 20ms light pulse, 1Hz, 10mw). **B**. The averaged LFP driven by 1ms light pulse at different power (0, 0.3, 1.2, 5, 10, 20 mw) and by electrical stimulation of the whisker barrel (2.0mA, 3Hz, 0.3ms, red dotted line). **C**. The averaged LFP driven by light pulse at different duration (0.3, 1, 5, and 20ms; 3Hz, 10mw).

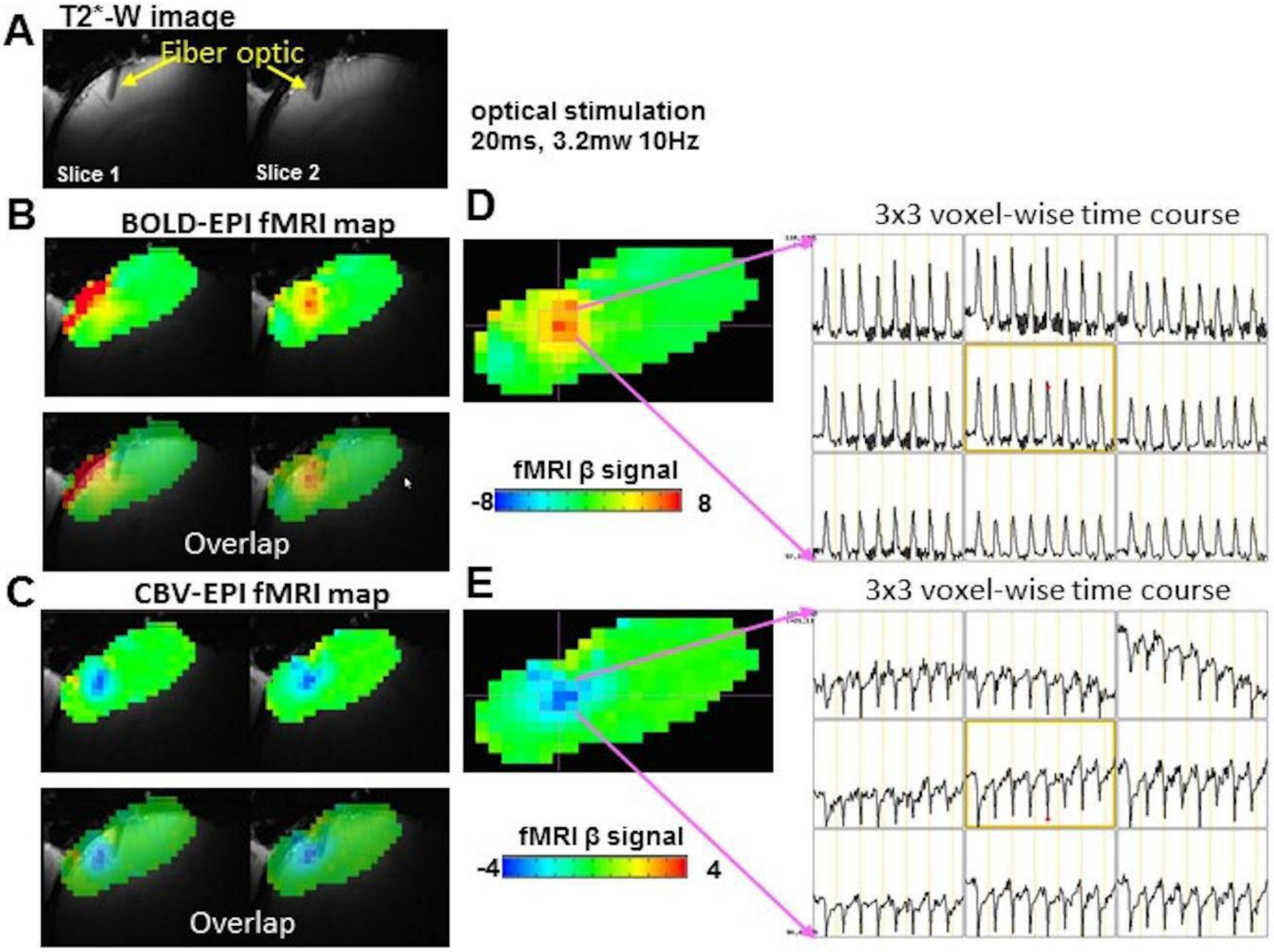

Supplementary Figure 8

Light-driven BOLD and CBV fMRI signal acquired by EPI methods.

A. The T2*-weighted images with the fiber optic inserted to target the barrel cortex in two consecutive slices. **B**. The colored BOLD fMRI maps show the most active voxels close to the fiber tip (upper panel) with anatomical image overlay (lower panel). **C**. The colored CBV fMRI maps show the most active voxels close to the fiber tip after iron oxide particle injection (upper panel) with anatomical image overlay (lower panel). **D**. The voxel-wise BOLD fMRI time courses (2s on/ 20s off, 8 epochs) plotted in a 3x3 matrix (the voxel position is shown in the colored BOLD-fMRI map, left). **E**. The voxel- wise CBV fMRI time courses (2s on/ 20s off, 8 epochs) plotted in a 3x3 matrix (the voxel position is shown in the colored CBV-fMRI map, left).

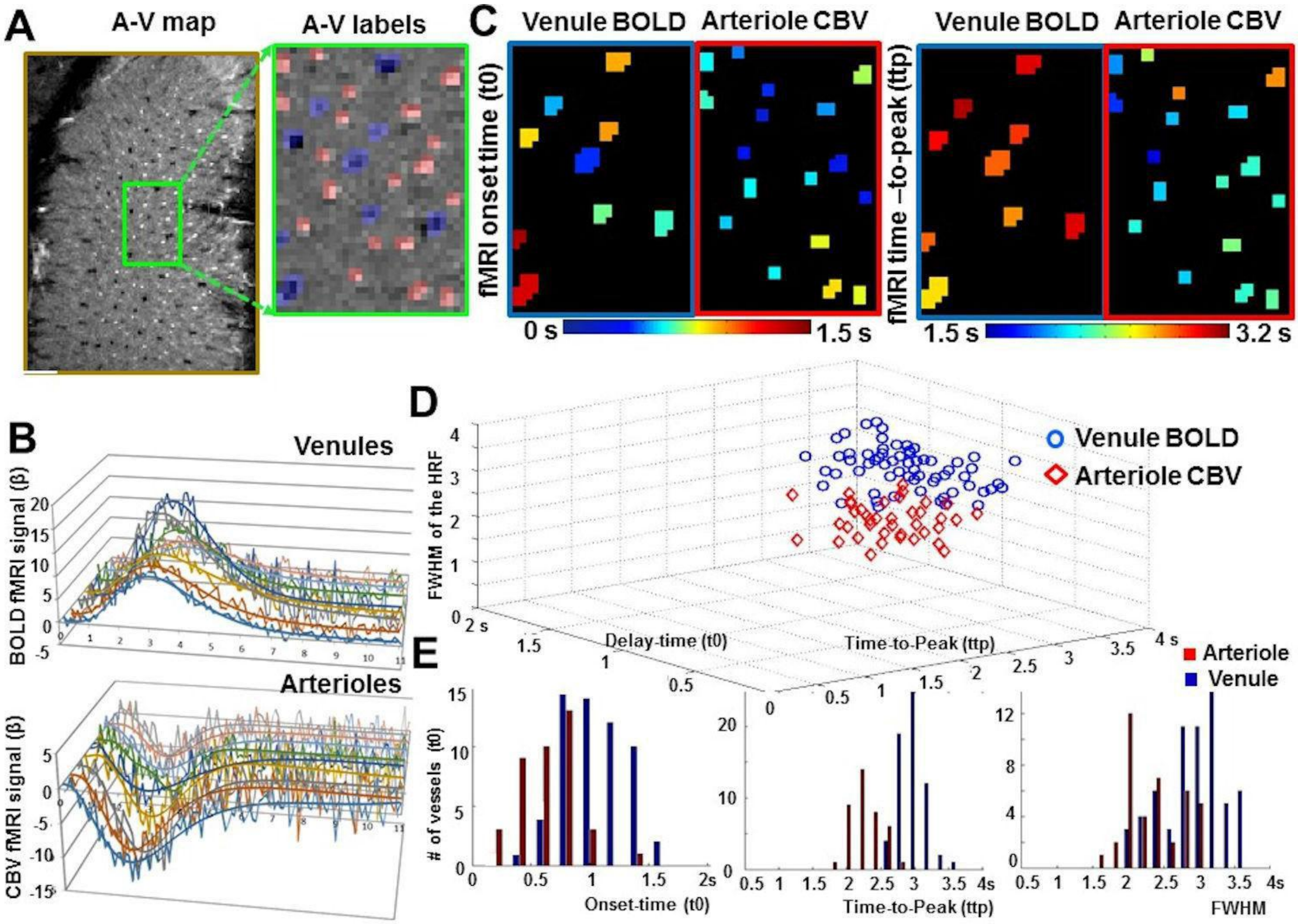

Supplementary Figure 9

The BOLD and CBV fMRI signal from individual arterioles and venules under 14.1 T.

A. A representative A-V map from 4 rats. The individual arteriole and venule voxels were detected with different signal intensity (venule voxels, blue; arteriole voxels, red). **B**. The BOLD fMRI time courses (raw data and fitting curves) from individual venule voxels(upper panel) and the CBV fMRI time courses (raw data and fitting curves) from individual arteriole voxels (lower panel). **C**. The fMRI onset time (t0) maps (left panel) and time-to-peak (ttp) maps (right panel) of a representative rat. **D**. 3d plots of the onset-time (t0), time-to-peak (ttp), and full-width-of-half-maximum (FWHM) of fMRI signal from individual arteriole (red diamonds, 39, $r^2>0.4$) and venule (blue circles, 63, $r^2>0.5$) voxels from 4 rats. **E**. Distribution of number of venule (blue) and arteriole (red) voxels with different t0, ttp and FWHM.

doi:10.1038/nmeth.3765

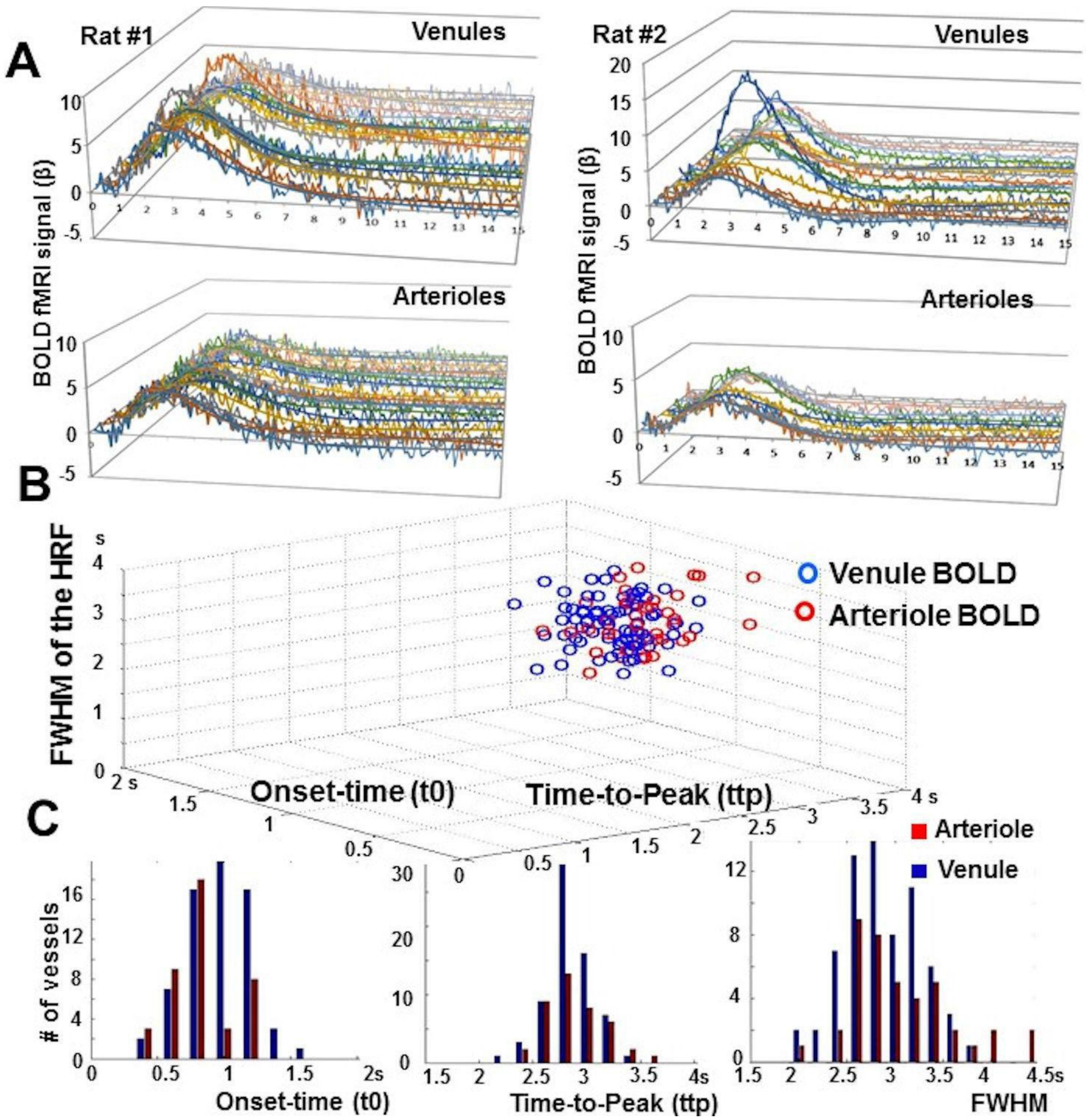

Supplementary Figure 10

The BOLD fMRI signal from individual arterioles and venules.

A. The BOLD fMRI time courses (raw data and fitting curves) of two representative rats from total 5 rats (venules, upper panel; arterioles, lower panel). **B**. 3d plot of the onset-time (t0), time-to-peak (ttp), and full-width-of-half-maximum (FWHM) of fMRI signal from individual arteriole (red circles, 41, $r^2>0.4$) and venule (blue circles, 71, $r^2>0.5$) voxels from 5 rats. **C**. Distribution of the number of venule (blue) and arteriole (red) voxels with different t0, ttp and FWHM.

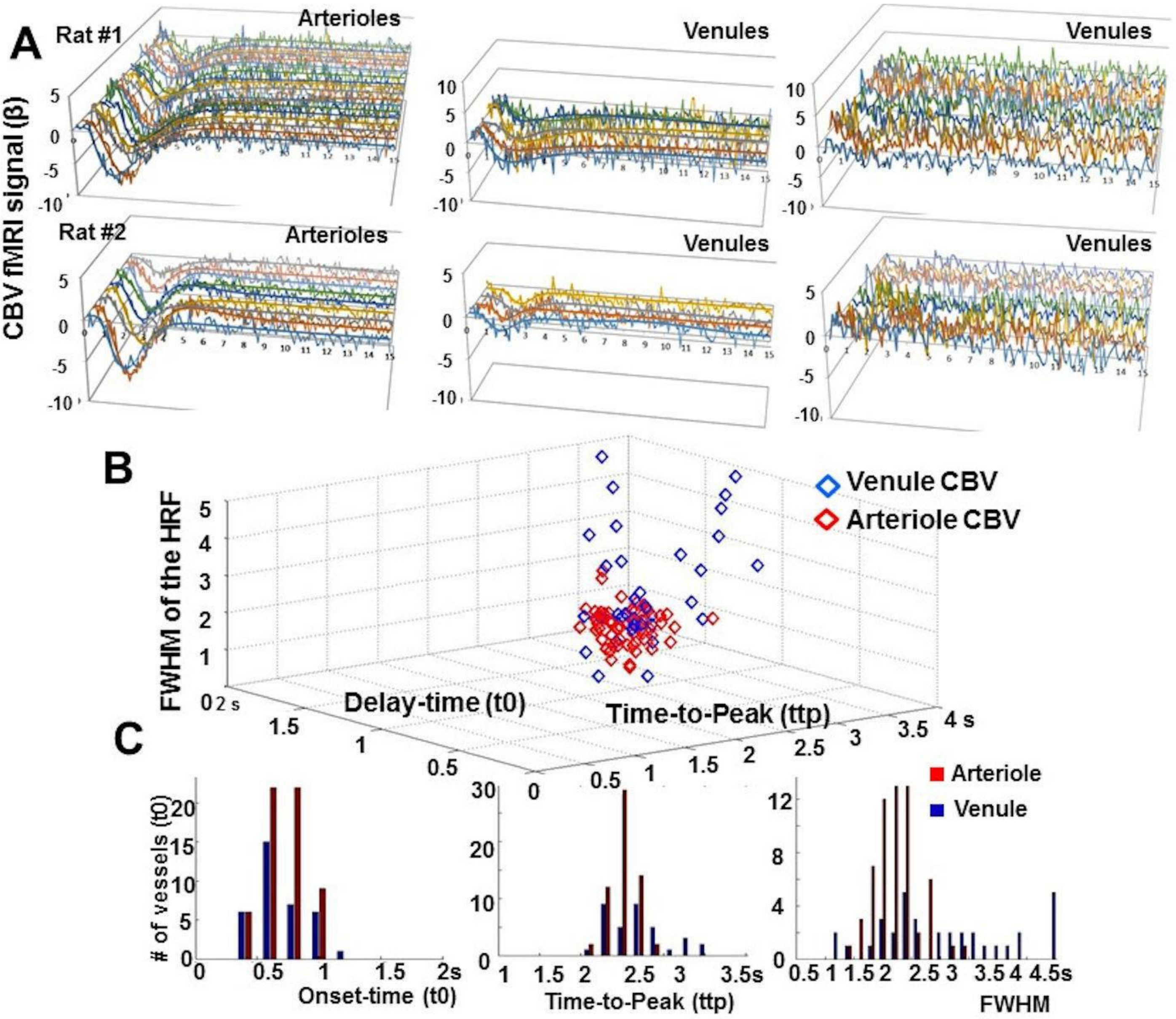

Supplementary Figure 11

The CBV fMRI signal from individual arterioles and venules.

A. The CBV fMRI time courses (raw data and fitting curves) of two representative rats from total five rats (arterioles, left; venules, middle, $r^2>0.2$, right, $r^2 \leq 0.2$). **B**. 3d plot of the onset-time (t0), time-to-peak (ttp), and full-width-of-half-maximum (FWHM) of fMRI signal from individual arteriole (red diamonds, 59, $r^2>0.4$) and venule (blue circles, 35, $r^2>0.2$) voxels from 5 rats. **C**. Distribution of number of venule (blue) and arteriole (red) voxels with different t0, ttp and FWHM.

doi:10.1038/nmeth.3765

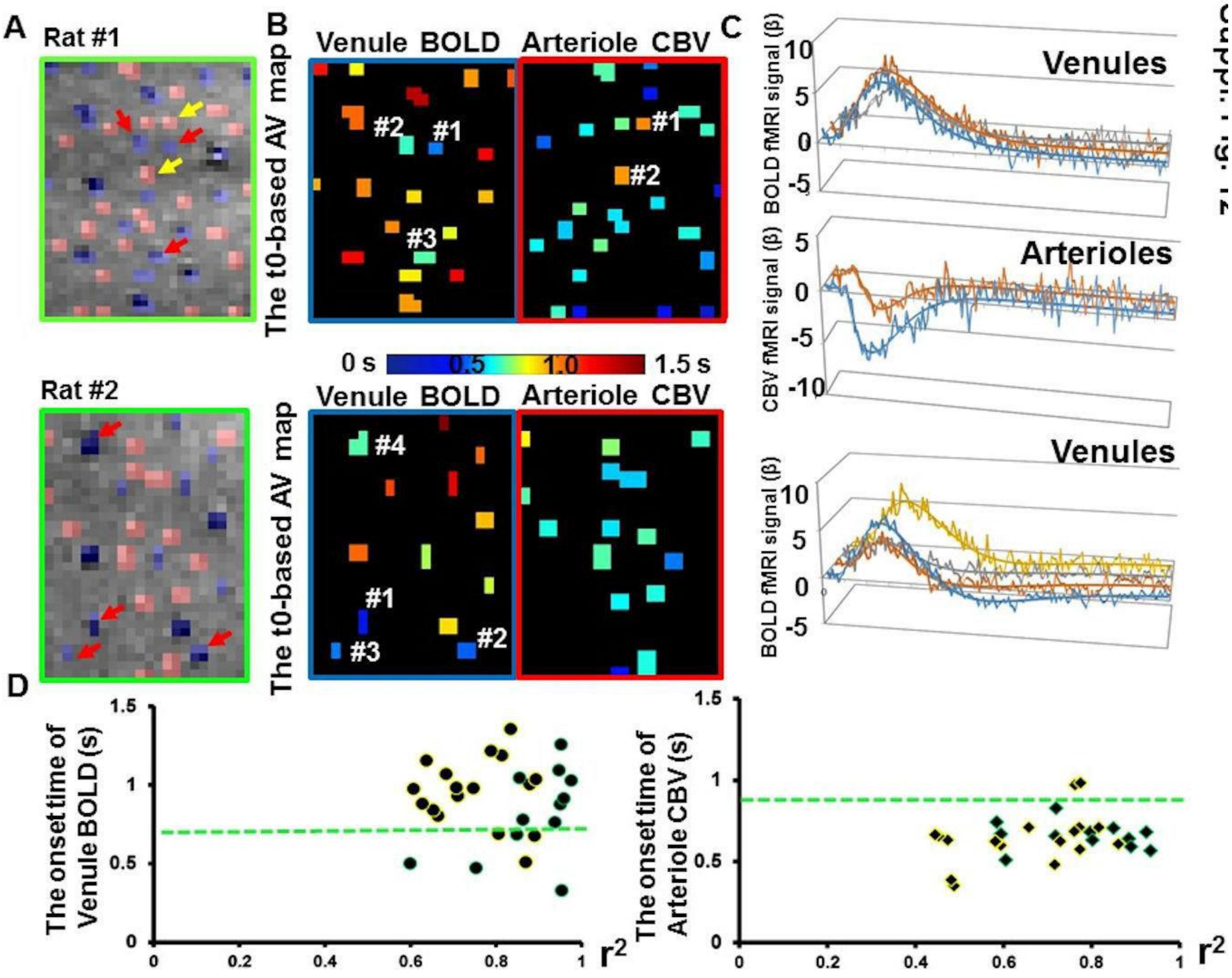

Supplementary Figure 12

The spatial and temporal characterization of the outlier vessel hemodynamic signal.

A. The A-V maps of two representative rats (red arrows for venule outliers, yellow arrows for arteriole outliers). **B**. The onset-time (t0) based A-V maps showed the BOLD t0 values of different venules and CBV t0 values of different arterioles of two representative rats (the outlier vessels are marked in numerical numbers). **C**. The time course of the hemodynamic signal from the outlier vessel voxels and their fitting curves. **D**. The scatter plot of the venule BOLD (left, dots, green line: 0.7s) and arteriole CBV (right, diamonds, green line: 0.9s) t0 values with the fitting r^2 values (rat #1, yellow borders, rat #2, blue borders).

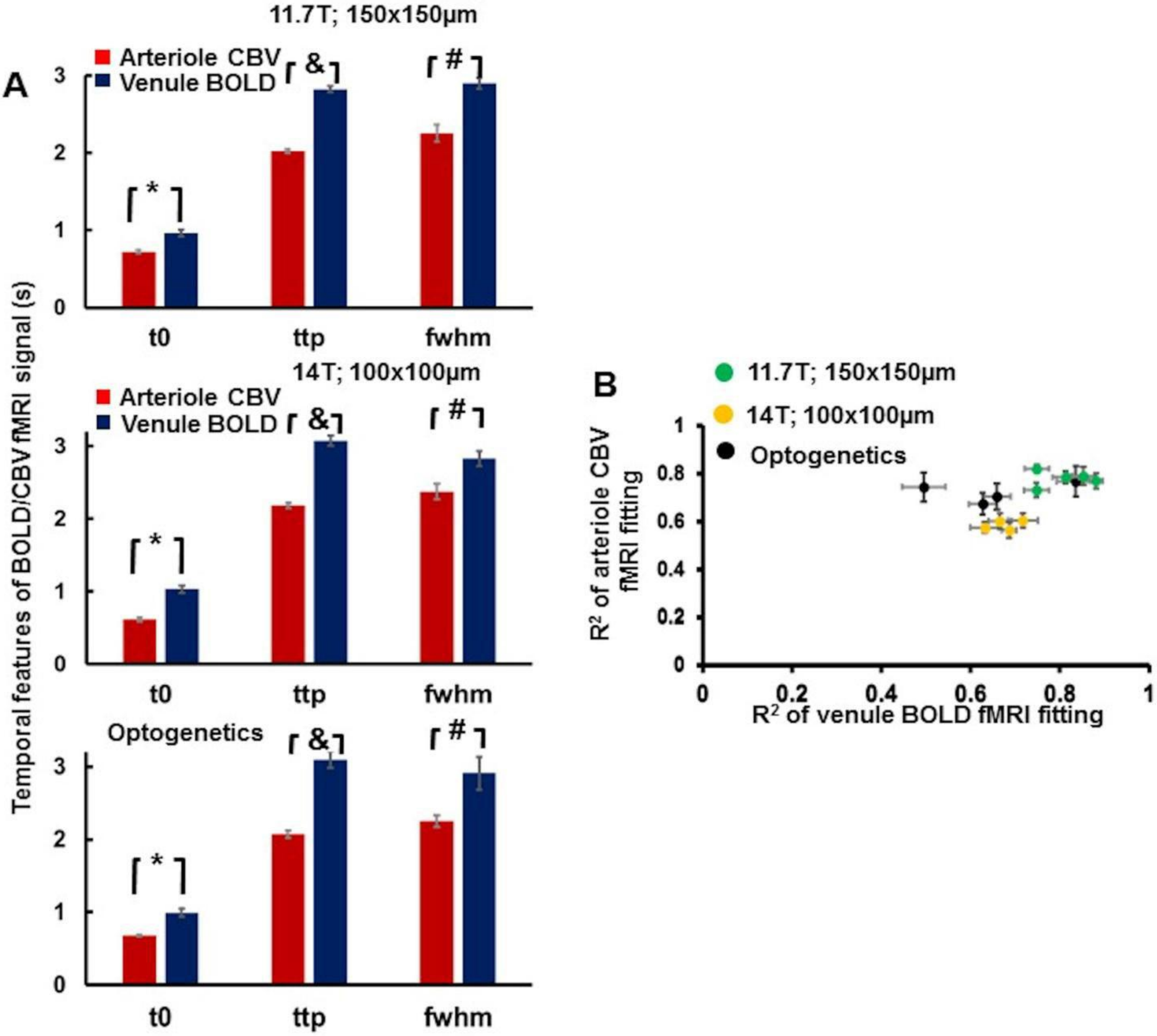

Supplementary Figure 13

Group analysis of BOLD and CBV fMRI signals from individual vessels.

A. The averaged onset time(t0), time-to-peak (ttp), and full-width-of-half-maximum (FWHM) from arteriole CBV signal (red) and venule BOLD signal (blue) acquired from 11.7T (top panel; n=5; * p=0.002; & p=0.00001, # p=0.002), 14.1T (middle panel, n=4; * p=0.002; &, p=0.0006; # p=0.01), and driven by optogenetic method under 14.1T (bottom panel; n=4; * p=0.01; & p=0.002, # p=0.04. **B**. The averaged r^2 values of all individual vessels were plotted for each rat of two experiments (11.7T: green, n=5, 14.1T: yellow, n=4; optogenetics: dark, n=4; error bar is ±SEM). Students’t-test was used for statistical analysis.

Supplementary Table

MR Scanner	Experiments	Vessels	Onset time (t0)	Time-to-Peak (ttp)	Full width of half Maximum (FWHM)
11.7T	Sensory input (n=5)	Venules	0.96 ± 0.04s	2.82 ± 0.04s	2.90 ± 0.07s
		Arterioles	0.72 ± 0.02s	2.02 ± 0.03s	2.26 ± 0.11s
14T	Sensory input (n=4)	Venules	1.03 ± 0.05s	3.08 ± 0.07s	2.83 ± 0.10s
		Arterioles	0.63 ± 0.03s	2.29 ± 0.03s	2.27 ± 0.11s
	Optogenetics (n=4)	Venules	0.99 ± 0.06s	3.10 ± 0.11s	2.91 ± 0.22s
		Arterioles	0.67 ± 0.01s	2.07 ± 0.05s	2.25 ± 0.08s

Supplementary Table 1. The mean t0, ttp and FWHM of hemodynamic signal evoked by sensory stimulation and optical stimulation with optogenetics. The values are mean ± SEM.

Supplementary Note

Supplementary results

In Supplementary Figure 1, cerebral blood volume (CBV) fMRI signal was acquired with EPI, after injecting iron oxide particles, to compare to BOLD signal. In the mid-cortical layers mapped with the same slice orientation, the most active CBV voxels did not overlap with active BOLD voxels, which were previously assigned to the penetrating venules (Supplementary Fig 1A). This preliminary result indicated that CBV signal originated from different vascular components than the BOLD signal from mid-cortical layers of somatosensory cortex. However, there are limitations to distinguishing vessel-specific BOLD and CBV signals using the long echo train of EPI due to image distortion. In addition, the short TR to get high temporal sampling leads to low signal-to-noise ratios (SNR) with long TE after the injection of iron oxide particles. To overcome these limitations, a single k-space line scanning technique was used to build up high resolution anatomical and functional images[1].

Here, the line-scanning based FLASH-fMRI method was used to map BOLD and CBV fMRI signal from a 2D slice perpendicular to the vessels penetrating the mid-cortical layers of somatosensory cortex (Supplementary Figure 2, Supplementary video 1). The short TE (~4ms) used for detection of CBV with iron oxide particles reduced the field distortion by the iron particles in the blood to get more accurate anatomical images. This short TE remains sensitive to T2*-weighted signal changes at the high field used. The CBV and BOLD signal can be mapped directly onto the anatomical images due to less distortion from the FLASH acquisition as compared to the EPI images (Supplementary Figure 3, 4). The spatial pattern of the most active CBV voxels was clearly separated from the most active BOLD voxels from penetrating venules(Supplementary Figure 5). However, the anatomical source of the active CBV voxels has not been clarified. This work motivated us to develop the single-vessel fMRI method to clearly map the fMRI signal from individual arterioles or venules penetrating the deep layer cortex.

doi:10.1038/nmeth.3765

The detailed discussion of the vessel-specific hemodynamic signal detected by single vessel fMRI method.

An issue for this work is how to best extract individual vessel-specific hemodynamic signals. In addition to averaging all venule or arteriole voxels from multiple subjects (Supplementary Figure 13), the individual vessel responses and their spatial and temporal hemodynamic features could be characterized directly (Fig 3). Of the measures made arterioles could be very well separated from venules based on the time-to-peak differences of CBV in arterioles vs. BOLD in venules. Interestingly, there were a few venules that showed very fast BOLD onset times. As shown in Supplementary Figure 12, there were seven venules from two rats with onset times (t0) estimated shorter than 0.7s. In addition, there were two arterioles with onset times longer than 0.9s. These specific vessel onsets might be due to misassignment of the types of vessels. Re-examination of the signal in the anatomical images used to label the A-V map indicated that two of the seven venules showed only slightly lower signal intensity than the surrounding voxels just passing the threshold for identification as venules. However, the other five venule voxels demonstrated large signal drops in the A-V maps, indicating that they were likely assigned correctly. In addition, the two arterioles voxels with slow onset times were readily identified by bright spots in the A-V map. The r^2 of the hemodynamic signal fitting of the total nine vessels fell within the normal distribution of the r^2 of all the vessels detected indicating that the parameters extracted came from good fits to the data. Therefore, the fast onset venules and slow onset arterioles were not likely due to incorrect localization of the venule or arteriole voxels or to poor data fitting. Fast onset times of venules are likely due to a short capillary distance from arteriole to venule or to fast responding arterioles that feed the fast responding venules. It is clear that the temporal characteristics of vessel responses to neural activity can be measured and opens the possibility of studying changes due to aging and disease such as stroke or Alzheimer’s disease.

The final challenging issue raised by the work is to understand the extravascular effects on single-vessel fMRI mapping that are well known to occur with BOLD and CBV fMRI signals. It is unclear whether the BOLD signal detected from the arteriole voxels arose from the arterioles or were due to extravascular effects from nearby venule BOLD signals. Similarly, any CBV detected on venule voxels could be due to extravascular effects from arterioles. Since very few venules showed any CBV effect at all this is a smaller problem with CBV. One way to distinguish whether signals are independent is to analyze time courses to compare different vessel types (Supplementary Figure 10, 11). The vessel t0 distribution histogram showed that 75% of the arterioles analyzed had a BOLD onset time shorter than 1s, but 60% of the venules had a BOLD onset time equal or longer than 1s. The group analysis of the mean t0 of arteriole and venules BOLD showed that the arteriole BOLD was significantly shorter than the venule BOLD (Mean t0: arteriole, 0.82±0.03s; venules, 0.96±0.04s, $p=0.035$, two-tail paired t-test, $n=5$). This result indicated that there was likely some BOLD effect in arterioles. This result of a shorter BOLD onset in arteriole voxels compared to venule voxels is consistent with a previous report showing that the tissue voxels (arterioles and capillaries) had earlier onset than the macro-venule voxels[2]. However, it could be that the 40% venule voxels with earlier onset time than 1s contributed to the arteriole BOLD signal through extravascular effects. Therefore, it is difficult to conclusively assign the early BOLD onset signal from the present study. It should be possible to do quantitative modeling based on the geometry of the vessel and the data to be more quantitative about the origins of the BOLD signals in non-venule voxels. It was observed that the majority of venule voxels did not show any CBV signal in response to the relatively short stimuli used in this study. Only a few venules had a CBV response (Supplementary Figure 11). The venule CBV signal could come from extravascular effects from nearby arterioles. There is evidence that longer stimulation leads to a venous balloon effect and so it may be that a longer duration of stimulation would lead to changes in venule CBV with different temporal features[3, 4]. In addition, the SNR of the venule voxels after injection of iron particles is significantly reduced and the fitting r^2 value for venule CBV signal (r^2>0.2) is much lower than the fitting to other data (Supplementary Figure 13). The large variability of the FWHM can be caused by the low contrast-noise-ratio of the venule CBV signal. An alternative methodological improvement for CBV studies is to implement the arterial spin labeling or VASO approaches so CBV could be measured without introducing iron oxide particles and T2* extravascular effects would be minimized[5-8]. However, blood spin labeling approaches are predicted to give smaller signal changes and would not give the vessel size amplification that T2* based methods give making it challenging to image arterioles. Nevertheless, the fact that in-flow effects could be used to assign arterioles does give some hope to using VASO or other arterial spin labeling strategies.

Reference

1. Yu, X., Qian, C., Chen, D.Y., Dodd, S.J. & Koretsky, A.P. Deciphering laminar-specific neural inputs with line-scanning fMRI. *Nature methods* **11**, 55-58 (2014).
2. Yu, X. et al. Direct imaging of macrovascular and microvascular contributions to BOLD fMRI in layers IV-V of the rat whisker-barrel cortex. *Neuroimage* **59**, 1451-1460 (2012).
3. Silva, A.C., Koretsky, A.P. & Duyn, J.H. Functional MRI impulse response for BOLD and CBV contrast in rat somatosensory cortex. *Magnetic resonance in medicine : official journal of the Society of Magnetic Resonance in Medicine / Society of Magnetic Resonance in Medicine* **57**, 1110-1118 (2007).
4. Buxton, R.B. Dynamic models of BOLD contrast. *NeuroImage* **62**, 953-961 (2012).
5. Lu, H. & van Zijl, P.C. A review of the development of Vascular-Space-Occupancy (VASO) fMRI. *NeuroImage* **62**, 736-742 (2012).
6. Moon, C.H., Fukuda, M. & Kim, S.G. Spatiotemporal characteristics and vascular sources of neural-specific and -nonspecific fMRI signals at submillimeter columnar resolution. *NeuroImage* **64**, 91-103 (2013).
7. Huber, L. et al. Cortical lamina-dependent blood volume changes in human brain at 7 T. *NeuroImage* **107**, 23-33 (2015).
8. Detre, J.A., Leigh, J.S., Williams, D.S. & Koretsky, A.P. Perfusion imaging. *Magnetic resonance in medicine : official journal of the Society of Magnetic Resonance in Medicine / Society of Magnetic Resonance in Medicine* **23**, 37-45 (1992).

4.2 A.2 Directly mapping the single-vessel hemodynamic signal with Multi-echo Line-scanning fMRI (MELS-fMRI)

Directly mapping the single-vessel hemodynamic signal with Multi-echo Line-scanning fMRI (MELS-fMRI)

He, Y., Wang, M., Yu, X.

Journal of Cerebral Blood Flow and Metabolism, 2017, under revision.

Directly mapping the single-vessel hemodynamic signal with Multi-echo Line-scanning fMRI (MELS-fMRI)

Yi He[1,2], Maosen Wang[1,2], Xin Yu[1*]

[1]Translational Neuroimaging and Neural Control Group, High Field Magnetic Resonance Department Max Planck Institute for Biological Cybernetics, Tuebingen, 72076, Germany
[2]Graduate Training Centre of Neuroscience, International Max Planck Research School, University of Tuebingen, Tuebingen, 72074, Germany

* Corresponding author: Dr. Xin Yu, Email: xin.yu@tuebingen.mpg.de.

Acknowledgments

This research was supported by funding of the DFG SPP 1665 and internal funding from the Max Planck Society. We thank Dr. Pohmann, R., Dr. Merkle H., and Buckenmaier, K. for technical support. We thank Ms. Schulz, H. and Fischer, S. for animal maintenance support. We thank Schluesner J. and Pais-Roldán P for proofreading the manuscript. We thank the AFNI team for the software support.

Keywords:

BOLD, single-vessel fMRI, vascular dynamics, hemodynamic signal, arterioles, neurovascular coupling

Abbreviations:

fMRI, functional magnetic resonance imaging; BOLD, blood oxygen level dependent; EPI, echo planar imaging; CNR, contrast to noise ratios; DTI, diffusion tensor imaging; TE, echo time; T0, Onset-time; TTP, Time-to-Peak; FWHM, full-width-of-half-maximum; MELS-fMRI, Multi-Echo Line-Scanning fMRI; A-V, Arteriole-Venule; peri-arteriole, peripheral-arteriole; peri-venule, peripheral-venule.

ABSTRACT

Besides mapping large-scale functional activity, fMRI detects the vascular dynamics of distinct cerebrovascular components in brains noninvasively. Here, a 2D multi-echo line-scanning fMRI (MELS-fMRI) method has been modified to distinguish the hemodynamic features of the fMRI signal from individual arterioles and venules penetrating the deep layer cortex. The fMRI signal is acquired at different echo-times (TE, 3-30 ms) with a 100 ms sampling rate. Venule voxels dominate the T_2*-weighted blood-oxygen-level-dependent (BOLD) signal, indicating the increased extravascular effect as the function of TE. Arteriole voxels show the T_1-weighted fMRI signal at 3 ms TE with earlier onset than venules voxels, which could be caused by the increased blood inflow and volume effects. At longer TEs, arteriole and peri-arteriole voxels illustrate a positive fMRI signal because the arteriole-specific BOLD and the extravascular effect from neighboring venules overcome the intrinsic negative effect of arteriole dilation. Meanwhile, by measuring the T_2* value from multi-echoes, the T_2*-based fMRI signal reveals the earlier fMRI onset and time-to-peak of arteriole than venule voxels. The MELS-fMRI method detects the vessel-specific TE-dependent fMRI signal, which extends the single-vessel dynamic mapping in small animals and assists the optimization of quantitative fMRI modeling of the human brain.

INTRODUCTION

High-field fMRI is utilized to map brain function non-invasively (Ogawa et al., 1990; Belliveau et al., 1991; Bandettini et al., 1992; Kwong et al., 1992; Ogawa et al., 1992; Kim and Ugurbil, 2003). High spatial resolution MR images are acquired under high magnetic field with sufficient signal-to-noise ratio (SNR) to better locate the fMRI signal coupled with brain function (Yacoub et al., 2001; Hu and Norris, 2004; Harel et al., 2010; Duyn, 2012). This advantage inherent in high field fMRI makes it possible to detect functional cortical columns (Menon et al., 1997; Grinvald et al., 2000; Kim et al., 2000; Cheng et al., 2001; Duong et al., 2001; Fukuda et al., 2006; Yacoub et al., 2008), as well as the laminar specific fMRI signal in animal and human brains (Polimeni et al., 2010; Siero et al., 2011; Goense et al., 2012; Yu et al., 2012; Moon et al., 2013; Shih et al., 2013; Yu et al., 2014; Huber et al., 2015; Heinzle et al., 2016). Recently, high field fMRI studies have mapped the fMRI signal from individual vessels penetrating the cortex of rat and cat brains in the deep cortical layers (Yu et al., 2012; Moon et al., 2013). In contrast to the BOLD signal primarily located at penetrating venules, the iron oxide particle-based cerebral blood volume (CBV) fMRI signal is detected mainly at penetrating arterioles (Yu et al., 2016). These studies indicate that fMRI can be used to directly map the vessel-specific hemodynamic signal in the cerebrovascular network.

The hemodynamic microvascular origin of fMRI signal has been better characterized by optical methods in small animals. By measuring the absorption spectral changes of oxy-deoxyhemoglobin (Malonek and Grinvald, 1996), the blood oxygen content changes of cortical vessels closely correlate with the evoked neural activity (Devor et al., 2003). Using two-photon microscopic imaging, the laminar and temporal features of neural activity-coupled arteriole dilation or pericyte-controlled capillary dilation can be further linked to the fMRI signal (Tian et al., 2010; Hall et al., 2014; Uhlirova et al., 2016). Recently, the BOLD fMRI signal was quantitatively modeled by measuring the oxygen saturation distribution from reconstructed 3D cerebrovasculature of rodent brains (Gagnon et al., 2015), showing a step forward in the interpretation of a fMRI signal based on hemodynamic signal propagation. However, few measurements directly link fMRI signal to its microvascular origin close to the neuronal source. The concurrent optical measurement of the hemodynamic responses with fMRI has revealed strong temporal correlation, but it is limited to the surface cortical vessels (Jezzard et al., 1994; Kennerley et al., 2005). In contrast, the high-resolution single-vessel fMRI method could directly characterize the vascular hemodynamic features of the fMRI signal, indicating great potential to decipher the neurovascular signaling through the cerebrovasculature directly by using fMRI.

In this study, a multi-echo acquisition scheme was implemented to the line-scanning fMRI method, i.e. multi-echo line-scanning fMRI (MELS-fMRI). The line-scanning method originates from the pioneer work of Mansfield *et al*(Mansfield et al., 1976). To construct MR images, each k-space line is acquired consecutively along the block design paradigm and the on/off stimulation trials are repeated for the number of phase-encoding steps (Silva and Koretsky, 2002; Yu et al., 2016). Since only one k-space line is acquired per echo, the acquisition window could be significantly reduced to 1-2 ms, which is much shorter than the readout echo train (10-20 ms) of the EPI method. The short acquisition window not only avoids the long echo train-induced extra T_2*-weighting under the high magnetic field, but also shortens the minimal TE(Lee et al., 1999; Hyde et al., 2001; Duong et al., 2003; Goense and Logothetis, 2006; Yu et al., 2012; Budde et al., 2014). Thus, the MELS-fMRI method can sample the T_1 or T_2* weighted fMRI signal at different TEs, as well as examine temporal features of the T_2*-based fMRI signal at the single vessel level. The vessel-specific fMRI signal could lead to better verification and optimization of fMRI quantitative models for human brain mapping.

MATERIALS AND METHODS

Animal preparation

All animal experiments were performed according to a protocol approved by the animal protection committee (Regierungspräsidium Tuebingen). FMRI experiments were performed on five male Sprague Dawley rats. All procedures are described in a previous study (Yu et al., 2010). Rats were initially anesthetized with isoflurane (5% induction, 1.5% maintenance). Each rat was orally intubated and placed on a mechanical ventilator (SAR-830/AP, CWE Inc.). Plastic catheters were inserted into the right femoral artery and vein to allow monitoring of arterial blood gasses and administration of anesthetics. After surgery, each rat was given an intravenous bolus of α-chloralose (80 mg/kg) and isoflurane was discontinued. Anesthesia was maintained with a constant infusion of α-chloralose (26.5 mg/kg/h). The animals were placed on a heated pad to maintain rectal temperature at 37 °C while in the magnet. Each animal was secured in a head holder with a tooth-bar to prevent head motion. End-tidal CO_2, rectal temperature, tidal pressure of ventilation, heart rate, and arterial blood pressure were continuously monitored during the experiment. Arterial blood gas levels were checked periodically and corrections were made by adjusting the respiratory volume or administering sodium bicarbonate to maintain blood gas levels when required. An intravenous injection of pancuronium bromide (4 mg/kg) was given once per hour to reduce motion artifacts. Voluntary respiration-induced resonance offset reduced significantly following the administration of the pancuronium injection.

MRI image acquisition

All images were acquired with a 14.1 T / 26 cm horizontal bore magnet (Magnex), interfaced to an AVANCE III console (Bruker, Germany) and equipped with a 12 cm gradient set, capable of providing 100 G/cm with a rise time of 150 µs (Resonance Research). A transceiver surface coil with 6 mm diameter was used to acquire images.

Multi-Echo Line-Scanning fMRI (MELS-fMRI): A 2D Multiple Gradient Echo (MGE) sequence was modified to perform multi-echo line-scanning fMRI with the following parameters: TEs, 3 ms, 6.5 ms, 10 ms, 13.5 ms, 17 ms, 20.5 ms, 24 ms, 27.5 ms, 31 ms; TR, 100 ms; flip angle, 22°; matrix, 96 x 64; slice thickness, 400 µm; in-plane resolution, 100 x 100 µm. Two saturation slices were applied to suppress signal out of the Field of view (FOV) to reduce the potential aliasing effect along the phase-encoding direction. The frequency-encoding direction was set along the z0 direction towards the lung to reduce the respiration-induced resonance offset. The block-design stimulation paradigm was used in the MELS-fMRI experiment. The electrical stimulation was delivered by a stimulation isolator (AD Instruments) (2.0 mA, 300 µs pulses repeated at 3 Hz) through two needle electrodes that were inserted between digits of the forepaw. The block-design paradigm consisted of 60 dummy scans to reach steady state, followed by 10 pre-stimulation scans, 20 scans during electrical stimulation, and 100 scans post-stimulation (with a total of 13 s for each on/off stimulation experiment). For image acquisition, only one single-phase k-space line was acquired at each TE per 100 ms before the second set of k-spaces was filled during the block design trial (Supplementary Figure 1). Each trial consisted of 3 epochs of stimulation on/off design with total 390 TRs. The trials were repeated for the number of phase-encoding steps. The total duration was 40 minutes, and 3 - 6 MELS-fMRI trials were acquired for each rat.

The single-vessel Arteriole-Venule (A-V) map: A 2D Multiple Gradient Echo (MGE) sequence was used to detect individual arterioles and venules with the following parameters: TR, 50 ms; TEs, 2.5 ms, 5 ms, 7.5 ms, 10 ms, 12.5 ms, 15 ms, 17.5 ms; flip angle, 40°; matrix, 192 × 128; in-plane resolution, 50 µm × 50 µm; slice thickness, 400 µm. This slice orientation was perpendicular to the penetrating vessels and covered forepaw S1 areas based on the Paxinos atlas. The horizontal slice angle was set at 15° and the center of the slice was positioned 1.2 mm from the cortical surface to cover layer 5 (Fig. 1 A). Similar to the previous study (Yu et al., 2016), by averaging the MGE images acquired from the second echo to the fourth echo, the single-vessel A-V map showed the venule voxels as dark dots due to fast T_2* dephase, while arteriole voxels remained bright dots due to the in-flow effect. The individual vessel voxels were determined based on their signal intensity as either higher than the mean signal intensity plus 3 times standard deviation (arterioles) or lower than the mean signal intensity minus 3 times the standard deviation (venules) of the local areas in a 7x7 kernel. The venule voxels were colored blue while the arterial voxels were colored red (Fig. 1 A). After the vessel voxels were characterized, an “imdilate” Matlab function was used to select the voxels surrounding the vessel voxels specifically. To avoid the overlap of peri-vessel voxels from different vessel voxels, a dilating factor of 2 was chosen so as to set the expanded peri-vessel ROI with a width of 2 voxels (Fig. 2 C).

Image processing and statistical analysis

MELS-fMRI data analysis was performed using the “Analysis of Functional NeuroImages” (AFNI) (Cox, 1996) software (NIH) and MATLAB. The detailed description of the processing is provided in a previous study (Yu et al., 2014).

MELS-fMRI preprocessing: The MELS-fMRI 2D k-space data were first reordered with a Matlab script, and then reconstructed to MELS-fMRI images using a built-in function of Bruker Paravision software. For AFNI analysis, a 2D registration function was applied to align all MELS-fMRI images to a template for multiple datasets acquired in the same orientation setup. To register the MELS-fMRI images with the single-vessel map, a tag-based registration method was applied. Ten to twelve tags were chosen from the venule voxels distributed around the 2D slices of MELS-fMRI and single-vessel images. The baseline level of MELS-fMRI images was scaled to 100 and multiple trials of block-design time courses were averaged for statistical analysis. The hemodynamic response function (HRF) was estimated by the linear regression using tent basis function as previously reported(Yu et al., 2016).

T_2 Mapping*: T_2* values were calculated in voxel-wise by fitting the following exponential decay equation:

$$f(t) = S_0 \times \exp\left(-t / T_2^*\right) \qquad [1]$$

Where t is the time variable and S_0 is the initial signal intensity. T_2*-based fMRI signal was estimated based on the percentage change of the T_2* value from the baseline level scaled to 100.

Contrast-to-Noise Ratio (CNR): CNR (Geissler et al., 2007) was estimated based on the following equation:

$$CNR = (S_P - S_B) / \sigma_B \qquad [2]$$

Where S_P is the peak amplitude, S_B is the mean of baseline signal, and σ_B is the standard deviation of the baseline signal, respectively. The CNR of the fMRI signal at different echoes and T_2*-based fMRI signal were analyzed with one-way ANOVA followed by Tukey's multiple comparison tests.

Estimation of the hemodynamic temporal features of vessel-specific fMRI signal: A two-gamma-variate fitting process was used to fit the fMRI signal acquired from individual vessel voxels (Madsen, 1992).

$$F(t) = a \times (t/(p \times q))^p \times e^{p-t/q} - b \times (t/(r \times s))^r \times e^{r-t/s} \quad [3]$$

Where t is the temporal variable and a, p, q, b, r and s are the coefficients for two-gamma-variate-function. The onset time (T0) was measured as an intercept with the baseline by fitting one line to the rising slope between 20% and 80% of the peak amplitude estimated from the two-gamma-variate-function(Tian et al., 2010). The time-to-peak (TTP) and the full-width-of-half-maximum (FWHM) were estimated directly from the two-gamma-variate-function (Supplementary Figure 2).

A paired Student's t-test was performed to compare the mean signal intensity, T0, TTP, and FWHM of T_2* fMRI signal from the venule voxels and arteriole voxels. The error bar in each graph represents the standard error of the mean (s.e.m).

RESULTS

Mapping the T_2-weighted fMRI signal from arterioles and venules with MELS-fMRI*

Previously, the line-scanning method was applied to acquire a single k-space line along the on/off block design to map the fMRI signal with high spatial and temporal resolution(Silva and Koretsky, 2002; Yu et al., 2014; Yu et al., 2016). Here, multi-gradient echoes were implemented into the single-vessel fMRI method. In contrast to the multi-echo EPI-fMRI and FLASH-fMRI method (Menon et al., 1993; Chen and Wyrwicz, 1999; Weiskopf et al., 2005; Poser et al., 2006), the MELS-fMRI acquired only one k-space line for each echo at every TR during an on/off stimulation block design trial and the k-space was filled sequentially by repeating the fMRI block-design stimulation trials for the number of phase-encoding steps (Fig. 1 C). This acquisition scheme sampled fMRI signals from multiple echoes ranging from 3 ms to 30 ms at every 100 ms with an acquisition window for each echo in less than 1-2 ms.

The individual arterioles and venules penetrating the deep layer cortex could be directly mapped by an inflow based multi-gradient echo (MGE) sequence (Yu et al., 2016), which had been previously proposed for the human brain mapping to identify pial arteries and veins (Menon et al., 1993). For shorter TEs, both arterioles and venules with fast blood flow were detected as brighter voxels due to the inflow effect. In contrast, only venules were detected as darker voxels at the longer TE due to the fast T_2* decay of the deoxygenated venule blood at the longer TEs, but not the arterioles because of the similar susceptibility of the oxygenated blood to the surrounding parenchyma voxels. MGE images at different TEs were integrated into the arteriole-venule (A-V) map, demonstrating arterioles as bright dots and venules as dark dots (Fig. 1A). The size of penetrating vessels detected with the A-V map ranged from 30 to 70 microns (Yu et al., 2016). The vessel diameter was previously estimated based on vessel distance of the A-V map in comparison to the mean distance of penetrating vessels in the 3D reconstruction of the vascular network characterized by two-photon imaging (Blinder et al., 2010; Keller et al., 2011; Gagnon et al., 2015).

The same slice orientation was applied for both MELS-fMRI images and the A-V map so that the vessel-specific fMRI signal could be identified for individual arteriole and venule voxels penetrating the deep layer cortex. The primary somatosensory (S1) cortex was covered in the A-V map (Fig. 1A). Electrical stimulation of the forepaw elicited the fMRI signal, which could be detected by the MELS-fMRI method. Fig. 1B illustrates the T_2* decay curves of arteriole and venule voxels as a function of TE, which were acquired every 100 ms along the on/off block design. Fig. 1 D shows a 3d plot of decay curves along the stimulation on/off period during the block design (Supplementary Movie 1). At the stimulation-on period, the T_2*-weighted signal at different TEs of the decay curves increased, indicating that fMRI signal changes could be directly characterized through the multiple echoes with MELS-fMRI.

The detailed functional patterns were characterized with TEs from 3 ms to 20.5 ms with MELS-fMRI (Fig. 2 A, B, Supplementary Movie 2). The peak fMRI signal acquired at different echoes was located primarily on venule voxels. This was also demonstrated by comparing the peak amplitude of fMRI time courses detected from arteriole and venule voxels (Fig. 2 C). The other voxels, enriched with capillaries or small vessels not identified by the A-V map, showed higher fMRI peak amplitude than arteriole voxels, but lower than venule voxels at different TEs (Supplementary Figure 3). To better characterize the fMRI signal at different vascular components, the non-vessel voxels were further distinguished as parenchyma voxels surrounding arterioles, i.e. peri-arteriole voxels, and parenchyma voxels surrounding venules, i.e. peri-venule voxels. At short TEs, the peak fMRI signal matched well with the venules voxels detected in the A-V map, which could be caused by the oxy/deoxy-hemoglobin changes of the venule blood, i.e. the BOLD effect, since the venule blood has very short T_2 (Lee et al., 1999; Blockley et al., 2008). In contrast, the BOLD fMRI signal spread to peri-venule voxels due to the increased extravascular effect at the longer TE. The multi-echo scheme of MELS-fMRI made it possible to specify the extravascular effect on the functional patterns with different T_2* weighting, as well as the potential contribution from the T_1-weighted signal due to cerebral blood flow changes from arterioles. The peak fMRI signal from peri-arteriole and peri-venule voxels was extracted to compare with the arteriole and venule fMRI signal at different TEs (Fig. 2 C). Quantitative analysis demonstrated that the peak fMRI signal from peri-venule voxels was significantly higher than that of the peri-arteriole voxels at longer TEs from 10 to 20 ms (Fig. 2 D). In addition, the TE-dependent fMRI peak signal of the other non-vessel voxels showed similar amplitude to that of the peri-venule voxels (Supplementary Figure 4). These results indicated that the extravascular effect from venules could be directly measured from the peri-venule voxels and the other non-vessel voxels enriched with capillaries or small vessels using the MELS-fMRI method. In contrast, the peak fMRI signal of arterioles was significantly higher than that of the peri-arteriole voxels for shorter TEs (3 and 6.5 ms), but not for longer TEs (Fig. 2 E). This result indicated that the inflow effect due to activity-coupled cerebral blood flow and volume changes might directly contribute to the fMRI signal acquired at short TEs. Besides the peak fMRI signal, the fMRI signal acquired from 1 s to 2 s following stimulus onset was compared among arteriole, venule, peri-arteriole and peri-venule voxels at the short TE (3 ms) (Supplementary Figure 5). The early fMRI signal (e.g. 1 s, 1.2 s after stimulus onset) from arteriole voxels was significantly higher than that of the other voxels. These results indicated that the CBF/CBV dependent arteriole-specific fMRI signal could be detected by MELS-fMRI, which was independent of the BOLD effect dominating fMRI signal detected in venule voxels.

Analysis of the T_2-based fMRI signal from arterioles and venules with MELS-fMRI*

Besides the T_2^*-weighted fMRI signal at each TE, the T_2^* decay curves were fitted to estimate the T_2^* value for each voxel at every 100ms. Fig. 3 B demonstrates the T_2^* maps acquired at 2 s and 3 s after the stimulus onset. The estimated T_2^* values of venules voxels were much lower than the arteriole and non-vessel parenchyma voxels due to the high susceptibility of the deoxy-hemoglobin of venule blood. In contrast, the arteriole and non-vessel parenchyma voxels showed similar T_2^* values because of the similar susceptibility of arteriole blood with high concentration of oxy-hemoglobin to that of non-vessel parenchyma voxels enriched with capillaries or small vessels. Fig. 3 C illustrates the averaged time courses of T_2^* values of arteriole and venule voxels, which were highly consistent through the fitting curves from 6 to 10 TEs. Furthermore, similar to previous multi-echo EPI studies(Chen and Wyrwicz, 1999; Poser and Norris, 2009; Kundu et al., 2013), the contrast-to-noise ratios (CNR) of the T_2^* based fMRI signal changes were significantly higher than the T_2^*-weighted fMRI signal changes acquired at each echo for both arteriole and venule voxels (Fig. 3 D, E). In addition, the T_2*-based fMRI signal showed similar or higher CNR than that of the averaged T_2*-weighted image acquired at all TEs (Fig. 3 D, E). In contrast to the line-scanning single-vessel fMRI method, the multi-echo acquisition of MELS-fMRI allowed us to achieve higher CNR of the fMRI signal to better characterize the temporal hemodynamic features of individual arterioles and venules penetrating the somatosensory cortex.

The T_2*-based fMRI signal changes were characterized from individual arteriole and venule voxels. Similar to the T_2*-weighted functional maps acquired at different TEs (Fig. 2), the peak T_2*-based fMRI signal was primarily located at the penetrating venules (Fig. 4 B, Supplementary Movie 3). The vessel-specific temporal features of the T_2*-based fMRI signal could be characterized with the MELS-fMRI method. The time courses of T_2*-based fMRI signal with fitting curves were plotted from individual arteriole and venule voxels (Fig. 4 C). The averaged time courses of the T_2*-based fMRI signal showed an earlier onset from arteriole than venule voxels (Fig. 4 D). The T_2* value of arteriole voxels detected at 0.8 s after stimulus onset was significantly higher than that of venule voxels, which was reversed at later time points, e.g. at 1.8 s after the stimulus onset (Fig. 4 E, F). This result was consistent with a previous study using EPI-fMRI method to decipher the distinct vascular components contributing to BOLD-fMRI signal (Yu et al., 2012). The onset time (T0), time-to-peak (TTP) and full-width-of-half-maximum (FWHM) plots of the T_2*-based fMRI signal readily separated arteriole and venule responses into distinct clusters (Fig. 4 G). The T0 and TTP of the arteriole voxels were significantly shorter than those of the venule voxels (Fig. 4 H), demonstrating the potential hemodynamic signal propagation through the cerebrovasculature directly mapped by MELS-fMRI. Therefore, MELS-fMRI makes it possible to extract the unique hemodynamic features of the fMRI signal detected from individual arteriole and venules in the deep layer cortex.

DISCUSSION

The MELS-fMRI method offers two unique features when mapping the fMRI signal in the individual vessels in the brain. First is the very short acquisition window (1-2 ms) due to the single-phase line acquired per TR, which significantly shortens the minimal TE and excludes additional T_2* dephasing during echo acquisition. The other is the detection of vessel-specific fMRI signal from multi-echoes with high spatiotemporal resolution. In this study, the fMRI signal was acquired with the sampling rate at 10 Hz over a field of view up to 9 x 6 mm of the rat cortex. Although only penetrating vessels (>30 μm) were identified from the A-V map (Blinder et al., 2010; Keller et al., 2011), the vessel-specific fMRI signal could be directly mapped in the deep layer cortex up to 1-1.5 mm, which was beyond the conventional optical penetration depth(Yu et al., 2016). MELS-fMRI further extended the single-vessel mapping scheme to acquire fMRI signal at different TEs so that unique hemodynamic response features could be directly detected from fMRI signal with either T_1 or T_2* weighting. Although the line-scanning scheme elongated the total imaging time making it less practical for human brain mapping, the vessel-specific fMRI signal acquired at different TEs provided first-hand experimental data to optimize the vessel-specific quantitative modeling of the fMRI signal (Gagnon et al., 2015).

The MELS-fMRI method better characterized the intravascular and extravascular effect from the vessel and the surrounding parenchyma at different TEs. Consistent with previous experimental and model prediction studies (Yacoub et al., 2003; Jochimsen et al., 2004; Uludag et al., 2009; Gagnon et al., 2015), the extravascular effect from venules increased as the function of TE, which could be directly detected as largely spread fMRI signal from venules voxels to the surrounding voxels (Fig 2). In addition, the peak CNR of T_2*-weighted fMRI signal at venule voxels was detected at the TE similar to the T_2* value of venule voxels (Fig. 3E). The arteriole T_2* value did not match the TE with peak CNR of T_2*-weighted fMRI, which could be deviated by the extravascular effect of nearby venule voxels. In contrast to the extravascular effect, the direct measurement of the intravascular effect was more challenging given the limit of spatial resolution. The penetrating vessel size, characterized in the cortex by the single-vessel fMRI method or two-photon microscopy, ranged from 30 to 70 microns(Blinder et al., 2010; Yu et al., 2016). Despite the high spatial resolution, the fMRI signal from designated single-vessel voxels contained a good portion of partial volume effects from surrounding non-vessel parenchyma. Thus, the peak fMRI signal detected from the venule voxels remained partially extravascular-driven (Yu et al., 2012). However, for very short TEs, the intravascular effect from the venule blood could be approximately characterized given the very short T_2* value of the deoxygenated blood (Lee et al., 1999; Blockley et al., 2008; Gagnon et al., 2015). Though the fMRI signal detected at short TE might not be as specific as in the spin-echo scheme to exclude the extravascular effect by the refocusing pulse (Duong et al., 2003; Ugurbil et al., 2003; Yacoub et al., 2003; Jochimsen et al., 2004), the intravascular effect contribution to the venule voxels could be much higher for shorter TEs than for longer TEs. This intravascular effect could be better visualized on the venule voxels, showing a strong fMRI signal at the 3ms TE (Fig. 2).

One novel application of MELS-fMRI is to detect fMRI signal changes from individual arterioles at different TEs. In contrast to the BOLD signal acquisition with

EPI-fMRI, the direct CBV and CBF-based signal was not detectable without a specific mapping sequence, e.g. arterial spin labeling (Detre et al., 1992; Kim et al., 2007a) or vascular space occupancy (Lu et al., 2003), or injection with contrast agent for CBV (Belliveau et al., 1991; Lee et al., 2001; Kim and Kim, 2011). The fMRI signal detected by MELS-fMRI at short TEs from 3 ms to 6.5 ms depended more on the T_1-weighted effect for voxels covering parenchyma enriched with capillaries or small arterioles with oxygenated blood. The vessel-specific inflow signal over the saturation effect due to the lack of full relaxation under the short TR (100 ms) of MELS-fMRI led to significantly higher fMRI signal from the arteriole voxels compared to the peri-arteriole voxels (Fig. 2 E) (Kim et al., 1994). This could be directly caused by the increased CBF/CBV (Kim et al., 2007b) upon stimulation. Interestingly, even at the long TE we did not observe the CBV-induced decrease of BOLD-fMRI signal either at the arteriole or peri-arteriole voxels from the averaged time courses as suggested for fMRI predictive models(Uludag et al., 2009). The negative extravascular effect of arterioles on the BOLD signal was suggested to be caused by the susceptibility difference of arteriole blood from the surrounding tissue parenchyma (the baseline oxygen level of arteriole blood (95%) has similar susceptibility to surrounding tissue(Spees et al., 2001; Blockley et al., 2008), but evoked neural activity increases oxygen level of arteriole blood to induce susceptibility difference from surrounding tissue, which leads to decreased BOLD fMRI signal)(Uludag et al., 2009; Vazquez et al., 2010a). There are a few possible explanations to explain the discrepancy. First, Gagnon et al. detected that the oxygen levels of penetrating arterioles varied from 70 to 95% (Gagnon et al., 2015). Upon stimulation, the changes of susceptibility difference may vary from individual arterioles since not all arterioles with baseline oxygen level have similar susceptibility to surrounding tissues, which could cancel out the expected negative extravascular effect of arterioles. Second, the arteriole dilation could increase the volume contribution of blood with increased oxygen levels upon stimulation. The signal changes of the arteriole voxels are determined by both the susceptibility difference of arteriole blood from surrounding tissue and the susceptibility changes of arteriole blood with increased oxygen levels. Thirdly, the negative BOLD signal from arteriole or peri-arteriole voxels can also be concealed by the highly spread extravascular effect of venules as presented in Fig. 2. Altogether, multiple effects from the arteriole blood oxygen content, particle volume contribution, and the extravascular effects of nearby venules could lead to the lack of negative CBV contribution to the BOLD-fMRI signal detected in the present study.

Similar to previous multi-echo EPI studies (Chen and Wyrwicz, 1999; Poser and Norris, 2009; Kundu et al., 2013), the T_2*-based functional map showed much higher

CNR than the T_2*-weighted functional maps acquired at each TE (Fig. 3 D, E). The temporal features of the vessel specific hemodynamic signal can be better characterized to show earlier onset time of the arteriole T_2*-based fMRI signal (0.92 ± 0.03 s) than that of the venule T_2*-based fMRI signal (1.14 ± 0.03 s). The T_2*-based fMRI functional mapping represented more significant vessel-specific onset time difference compared to previous single-vessel T_2*-weighted fMRI studies (Yu et al., 2016), which could be due to the better CNR of the T_2*-based fMRI signal. Also noteworthy is that the time-to-peak of the T_2*-based fMRI signal from arterioles was significantly shorter than that of the venules. The T_2*-based early arteriole fMRI signal onset and time-to-peak could result from the oxy/deoxy-hemoglobin ratio changes detected in arterioles (Berwick et al., 2005; Hillman et al., 2007; Vazquez et al., 2010b), as well as from the CBF/CBV contribution at short TEs (Supplementary Figure 5). The onset time of fMRI signal detected by MELS-fMRI is similar to previous studies, indicating BOLD signal increased as early as 1s after stimulus onset in both cat and human visual cortex (Lin et al., 2013; Moon et al., 2013). Meanwhile, Silva *et al*. used an M-sequence and showed faster BOLD-fMRI onset with a mean time-to-peak less than 2.5s due to the short stimulation duration(Silva et al., 2007). Thus, the T_2*-based MELS-fMRI could better differentiate the temporal features of fMRI signal from arteriole and venule voxels than the T_2*-weighted fMRI acquired from the single echo (Yu et al., 2012; Yu et al., 2016).

In contrast to the EPI-fMRI with conventional Cartesian or Spiral trajectory to cover k-space, MELS-fMRI was less efficient and highly sensitive to motion artifacts. This is because the MELS-fMRI k-space was filled inconsecutively through the time series of the on/off block design. This line-scanning scheme leads to a great number of averaging of the fMRI signal across multiple blocks. Therefore, signal acquisition in real time in MELS-fMRI differed from multi-echo EPI-fMRI, and MELS-fMRI could not be used for non-BOLD component correction for the resting-state fMRI study(Kundu et al., 2012). This implies that the MELS-fMRI method would be less practical for human brain mapping and awake animal fMRI. However, this method could be readily used for ventilated and head-fixed animals under anesthesia. In addition, MELS-fMRI was less sensitive to the field inhomogeneity and fluctuation. It was less dependent on gradient performance and had shorter readout times than EPI-fMRI. These features allowed MELS-fMRI to acquire images with a much higher spatiotemporal resolution than EPI-fMRI to directly decipher distinct vascular contributions to the fMRI signal with different hemodynamic features. This method provided a unique advantage to characterize the vessel-specific neurovascular signaling events in the normal and diseased states, e.g. stroke or vascular/neuronal dementia, of animal models.

Acknowledgments

This research was supported by funding of the DFG SPP 1665 and internal funding from the Max Planck Society. We thank Dr. Pohmann, R., Dr. Merkle H., and Buckenmaier, K. for technical support. We thank Ms. Schulz, H. and Fischer, S. for animal maintenance support. We thank Schluesner J. and Pais-Roldán P for proofreading the manuscript. We thank the AFNI team for the software support.

Conflict of Interest: The authors declare that no competing interests exist.

Authors' contributions

XY designed the research. YH, MW performed animal experiments; YH, XY acquired and analyzed data; XY, YH wrote the paper.

REFERENCES

Bandettini, P.A., Wong, E.C., Hinks, R.S., Tikofsky, R.S., and Hyde, J.S. (1992). Time course EPI of human brain function during task activation. Magn Reson Med 25, 390-397.

Belliveau, J.W., Kennedy, D.N., Jr., McKinstry, R.C., Buchbinder, B.R., Weisskoff, R.M., Cohen, M.S., Vevea, J.M., Brady, T.J., and Rosen, B.R. (1991). Functional mapping of the human visual cortex by magnetic resonance imaging. Science 254, 716-719.

Berwick, J., Johnston, D., Jones, M., Martindale, J., Redgrave, P., McLoughlin, N., Schiessl, I., and Mayhew, J.E. (2005). Neurovascular coupling investigated with two-dimensional optical imaging spectroscopy in rat whisker barrel cortex. Eur J Neurosci 22, 1655-1666.

Blinder, P., Shih, A.Y., Rafie, C., and Kleinfeld, D. (2010). Topological basis for the robust distribution of blood to rodent neocortex. Proc Natl Acad Sci U S A 107, 12670-12675.

Blockley, N.P., Jiang, L., Gardener, A.G., Ludman, C.N., Francis, S.T., and Gowland, P.A. (2008). Field strength dependence of R1 and R2* relaxivities of human whole blood to ProHance, Vasovist, and deoxyhemoglobin. Magnetic resonance in medicine : official journal of the Society of Magnetic Resonance in Medicine / Society of Magnetic Resonance in Medicine 60, 1313-1320.

Budde, J., Shajan, G., Zaitsev, M., Scheffler, K., and Pohmann, R. (2014). Functional MRI in human subjects with gradient-echo and spin-echo EPI at 9.4 T. Magnetic resonance in medicine : official journal of the Society of Magnetic Resonance in Medicine / Society of Magnetic Resonance in Medicine 71, 209-218.

Chen, N.K., and Wyrwicz, A.M. (1999). Correction for EPI distortions using multi-echo gradient-echo imaging. Magn Reson Med 41, 1206-1213.

Cheng, K., Waggoner, R.A., and Tanaka, K. (2001). Human ocular dominance columns as revealed by high-field functional magnetic resonance imaging. Neuron 32, 359-374.

Cox, R.W. (1996). AFNI: software for analysis and visualization of functional magnetic resonance neuroimages. Computers and biomedical research, an international journal 29, 162-173.

Detre, J.A., Leigh, J.S., Williams, D.S., and Koretsky, A.P. (1992). Perfusion imaging. Magn Reson Med 23, 37-45.

Devor, A., Dunn, A.K., Andermann, M.L., Ulbert, I., Boas, D.A., and Dale, A.M. (2003). Coupling of total hemoglobin concentration, oxygenation, and neural activity in rat somatosensory cortex. Neuron 39, 353-359.

Duong, T.Q., Kim, D.S., Ugurbil, K., and Kim, S.G. (2001). Localized cerebral blood flow response at submillimeter columnar resolution. Proc Natl Acad Sci U S A 98, 10904-10909.

Duong, T.Q., Yacoub, E., Adriany, G., Hu, X., Ugurbil, K., and Kim, S.G. (2003). Microvascular BOLD contribution at 4 and 7 T in the human brain: gradient-echo and spin-echo fMRI with suppression of blood effects. Magn Reson Med 49, 1019-1027.

Duyn, J.H. (2012). The future of ultra-high field MRI and fMRI for study of the human brain. NeuroImage 62, 1241-1248.

Fukuda, M., Moon, C.H., Wang, P., and Kim, S.G. (2006). Mapping iso-orientation columns by contrast agent-enhanced functional magnetic resonance imaging: reproducibility, specificity, and evaluation by optical imaging of intrinsic signal. J Neurosci 26, 11821-11832.

Gagnon, L., Sakadzic, S., Lesage, F., Musacchia, J.J., Lefebvre, J., Fang, Q., Yucel, M.A., Evans, K.C., Mandeville, E.T., Cohen-Adad, J.*, et al.* (2015). Quantifying the microvascular origin of BOLD-fMRI from first principles with two-photon microscopy and an oxygen-sensitive nanoprobe. J Neurosci 35, 3663-3675.

Geissler, A., Gartus, A., Foki, T., Tahamtan, A.R., Beisteiner, R., and Barth, M. (2007). Contrast-to-noise ratio (CNR) as a quality parameter in fMRI. J Magn Reson Imaging 25, 1263-1270.

Goense, J., Merkle, H., and Logothetis, N.K. (2012). High-resolution fMRI reveals laminar differences in neurovascular coupling between positive and negative BOLD responses. Neuron 76, 629-639.

Goense, J.B., and Logothetis, N.K. (2006). Laminar specificity in monkey V1 using high-resolution SE-fMRI. Magn Reson Imaging 24, 381-392.

Grinvald, A., Slovin, H., and Vanzetta, I. (2000). Non-invasive visualization of cortical columns by fMRI. Nat Neurosci 3, 105-107.

Hall, C.N., Reynell, C., Gesslein, B., Hamilton, N.B., Mishra, A., Sutherland, B.A., O'Farrell, F.M., Buchan, A.M., Lauritzen, M., and Attwell, D. (2014). Capillary pericytes regulate cerebral blood flow in health and disease. Nature 508, 55-60.

Harel, N., Bolan, P.J., Turner, R., Ugurbil, K., and Yacoub, E. (2010). Recent advances in high-resolution MR application and its implications for neurovascular coupling research. Frontiers in neuroenergetics 2.

Heinzle, J., Koopmans, P.J., den Ouden, H.E., Raman, S., and Stephan, K.E. (2016). A hemodynamic model for layered BOLD signals. NeuroImage 125, 556-570.

Hillman, E.M., Devor, A., Bouchard, M.B., Dunn, A.K., Krauss, G.W., Skoch, J., Bacskai, B.J., Dale, A.M., and Boas, D.A. (2007). Depth-resolved optical imaging and microscopy of vascular compartment dynamics during somatosensory stimulation. NeuroImage 35, 89-104.

Hu, X.P., and Norris, D.G. (2004). Advances in high-field magnetic resonance imaging. Annu Rev Biomed Eng 6, 157-184.

Huber, L., Goense, J., Kennerley, A.J., Trampel, R., Guidi, M., Reimer, E., Ivanov, D., Neef, N., Gauthier, C.J., Turner, R., and Moller, H.E. (2015). Cortical lamina-dependent blood volume changes in human brain at 7 T. NeuroImage 107, 23-33.

Hyde, J.S., Biswal, B.B., and Jesmanowicz, A. (2001). High-resolution fMRI using multislice partial k-space GR-EPI with cubic voxels. Magn Reson Med 46, 114-125.

Jezzard, P., Heineman, F., Taylor, J., DesPres, D., Wen, H., Balaban, R.S., and Turner, R. (1994). Comparison of EPI gradient-echo contrast changes in cat brain caused by respiratory challenges with direct simultaneous evaluation of cerebral oxygenation via a cranial window. NMR Biomed 7, 35-44.

Jochimsen, T.H., Norris, D.G., Mildner, T., and Moller, H.E. (2004). Quantifying the intra- and extravascular contributions to spin-echo fMRI at 3 T. Magn Reson Med 52, 724-732.

Keller, A.L., Schuz, A., Logothetis, N.K., and Weber, B. (2011). Vascularization of cytochrome oxidase-rich blobs in the primary visual cortex of squirrel and macaque monkeys. J Neurosci 31, 1246-1253.

Kennerley, A.J., Berwick, J., Martindale, J., Johnston, D., Papadakis, N., and Mayhew, J.E. (2005). Concurrent fMRI and optical measures for the investigation of the hemodynamic response function. Magn Reson Med 54, 354-365.

Kim, D.S., Duong, T.Q., and Kim, S.G. (2000). High-resolution mapping of iso-orientation columns by fMRI. Nat Neurosci 3, 164-169.

Kim, S.G., Hendrich, K., Hu, X., Merkle, H., and Ugurbil, K. (1994). Potential pitfalls of functional MRI using conventional gradient-recalled echo techniques. NMR in biomedicine 7, 69-74.

Kim, S.G., and Ugurbil, K. (2003). High-resolution functional magnetic resonance imaging of the animal brain. Methods 30, 28-41.

Kim, T., Hendrich, K.S., Masamoto, K., and Kim, S.G. (2007a). Arterial versus total blood volume changes during neural activity-induced cerebral blood flow change: implication for BOLD fMRI. J Cereb Blood Flow Metab 27, 1235-1247.

Kim, T., Hendrich, K.S., Masamoto, K., and Kim, S.G. (2007b). Arterial versus total blood volume changes during neural activity-induced cerebral blood flow change: implication for BOLD fMRI. J Cerebr Blood F Met 27, 1235-1247.

Kim, T., and Kim, S.G. (2011). Temporal dynamics and spatial specificity of arterial and venous blood volume changes during visual stimulation: implication for BOLD quantification. Journal of cerebral blood flow and metabolism : official journal of the International Society of Cerebral Blood Flow and Metabolism 31, 1211-1222.

Kundu, P., Brenowitz, N.D., Voon, V., Worbe, Y., Vertes, P.E., Inati, S.J., Saad, Z.S., Bandettini, P.A., and Bullmore, E.T. (2013). Integrated strategy for improving functional connectivity mapping using multiecho fMRI. Proc Natl Acad Sci U S A 110, 16187-16192.

Kundu, P., Inati, S.J., Evans, J.W., Luh, W.M., and Bandettini, P.A. (2012). Differentiating BOLD and non-BOLD signals in fMRI time series using multi-echo EPI. NeuroImage 60, 1759-1770.

Kwong, K.K., Belliveau, J.W., Chesler, D.A., Goldberg, I.E., Weisskoff, R.M., Poncelet, B.P., Kennedy, D.N., Hoppel, B.E., Cohen, M.S., Turner, R., and et al. (1992). Dynamic magnetic resonance imaging of human brain activity during primary sensory stimulation. Proc Natl Acad Sci U S A 89, 5675-5679.

Lee, S.P., Duong, T.Q., Yang, G., Iadecola, C., and Kim, S.G. (2001). Relative changes of cerebral arterial and venous blood volumes during increased cerebral blood flow: implications for BOLD fMRI. Magn Reson Med 45, 791-800.

Lee, S.P., Silva, A.C., Ugurbil, K., and Kim, S.G. (1999). Diffusion-weighted spin-echo fMRI at 9.4 T: microvascular/tissue contribution to BOLD signal changes. Magnetic resonance in medicine : official journal of the Society of Magnetic Resonance in Medicine / Society of Magnetic Resonance in Medicine 42, 919-928.

Lin, F.H., Witzel, T., Raij, T., Ahveninen, J., Tsai, K.W., Chu, Y.H., Chang, W.T., Nummenmaa, A., Polimeni, J.R., Kuo, W.J., *et al.* (2013). fMRI hemodynamics accurately reflects neuronal timing in the human brain measured by MEG. NeuroImage 78, 372-384.

Lu, H., Golay, X., Pekar, J.J., and Van Zijl, P.C. (2003). Functional magnetic resonance imaging based on changes in vascular space occupancy. Magn Reson Med 50, 263-274.

Madsen, M.T. (1992). A simplified formulation of the gamma variate function. Physics in Medicine and Biology 37, 1597.

Malonek, D., and Grinvald, A. (1996). Interactions between electrical activity and cortical microcirculation revealed by imaging spectroscopy: implications for functional brain mapping. Science 272, 551-554.

Mansfield, P., Maudsley, A.A., and Baines, T. (1976). Fast Scan Proton Density Imaging by Nmr. J Phys E Sci Instrum 9, 271-278.

Menon, R.S., Ogawa, S., Strupp, J.P., and Ugurbil, K. (1997). Ocular dominance in human V1 demonstrated by functional magnetic resonance imaging. J Neurophysiol 77, 2780-2787.

Menon, R.S., Ogawa, S., Tank, D.W., and Ugurbil, K. (1993). Tesla gradient recalled echo characteristics of photic stimulation-induced signal changes in the human primary visual cortex. Magnetic resonance in medicine : official journal of the Society of Magnetic Resonance in Medicine / Society of Magnetic Resonance in Medicine 30, 380-386.

Moon, C.H., Fukuda, M., and Kim, S.G. (2013). Spatiotemporal characteristics and vascular sources of neural-specific and -nonspecific fMRI signals at submillimeter columnar resolution. NeuroImage 64, 91-103.

Ogawa, S., Lee, T.M., Kay, A.R., and Tank, D.W. (1990). Brain magnetic resonance imaging with contrast dependent on blood oxygenation. Proc Natl Acad Sci U S A 87, 9868-9872.

Ogawa, S., Tank, D.W., Menon, R., Ellermann, J.M., Kim, S.G., Merkle, H., and Ugurbil, K. (1992). Intrinsic signal changes accompanying sensory stimulation: functional brain mapping with magnetic resonance imaging. Proc Natl Acad Sci U S A 89, 5951-5955.

Polimeni, J.R., Fischl, B., Greve, D.N., and Wald, L.L. (2010). Laminar analysis of 7T BOLD using an imposed spatial activation pattern in human V1. NeuroImage 52, 1334-1346.

Poser, B.A., and Norris, D.G. (2009). Investigating the benefits of multi-echo EPI for fMRI at 7 T. NeuroImage 45, 1162-1172.

Poser, B.A., Versluis, M.J., Hoogduin, J.M., and Norris, D.G. (2006). BOLD contrast sensitivity enhancement and artifact reduction with multiecho EPI: parallel-acquired inhomogeneity-desensitized fMRI. Magn Reson Med 55, 1227-1235.

Shih, Y.Y., Chen, Y.Y., Lai, H.Y., Kao, Y.C., Shyu, B.C., and Duong, T.Q. (2013). Ultra high-resolution fMRI and electrophysiology of the rat primary somatosensory cortex. NeuroImage 73, 113-120.

Siero, J.C., Petridou, N., Hoogduin, H., Luijten, P.R., and Ramsey, N.F. (2011). Cortical depth-dependent temporal dynamics of the BOLD response in the human brain. J Cereb Blood Flow Metab 31, 1999-2008.

Silva, A.C., and Koretsky, A.P. (2002). Laminar specificity of functional MRI onset times during somatosensory stimulation in rat. Proceedings of the National Academy of Sciences of the United States of America 99, 15182-15187.

Silva, A.C., Koretsky, A.P., and Duyn, J.H. (2007). Functional MRI impulse response for BOLD and CBV contrast in rat somatosensory cortex. Magnetic resonance in medicine : official journal of the Society of Magnetic Resonance in Medicine / Society of Magnetic Resonance in Medicine 57, 1110-1118.

Spees, W.M., Yablonskiy, D.A., Oswood, M.C., and Ackerman, J.J. (2001). Water proton MR properties of human blood at 1.5 Tesla: magnetic susceptibility, T(1), T(2), T*(2), and non-Lorentzian signal behavior. Magn Reson Med 45, 533-542.

Tian, P., Teng, I.C., May, L.D., Kurz, R., Lu, K., Scadeng, M., Hillman, E.M., De Crespigny, A.J., D'Arceuil, H.E., Mandeville, J.B., *et al.* (2010). Cortical depth-specific microvascular dilation underlies laminar differences in blood oxygenation level-dependent functional MRI signal. Proc Natl Acad Sci U S A 107, 15246-15251.

Ugurbil, K., Toth, L., and Kim, D.S. (2003). How accurate is magnetic resonance imaging of brain function? Trends Neurosci 26, 108-114.

Uhlirova, H., Kilic, K., Tian, P., Thunemann, M., Desjardins, M., Saisan, P.A., Sakadzic, S., Ness, T.V., Mateo, C., Cheng, Q., *et al.* (2016). Cell type specificity of neurovascular coupling in cerebral cortex. Elife 5.

Uludag, K., Muller-Bierl, B., and Ugurbil, K. (2009). An integrative model for neuronal activity-induced signal changes for gradient and spin echo functional imaging. NeuroImage 48, 150-165.

Vazquez, A.L., Fukuda, M., Tasker, M.L., Masamoto, K., and Kim, S.G. (2010a). Changes in cerebral arterial, tissue and venous oxygenation with evoked neural stimulation: implications for hemoglobin-based functional neuroimaging. J Cereb Blood Flow Metab 30, 428-439.

Vazquez, A.L., Fukuda, M., Tasker, M.L., Masamoto, K., and Kim, S.G. (2010b). Changes in cerebral arterial, tissue and venous oxygenation with evoked neural stimulation: implications for hemoglobin-based functional neuroimaging. Journal of cerebral blood flow and metabolism : official journal of the International Society of Cerebral Blood Flow and Metabolism 30, 428-439.

Weiskopf, N., Klose, U., Birbaumer, N., and Mathiak, K. (2005). Single-shot compensation of image distortions and BOLD contrast optimization using multi-echo EPI for real-time fMRI. NeuroImage 24, 1068-1079.

Yacoub, E., Duong, T.Q., Van De Moortele, P.F., Lindquist, M., Adriany, G., Kim, S.G., Ugurbil, K., and Hu, X. (2003). Spin-echo fMRI in humans using high spatial resolutions and high magnetic fields. Magn Reson Med 49, 655-664.

Yacoub, E., Harel, N., and Ugurbil, K. (2008). High-field fMRI unveils orientation columns in humans. Proceedings of the National Academy of Sciences of the United States of America 105, 10607-10612.

Yacoub, E., Shmuel, A., Pfeuffer, J., Van De Moortele, P.F., Adriany, G., Andersen, P., Vaughan, J.T., Merkle, H., Ugurbil, K., and Hu, X. (2001). Imaging brain function in humans at 7 Tesla. Magn Reson Med 45, 588-594.

Yu, X., Glen, D., Wang, S., Dodd, S., Hirano, Y., Saad, Z., Reynolds, R., Silva, A.C., and Koretsky, A.P. (2012). Direct imaging of macrovascular and microvascular contributions to BOLD fMRI in layers IV-V of the rat whisker-barrel cortex. NeuroImage 59, 1451-1460.

Yu, X., He, Y., Wang, M., Merkle, H., Dodd, S.J., Silva, A.C., and Koretsky, A.P. (2016). Sensory and optogenetically driven single-vessel fMRI. Nature methods 13, 337-340.

Yu, X., Qian, C., Chen, D.Y., Dodd, S.J., and Koretsky, A.P. (2014). Deciphering laminar-specific neural inputs with line-scanning fMRI. Nature methods 11, 55-58.

Yu, X., Wang, S.M., Chen, D.Y., Dodd, S., Goloshevsky, A., and Koretsky, A.P. (2010). 3D mapping of somatotopic reorganization with small animal functional MRI. NeuroImage 49, 1667-1676.

Main Figures (4)

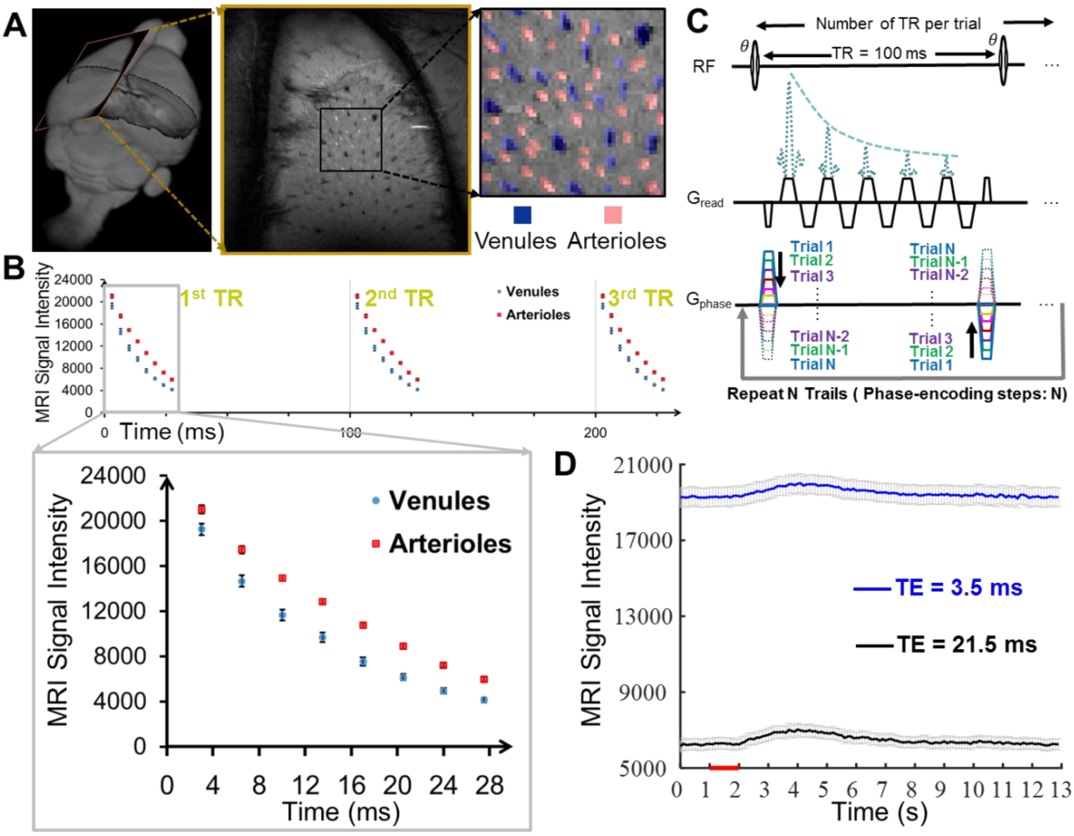

Figure 1. Map the single-vessel fMRI signal with the MELS-fMRI method. (**A**) The 2D slice position of the A-V map is shown in the 3D rat brain (left panel). The arteriole voxels were marked in red ROIs and the venule voxels were marked as blue ROIs (right panel). (**B**). The signal intensity of venule voxels (blue circles) and arteriole voxels (red squares) is shown at different echo time from three consecutive TR (100ms). The enlarged data showed that the venule voxels has faster decay curve than the arteriole voxels (one representative rat from five rats, venules: n = 25, arteriole: n = 35, mean ± s.e.m) **(C)**. MELS-fMRI pulse sequence diagram. Only one phase-encoding step was employed at each trial. The trials were repeated for the number of phase-encoding steps to fill up the k-space. (**D**). The signal intensity of long TE (21.5 ms) and short TE (3.5 ms) from venule voxels (n = 25, mean ± s.e.m) as the function of the on/off block design time (1s off, 2s on, and 10 s off).

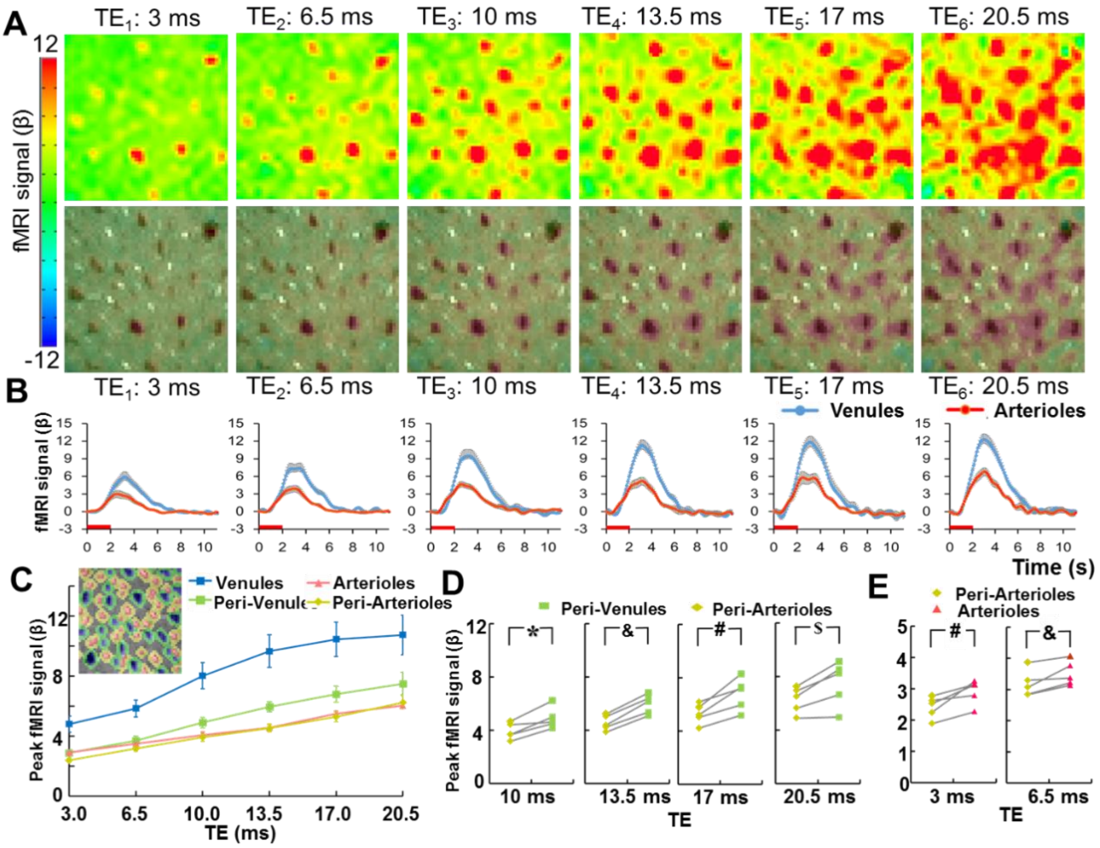

Figure 2. The vessel-specific fMRI patterns acquired at different TEs. (**A**) The color-coded fMRI maps are shown at six different TEs (up) and the overlapped images with the A-V map represent the venule-dominated peak fMRI signal distribution (bottom). (**B**) The averaged time courses of fMRI signal from venule (blue) and arteriole (red) voxels (n = 5 rats, the graphs show the mean ± s.e.m). (**C**) The peak amplitudes of fMRI signal from arteriole (red), venule (blue), peri-venule (green), and peri-arteriole (yellow) voxels are shown at different TEs (n = 5 rats, mean ± s.e.m). The inset is an A-V map demo to show the definition of different ROIs. (**D**) The peak fMRI signal of peri-venule voxels are significantly higher than that of the peri-arteriole voxels acquired at TEs ranging from 10ms to 20.5ms (n=5, *, p = 0.007, &, p = 0.0001, #, p = 0.005, $, p = 0.012, paired t-test). (**E**) The peak fMRI signal of arteriole voxels are significantly higher than that of the peri-arteriole voxels acquired at TEs 3 ms and 6.5ms (#, p = 0.012; &, p = 0.017, paired t-test, n = 5).

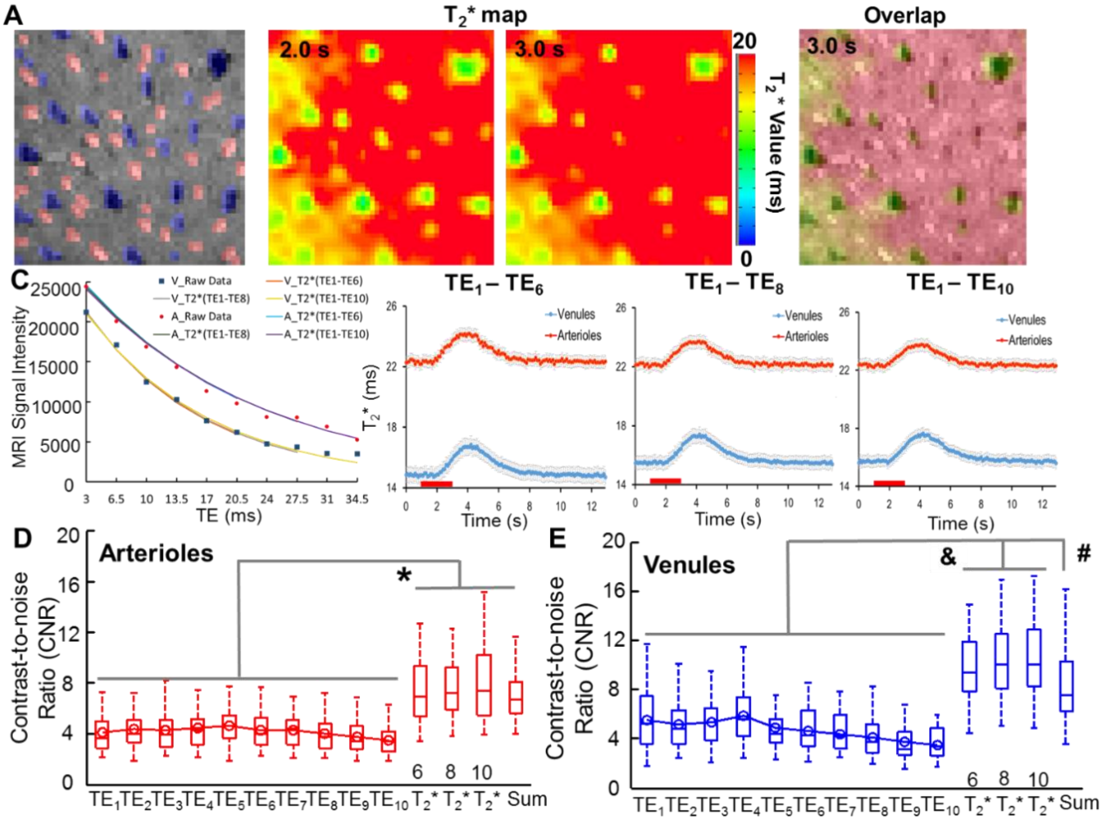

Fiugre 3. The vessel-specific T_2* map with the MELS-fMRI method. (A) A-V map **(B)** The T_2* maps of the 2D slice acquired at 2s and 3s after stimulus onset (left and middle panel). The T_2* map (3s) is overlapped with the A-V map, showing all venules voxels have shorter T_2* decay time than the surrounding parenchyma and arteriole voxels (right). **(C)** The decay curves were fitted to the MR signal detected at different TEs of one venule voxel and one arterial voxel. The averaged time course of T_2*-value (TE1-TE6, TE1-TE8, TE1-TE10) based fMRI signal from most activated venules (blue) and arterioles ROIs (n = 48 arterioles, red, 36 venules, blue, mean ± s.e.m.). **(D-E)** The Contrast-to-noise Ratios (CNR) of T_2*-weight fMRI signal acquired at different TEs are significantly lower than the CNR of the T_2*-based fMRI signal from arteriole and venule voxels (*, F=36.81, p<0.00001, &, F=33.03, p<0.00001, one-way ANOVA followed by Tukey's multiple comparison test).

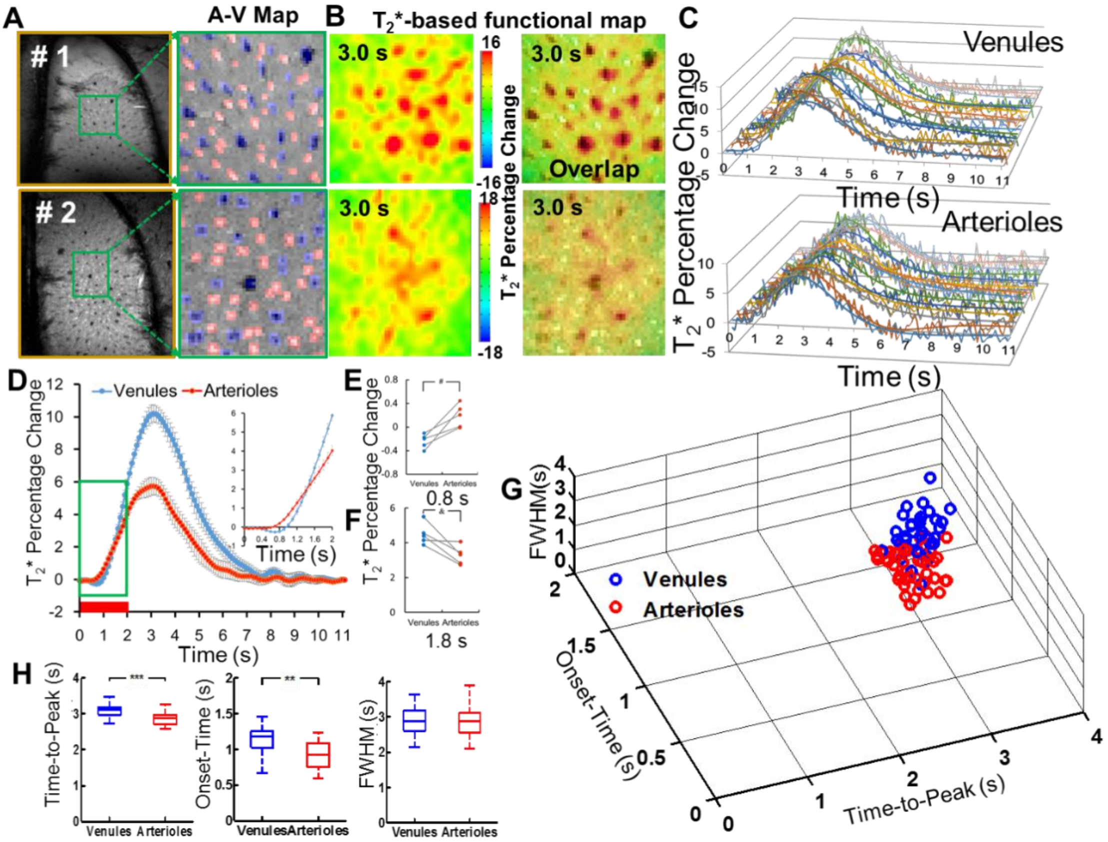

Figure 4. The hemodynamic feature of the T_2*-based fMRI signal with the MELS-fMRI method. (**A**) The A-V maps from two representative rats of five rats show arteriole (red) and venule (blue) ROIs. (**B**) T_2*-based fMRI maps at 3.0s after stimulation and the overlap images with A-V maps. (**C**) The time course (raw data and fitting curves) of T_2*-based fMRI signal from individual venule voxels (upper panel) and individual arteriole voxels (lower panel) of one representative rat. (**D**) The averaged time course of T_2* fMRI signal from venule (blue) and arteriole (red) voxels (n = 5 rats, mean ± s.e.m). The inset is the enlarged time course from 0 s to 2.0 s after stimulus onset. (**E-F**) T_2* fMRI signal percentage changes from arteriole and venule ROIs are shown at 0.8 s and 1.8 s after stimulation onset from individual rats (#, p = 0.006; &, p = 0.012, paired t-test, n = 5). (**G**) The 3d plot of Onset-time (T0), Time-to-Peak (TTP), and the full-width-of-half-maximum (FWHM) of T_2* fMRI signal from individual arteriole (red circles, 34, $r^2 > 0.8$) and venule (blue circles, 43, $r^2 > 0.7$) voxels demonstrates two distinct clusters. (**H**). The boxplot of TTP, T0 from venule voxels (blue) is significantly higher than that from arteriole voxels (red) (*, p = 6.2×10^{-8}, &, p = 8.1×10^{-9}, unpaired t-test, arteriole voxels, 34, venule voxels, 43). The boxplot shows no significant difference on FWHM of the venule and arteriole voxels (right panel).

Supplementary Figures (5)

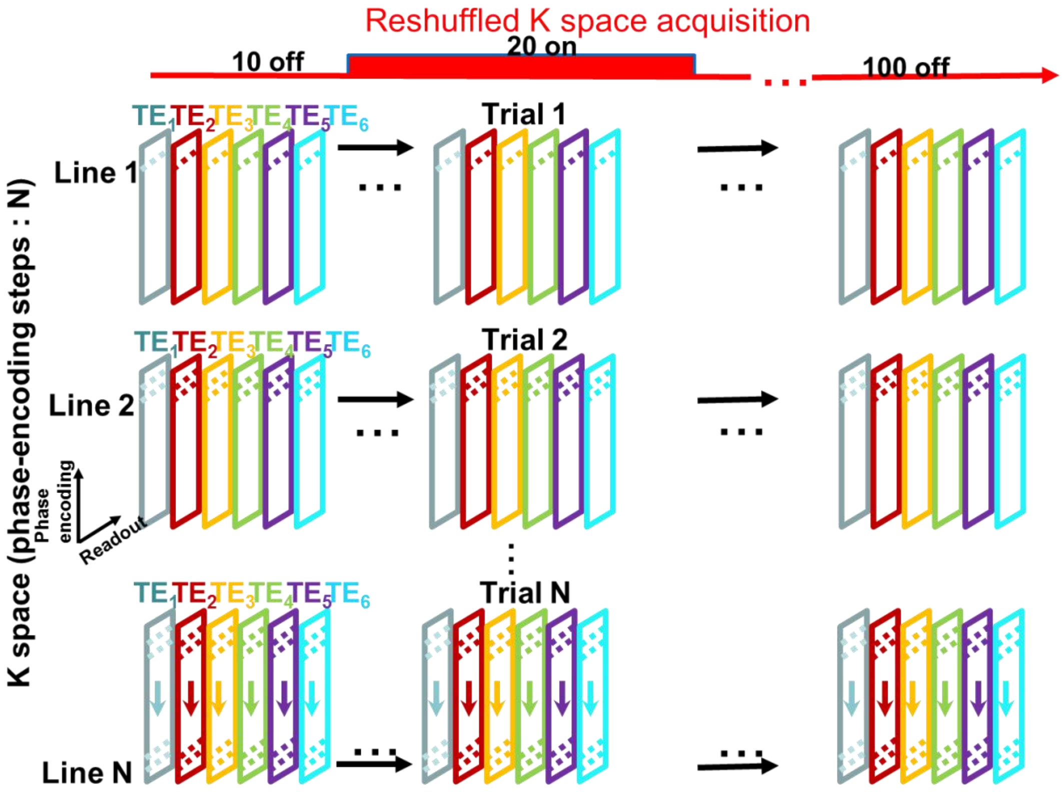

Supplementary Figure 1. K-space Trajectory of Multi-Echo Line-Scanning fMRI (MELS-fMRI). The k-space of MELS-fMRI is shown in a block-design paradigm with 10 scans off, 20 scans on and 100 scans off (the red line). Each box in different colors represents the k-space of the same slice acquired at different TEs. Within the box, each line indicated a k-space line. One line filled the k-space for each image at each trial consequentially. Then the trials were repeated for the number of phase-encoding steps.

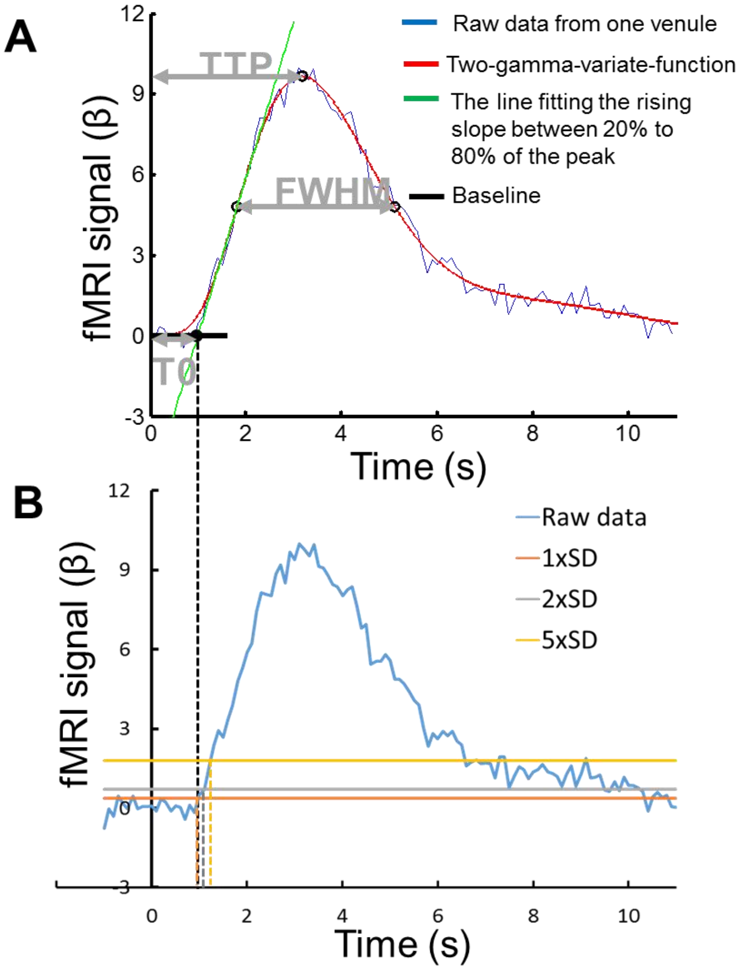

Supplementary Figure 2. The Definition of T0, TTP, FWHM. (A). The raw fMRI signal (blue line) was fitted with the two-gamma-variate function (red line). The green line was fit to the rising slope of fMRI signal between 20% and 80% to the peak amplitude of two-gamma-variate-function. The T0 was estimated as the intercept with the x-axis. The TTP was estimated by the time from the stimulus onset to the peak amplitude of the two-gamma-variate-function. The FWHM was estimated by the time between two points that are the half of the maximum amplitude of the two-gamma-variate-function. **(B).** the first (second, fifth) standard deviation (SD) from baseline show that the onset time defined here is between the first SD and the second SD from baseline.

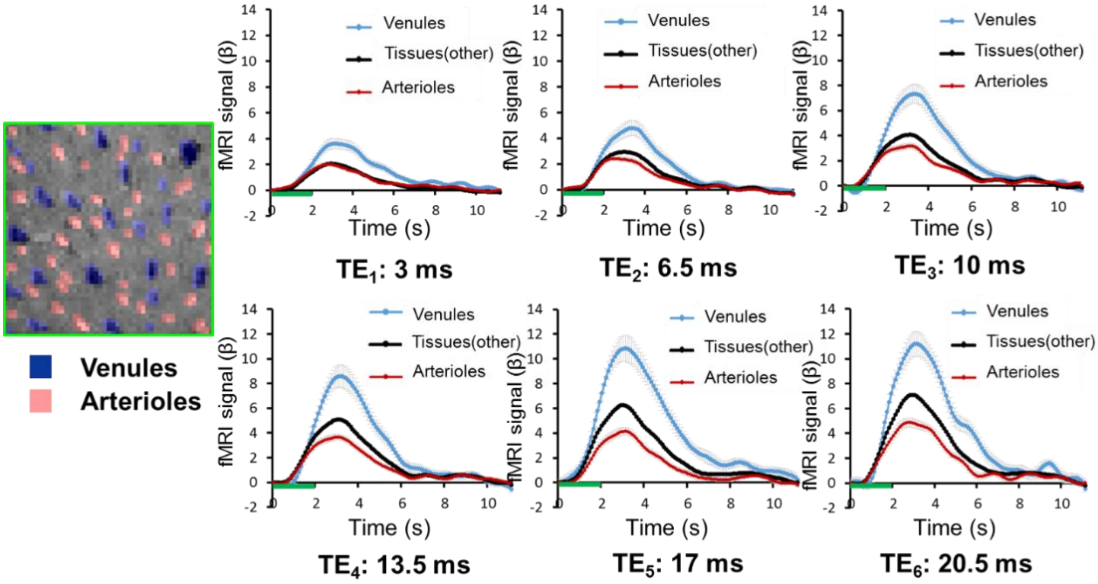

Supplementary Figure 3. The averaged time courses of fMRI signal from venule (blue), arteriole (red) and other non-vessel voxels (black) from one representative rat.

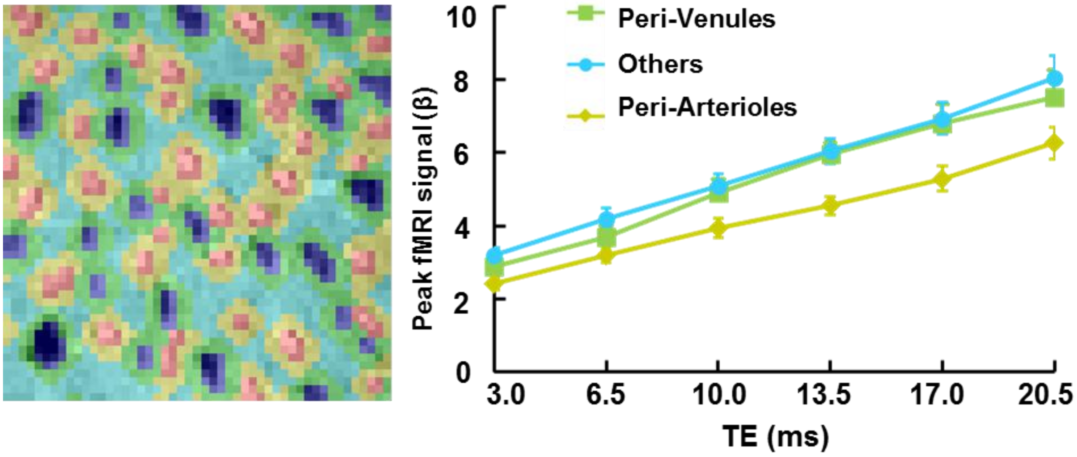

Supplementary Figure 4. The peak amplitudes of fMRI signal from peri-venule (green), peri-arteriole (yellow), and others (cyan) voxels are shown at different TEs (n = 5 rats, mean ± s.e.m). The left panel is an A-V map demo to show the definition of different ROIs.

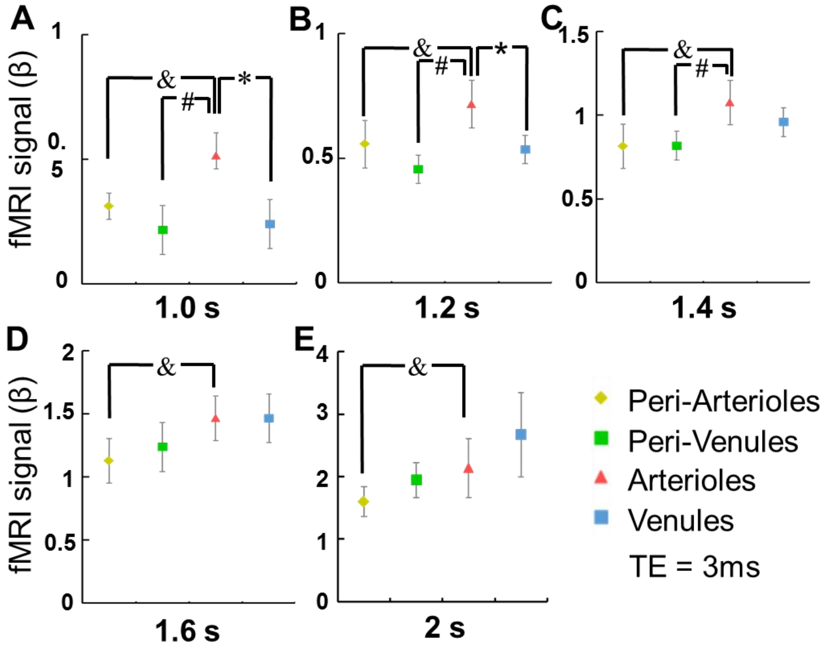

Supplementary Figure 5. Vessel-specific fMRI signal at different time (TE = 3 ms). The amplitudes (1.0s , 1.2s, 1.4s, 1.6s, 2s after the stimulation onset) of the fMRI signal from arteriole (red), venule (blue), peri-venule (green), and peri-arteriole (yellow) voxels were shown at 3 ms TE (n = 5 rats, mean ± s.e.m). **(A)** The fMRI signal of arteriole voxels was significantly higher than that of the venule, peri-venule, and peri-arteriole voxels at 1.0s after the stimulation onset. (Paired t-test, n = 5, *, p = 0.009, &, p = 0.04, #, p = 0.037). **(B)**. The fMRI signal of arteriole voxels was significantly higher than that of the venule, peri-venule, peri-arteriole voxels at 1.2 s after the stimulation onset. (Paired t-test, n = 5, *, p = 0.025, &, p = 0.047, #, p = 0.034) **(C)**. The fMRI signal of arteriole voxels was significantly higher than that of peri-venule and peri-arteriole voxels at 1.4 s after the stimulation onset. (Paired t-test, n = 5, &, p = 0.034, #, p = 0.049) **(D)**. The fMRI signal of arteriole voxels was significantly higher than that of peri-arteriole voxels at 1.6 s after the stimulation onset. (Paired t-test, n = 5, &, p = 0.049) **(E)**. The fMRI signal of venule voxels was significantly higher than that of arteriole voxels at 2.0 s after the stimulation onset. (Paired t-test, n = 5, &, p = 0.042)

Supplementary Movie Legends

Supplementary Movie 1. The three-dimensional plot of the mean signal intensity of multiple TEs from venule voxels as a function of time (block design: 1s off, 2s on, and 10s off).

Supplementary Movie 2. The spatial patterns of vessel-specific fMRI signal at different TEs. The voxel-wise BOLD fMRI signal was demonstrated from 7x7 voxel matrix covering one individual venule (middle panel: the dark voxel in the green square, in-plane resolution: 50 x 50 μm). The red curser in the center voxel (100 ms temporal resolution) indicated the fMRI signal changes at 6.5 ms TE (right panel).

Supplementary Movie 3. The T_2*-based fMRI maps from two representative rats. T_2*-based fMRI maps (middle panel) were overlapped with the A-V map (left panel). The most active voxels (red color, 100x100 μm) were primarily located at the underlying venule voxels (black dots, right panel).

4.3 A.3 Ultra-slow single vessel BOLD and CBV-based fMRI spatiotemporal dynamics and their correlation with neuronal intracellular calcium signals

Ultra-slow single vessel BOLD and CBV-based fMRI spatiotemporal dynamics and their correlation with neuronal intracellular calcium signals

He, Y., Wang, M., Chen, X., Pohmann, R., Polimeni, J., Scheffler, K., Rosen, B., Kleinfeld, D. and Yu, X.

Neuron, 2018, 97 (4), 925-939. e5

Neuron

Article

Ultra-Slow Single-Vessel BOLD and CBV-Based fMRI Spatiotemporal Dynamics and Their Correlation with Neuronal Intracellular Calcium Signals

Graphical Abstract

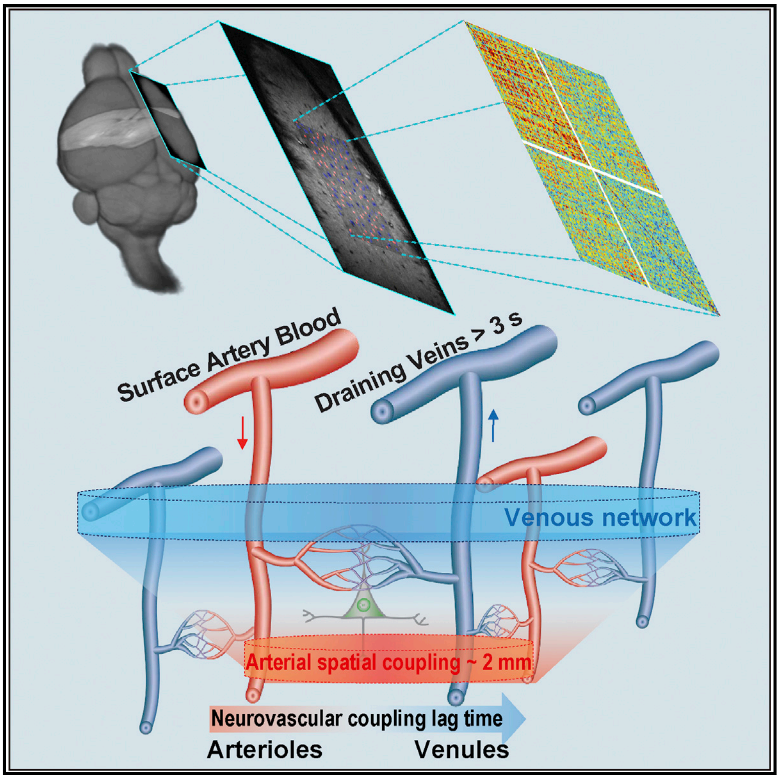

Highlights

- bSSFP-based single-vessel fMRI reveals dynamic vascular network connectivity
- Arterioles and venules showed distinct patterns of spatiotemporal correlations
- Neural Ca^{2+} ultra-slow oscillations correlate to vessel-specific fMRI fluctuations
- Human brain fMRI signal fluctuations were mapped in individual gray matter veins

Authors

Yi He, Maosen Wang, Xuming Chen, ...,
Bruce R. Rosen, David Kleinfeld, Xin Yu

Correspondence

xin.yu@tuebingen.mpg.de

In Brief

He et al. performed single-vessel fMRI in rat to map spatiotemporal correlations of ultra-slow arteriole CBV and venule BOLD fluctuations, concurrent with intracellular-calcium photometry. They find a 2 mm correlation length, which bears on the resolution of functional connectivity.

He et al., 2018, Neuron *97*, 1–15
February 21, 2018 © 2018 Elsevier Inc.
https://doi.org/10.1016/j.neuron.2018.01.025

CellPress

Please cite this article in press as: He et al., Ultra-Slow Single-Vessel BOLD and CBV-Based fMRI Spatiotemporal Dynamics and Their Correlation with Neuronal Intracellular Calcium Signals, Neuron (2018), https://doi.org/10.1016/j.neuron.2018.01.025

Neuron
Article

Ultra-Slow Single-Vessel BOLD and CBV-Based fMRI Spatiotemporal Dynamics and Their Correlation with Neuronal Intracellular Calcium Signals

Yi He,[1,2] Maosen Wang,[1,2] Xuming Chen,[1,2] Rolf Pohmann,[1] Jonathan R. Polimeni,[3] Klaus Scheffler,[1,6] Bruce R. Rosen,[3] David Kleinfeld,[4,5] and Xin Yu[1,7,*]
[1]High-Field Magnetic Resonance Department, Max Planck Institute for Biological Cybernetics, 72076 Tuebingen, Germany
[2]Graduate Training Centre of Neuroscience, International Max Planck Research School, University of Tuebingen, 72074 Tuebingen, Germany
[3]MGH/MIT/HMS Athinoula A. Martinos Center for Biomedical Imaging, Department of Radiology, Harvard Medical School, Massachusetts General Hospital, Charlestown, MA 02114, USA
[4]Department of Physics
[5]Section of Neurobiology
University of California at San Diego, La Jolla, CA 92093, USA
[6]Department of Biomedical Magnetic Resonance, University of Tübingen, 72076 Tübingen, Germany
[7]Lead Contact
*Correspondence: xin.yu@tuebingen.mpg.de
https://doi.org/10.1016/j.neuron.2018.01.025

SUMMARY

Functional MRI has been used to map brain activity and functional connectivity based on the strength and temporal coherence of neurovascular-coupled hemodynamic signals. Here, single-vessel fMRI reveals vessel-specific correlation patterns in both rodents and humans. In anesthetized rats, fluctuations in the vessel-specific fMRI signal are correlated with the intracellular calcium signal measured in neighboring neurons. Further, the blood-oxygen-level-dependent (BOLD) signal from individual venules and the cerebral-blood-volume signal from individual arterioles show correlations at ultra-slow (<0.1 Hz), anesthetic-modulated rhythms. These data support a model that links neuronal activity to intrinsic oscillations in the cerebral vasculature, with a spatial correlation length of ~2 mm for arterioles. In complementary data from awake human subjects, the BOLD signal is spatially correlated among sulcus veins and specified intracortical veins of the visual cortex at similar ultra-slow rhythms. These data support the use of fMRI to resolve functional connectivity at the level of single vessels.

INTRODUCTION

The cerebral vasculature is an interconnected network that supplies metabolites to the brain and mediates chemical signaling between the brain and the body. Cerebral circulation is mediated by an electrogenic vascular system, composed of interconnected endothelial cells that transmit signals between neighboring vessels to control the tone of arteriole smooth muscle (Aydin et al., 1991; Longden et al., 2017) in addition to forming the lumen of the vessels. The vascular system exhibits a number of rhythms of neurological and vascular origin (Obrig et al., 2000; Tak et al., 2015; Zhu et al., 2015). Respiratory- and cardiac-based rhythmic components can be regressed out of the fMRI data. Yet an ultra-low frequency (0.1 Hz) fluctuation in the diameter of arterioles, known as vasomotion (Intaglietta, 1990), remain. Far from a confounding factor (Murphy et al., 2013), these fluctuations form the basis of resting-state fMRI (Biswal et al., 1995; Fox and Raichle, 2007). Critically, vasomotion has been shown to be entrained by similarly ultra-slow oscillations in neuronal signaling (Mateo et al., 2017). It has been hypothesized that these covaried vasomotion and oscillatory neuronal patterns may contribute to the physiological basis of the resting-state fMRI connectivity mapping. This would provide the underpinning to observations of concurrent ultra-slow neuronal and hemodynamic signals, acquired optically (Schulz et al., 2012; Du et al., 2014; Ma et al., 2016) and electrophysiologically (Shmuel and Leopold, 2008; Schölvinck et al., 2010).

It is an open challenge to merge the optically acquired neuronal and vessel-specific hemodynamic signaling events with fMRI recordings to directly interpret the vascular basis of the resting-state fMRI signal (Logothetis et al., 2001). In most past work, the resting-state fMRI signal is acquired from large brain voxels (He et al., 2008; Shmuel and Leopold, 2008; Schölvinck et al., 2010). However, more recently high-resolution fMRI has allowed us to map vessel-specific hemodynamic signal from distinct vessel-dominated versus parenchyma-dominated voxels enriched with capillaries in animal brains with either cerebral blood volume (CBV) fMRI or blood-oxygen-level-dependent BOLD (fMRI) (Yu et al., 2012; Moon et al., 2013; Poplawsky et al., 2017). Using line-scanning fMRI methods, the iron oxide particle-based CBV-weighted signal is localized at penetrating arterioles (Yu et al., 2016), while the BOLD signal is detected at penetrating venules (Mansfield et al., 1976; Silva and Koretsky, 2002; Yu et al., 2012, 2014). Thus, the high-resolution fMRI will

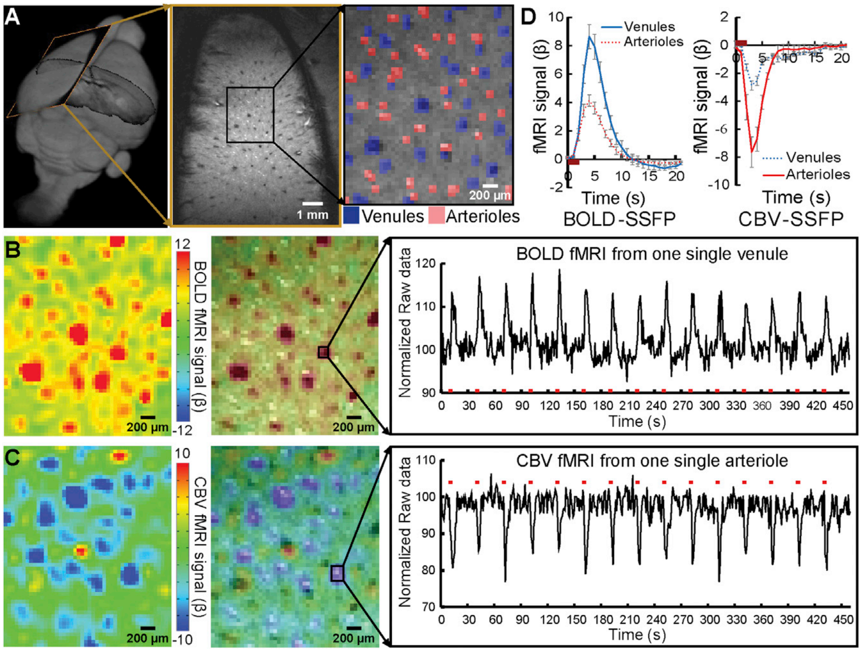

Figure 1. Balanced Steady-State Free Precession-Based Task-Related Single-Vessel BOLD and CBV fMRI

(A) An A-V map shows individual venules (dark dots, blue markers) and arterioles (bright dots, red markers) in a 2D slice.

(B) The BOLD fMRI map (left) and the semi-transparent map overlaid on the A-V map demonstrate the venule-dominated peak BOLD signal with the on/off block time series from a single venule ROI.

(C) The CBV fMRI map (left) and the semi-transparent map overlaid on the A-V map show the arteriole-dominated peak CBV signal with the on/off block time series from a single arteriole ROI.

(D) The averaged BOLD (left)/CBV (right) fMRI response function from venule (blue) and arteriole (red) voxels (n = 5, mean ± SEM).

See also Figures S1 and S4 and Table S1.

permit us to follow neurovascular-coupled hemodynamic signals as they propagate from the arteriolar network, e.g., in terms of a CBV-weighted signal that will be sensitive to changes in vascular diameter, to the venous network, e.g., in terms of the BOLD signal, to gain a vascular-specific view of hemodynamic signaling with fMRI.

The technical goal of this work is 2-fold. The first is to detect the vessel-specific fluctuations in fMRI signals during the resting state. This goal must be accomplished across a plane through cortex with sufficient speed to accurately determine the magnitude and phase of correlation mediated by vasomotor fluctuations across vessels. The second is to measure these fluctuations concurrent with calcium signal recordings from neighboring neurons. Our approach builds on our ability to identify brain arterioles from venules with MRI and our line-scanning method to map the single-vessel hemodynamic signal (Yu et al., 2016). The line-scanning scheme reshuffled the k-space acquisition so that each image was reconstructed from data acquired along the entire experimental time series with a fast sampling rate, but not in real time (Silva and Koretsky, 2002; Yu et al., 2016). Here, we develop a single-vessel resting-state fMRI mapping method to specify the unique temporal dynamic features of neurovascular oscillatory signals, as well as to characterize the spatial distribution of fluctuations in the fMRI signal in both arteriolar and venous networks. We ask: (1) can the balanced steady-state free precession (bSSFP) method be used to detect vessel-specific fMRI signal fluctuations during resting state? The bSSFP method has higher SNR per time unit than the line-scanning method and presents less image distortion with reduced extravascular effect than the echo-planar imaging (EPI) method for high-field rat brain fMRI (Scheffler and Lehnhardt, 2003). (2) Can both BOLD and CBV signals be detected at the scale of penetrating vessels, the finest spatial scale within the brain in real time? This has not been feasible for the previously established line-scanning single-vessel fMRI method (Yu et al., 2016). (3) As a means to connect neural activity with hemodynamics, does the neuronal calcium signal at the location of cortical vessels studied with fMRI match all or part of the fMRI signal with the context of low-frequency fluctuations in brain state (Schulz et al., 2012; Du et al., 2014; Ma et al., 2016)? (4) Lastly, can the single-vessel fMRI scheme be extended to map the vessel-specific long-range correlation patterns in the gray matter of the human brain?

RESULTS

Single-Vessel Mapping of the Evoked BOLD and CBV-Weighted Signal with bSSFP-fMRI

Balanced steady-state free precession (bSSFP) single-vessel fMRI was implemented to map the evoked BOLD and CBV-weighted fMRI signal in the forepaw region of primary sensory (S1) cortex rats under α-chloralose anesthesia. Although anesthesia will alter brain rhythms, and lower the ultra-slow fluctuations to below their awake, resting-state value of $\sim$0.1 Hz (Chan et al., 2015), the use of anesthesia is currently necessary for stability in these initial single-vessel fMRI measurements. Our stimulus was transient electrical stimulation of the forepaw. To acquire a high spatial resolution 2D bSSFP image, we acquired each spin echo every 7.8 ms to shorten the total acquisition time for each 2D image, comprising a 96 × 128 matrix (FOV, 9.6 × 12.8 mm) for an in-plane resolution of 100 × 100 μm, to a TR of 1 s. As described previously (Yu et al., 2016), a multi-gradient-echo (MGE) sequence was used to distinguish among individual arterioles (bright dots, due to the inflow effect) and venules (dark dots, due to fast T2* decay of deoxygenated blood) from the anatomical single-vessel 2D images, i.e., the arteriole-venule (A-V) map (Figure 1A). Also noteworthy is that the A-V ratio is 0.85 ± 0.04 (Table S1), demonstrating more penetrating veins than arteries, which is consistent with what has been previous reported in rodents (Hirsch et al., 2012; Blinder et al., 2013).

Further, the sensory-evoked single-vessel BOLD and CBV-weighted fMRI signal was detected by the bSSFP single-vessel fMRI before and after iron oxide particle injection. The data of Figure 1B show that the peak BOLD signals are primarily located at the venule voxels with the time course of the positive BOLD signal from a selected venule (Figure S1). After an injection of iron oxide particles, the bSSFP fMRI signal was acquired in the same 2D slice and shows that the evoked CBV-weighted signal corresponds to a decreased T2*-weighted MR signal (Figure 1C). Note that the T2*-weighted signal drops since activity-evoked vasodilation leads to an increased blood volume with more iron oxide particles in a given voxel, which shortens the magnitude of T2* and diminishes the signal (Mandeville et al., 1998). The peak CBV-weighted signal was mainly located at individual arterioles with the time course of the negative CBV-weighted signal originated from a selected arteriole (Figures 1C and S1). The averaged hemodynamic time courses from regions of interest of venule and arteriole voxels showed that the positive BOLD signal is much higher in venule than arteriole voxels (Figure 1D). Similarly, the negative CBV-weighted signal is much lower in arteriole than venule voxels (Figure 1D). Interestingly, the CBV-weighted signal in arteriole voxels returned to baseline faster than that in venules. An extended temporal response for the CBV-weighted signal in venules has been previously reported for CBV-based fMRI studies (Mandeville et al., 1999; Silva et al., 2007; Drew et al., 2011) and may be inferred from optical imaging (Drew et al., 2011). These results demonstrate the feasibility of bSSFP-fMRI for real-time single-vessel hemodynamic mapping from arterioles. They complement the venule-dominated approach for the positive BOLD signal mainly in terms of oxy/deoxy-hemoglobin ratio changes.

Single-Vessel bSSFP fMRI Mapping the Resting-State BOLD and CBV-Weighted Signals

Moving beyond the evoked single-vessel fMRI mapping, the ultra-slow resting-state hemodynamic signal was directly mapped with the bSSFP single-vessel fMRI method. Individual arterioles or venules identified from the A-V map were selected as seed voxels to calculate the correlation maps of both BOLD and CBV-based fluctuations in the fMRI signal (Figure 2); the frequency range was 0.01 to 0.1 Hz. As shown in the example data of Figure 2B, venule voxels were highly correlated to each other but less correlated for arterioles in the resting-state BOLD correlation maps (Movie S1). In contrast, as shown in the example data of Figure 2C, arteriole voxels were highly correlated but venules essentially uncorrelated in the resting-state CBV-weighted correlation maps (Movie S2). The power spectral density shows that the venule-specific BOLD and arteriole-specific CBV-weighted fMRI signal fluctuate within the ultra-slow frequency range of 0.01 to 0.04 Hz (Figure 2D). Similar to the evoked fMRI maps, the significant BOLD signal correlations were primarily located at venule voxels, i.e., the venule-specific connectivity map, and the significant CBV-weighted signal correlation were primarily located at arteriole voxels, i.e., the arteriole-specific connectivity map, during the resting state.

To better characterize the spatial and temporal features of the single-vessel fMRI fluctuations, the vessels identified in the A-V map were paired to calculate correlation coefficients (Figure 3A). First, the values of the correlation coefficient for all vessel pairs (arteriole pairs: A-A; venule pairs: V-V) were plotted as the function of inter-vessel distance. For the BOLD signal fluctuation, V-V pairs show a stronger correlation than that of A-A pairs in the large field-of-view, up to 5 × 5 mm. This highlights the large-scale extent of the BOLD-based venule functional connectivity (Figures 3B and 3F). In contrast to the case for BOLD, a stronger correlation was detected for the A-A pairs than the V-V pairs for the CBV-weighted signal fluctuations. These correlations diminished over a vessel separation distance of 2 mm (Figures 3C and 3G). This spatial scale is consistent with the scale for correlations in vasomotion across arterioles, as detected by two-photon imaging of vessel diameter (Mateo et al., 2017). This spatial scale also corresponds to the $\sim$2 mm electrotonic length for conduction through endothelial cells (Segal and Duling, 1989). The color-coded correlation matrices showed higher BOLD values of correlation in V-V pairs than the other pairs (Figure 3D) and higher CBV-weighted values of correlation in A-A pairs than the other pairs (Figure 3E), which is quantitatively represented as the function of vessel pair distance (Figures 3F and 3G).

Next, Spectral coherence analysis from paired venules or arterioles was performed to characterize the full frequency spectrum of the vessel-specific fMRI signal fluctuation during the resting state. The coherent oscillation was mainly distributed in the 0.01–0.04 Hz frequency range for both BOLD and CBV-weighted fMRI signal fluctuation (Figures 3H and 3I, similar to the spectral power, Figure 2D). Quantitative analysis demonstrates that the coherence coefficient of venule pairs is significantly higher than that of arteriole pairs for the BOLD signal fluctuation. In contrast, for the CBV-weighted signal fluctuation, the coherence coefficient of arteriole pairs is significantly higher than that of venule pairs for the 0.01–0.04 Hz frequency bandwidth (Figures 3J and 3K). In addition to the seed-based analysis, independent component analysis (ICA) was used to determine the venule-specific dynamic connectivity for BOLD signal fluctuation and the arteriole-specific dynamic connectivity for CBV-weighted signal fluctuation (Figures S2A–S2G). One component appeared specific for vessel-specific BOLD ultra-slow oscillations and another for CBV-weighted the ultra-slow oscillations (Figures S2F and S2G). These results confirm distinct vessel-specific correlation patterns for BOLD and CBV-weighted signal fluctuation.

Vessel-specific BOLD correlation maps were detected in rats anesthetized with isoflurane (<1.2% [v/v]) (Figures S2H–S2M). The frequency range of oscillations extended to $\sim$0.1 Hz with peak power levels at 0.01–0.04 Hz, similar to those observed with rats anesthetized with α-chloralose (Figure 2). This result suggests that while oscillation at frequencies above $\sim$0.1 Hz may vary depending on the anesthetized or awake brain state (Obrig et al., 2000; Du et al., 2014; Ma et al., 2016; Mateo et al., 2017), the ultra-slow frequencies are fairly stable (<0.1 Hz) under uniform ventilation. It is noteworthy that blood pressure was acquired simultaneously with fMRI, but no clear ultra-slow frequency fluctuation was observed from either of the physiological parameters (Figure S3).

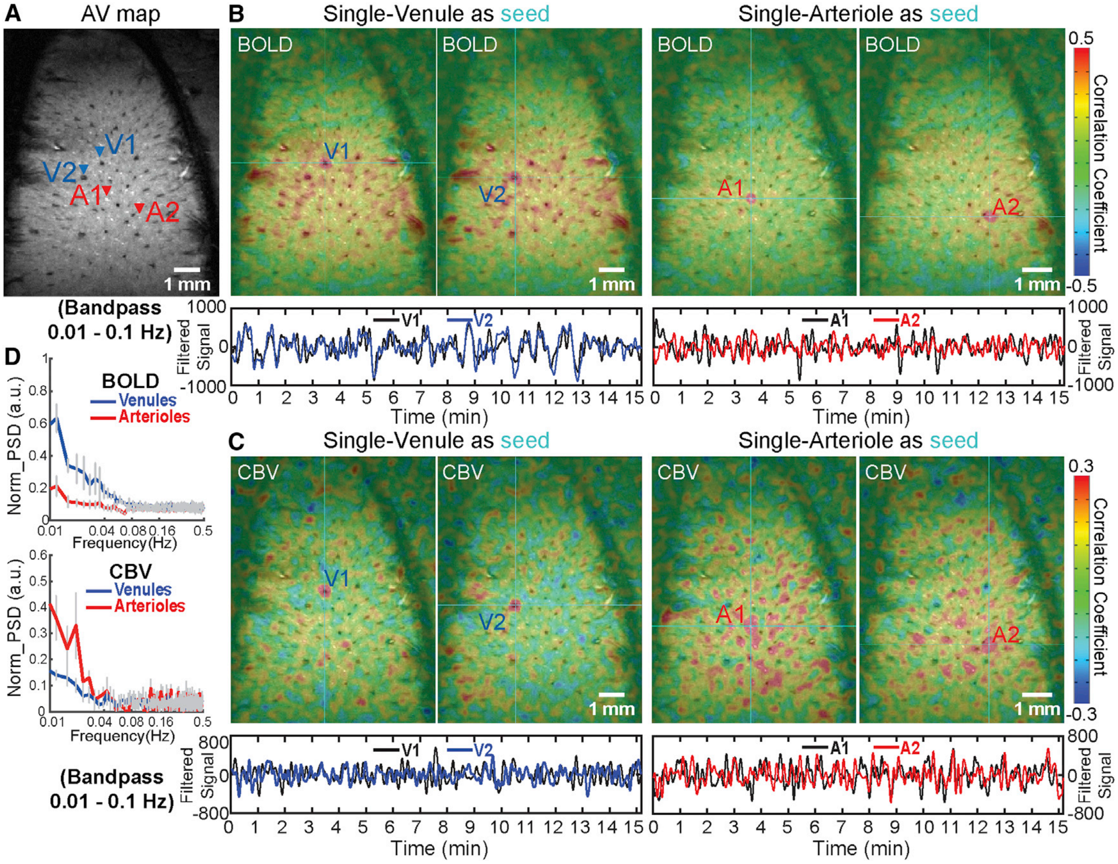

Figure 2. Using bSSFP-Based rs-fMRI to Map Vascular-Specific Correlation Patterns

(A) The A-V map shows individual penetrating arterioles and venules (blue arrowheads, venules; red arrowheads, arterioles).

(B) The seed-based BOLD rs-fMRI correlation maps (0.01–0.1 Hz; seeds: cyan crosshairs) of two venule seeds (V1 and V2; left) and CBV rs-fMRI correlation maps (0.01–0.1 Hz; seeds: cyan crosshairs) of two arteriole seeds (A1 and A2; right). The lower panel is the BOLD signal time course of the two venule seed ROIs and two arteriole seed ROIs.

(C) The seed-based CBV rs-fMRI correlation maps (0.01–0.1 Hz; seeds: cyan crosshairs) of two venule seeds (V1 and V2; left) and CBV rs-fMRI correlation maps (0.01–0.1 Hz; seeds: cyan crosshairs) of two arteriole seeds (A1 and A2; right). The lower panel is the CBV signal time course of the two venule seed ROIs and two arteriole seed ROIs.

(D) The power spectral density (PSD: arbitrary unit [a.u.]) of the venule and arteriole-specific resting-state BOLD (upper) and CBV (lower) fMRI time courses. See also Figures S2 and S3.

Comparison of Vessel-Specific BOLD and CBV fMRI Signals with Simultaneous Neuronal Calcium Recording

To characterize the potential neural correlates of the vessel-specific fMRI signal fluctuation, a genetically encoded calcium indicator, GCaMP6f, was expressed in neurons of forepaw S1 or vibrissa S1 cortex for simultaneous intracellular [Ca^{2+}] recording and fMRI (Figure S4); immunostaining verified the GCaMP expression in cortical neurons (Figure S4B). Evoked and spontaneous intracellular [Ca^{2+}] transients were recorded in the deep layers with fiber photometry concurrent with the local field potential (LFP) (Figures 4A and S4C–S4F). Evoked [Ca^{2+}] spikes were acquired simultaneously with single-vessel bSSFP-fMRI for comparison with the venule-specific positive BOLD signal and arteriole-specific negative CBV-weighted signal (Figures S4E and S4F). These results demonstrate the feasibility of simultaneous single-vessel fMRI with intracellular [Ca^{2+}] fiber optic recording.

We sought to characterize the potential neuronal origin of the vessel-specific fMRI signal fluctuation. We first considered the correlation between changes in intracellular [Ca^{2+}] in the 0.01 to 0.1 Hz band and the resting-state BOLD signal. It shows vessel-specific positive correlation patterns that are similar to the venule-seed based correlation maps from rats anesthetized with α-chloralose (Figures 4B and 4C); time courses of representative venules (V1, V2), and changes in intracellular [Ca^{2+}] are shown in Figure 4D. The correlation coefficient between the intracellular [Ca^{2+}] and the venule BOLD signal (Ca^{2+}-V) was significantly higher than that with the arteriole BOLD signal (Ca^{2+}-A) (Figure 4F). Cross-correlation analysis between the changes in intracellular [Ca^{2+}] and the venule-specific BOLD signal showed a positive peak at the averaged lag time of 2.3 ± 0.2 s (Figures 4E and 4G). The vessels at the cortical surface had the longest lag, up to 3–5 s (Figure 4C), which agrees with the lag reported previously by cross-correlation analysis of the

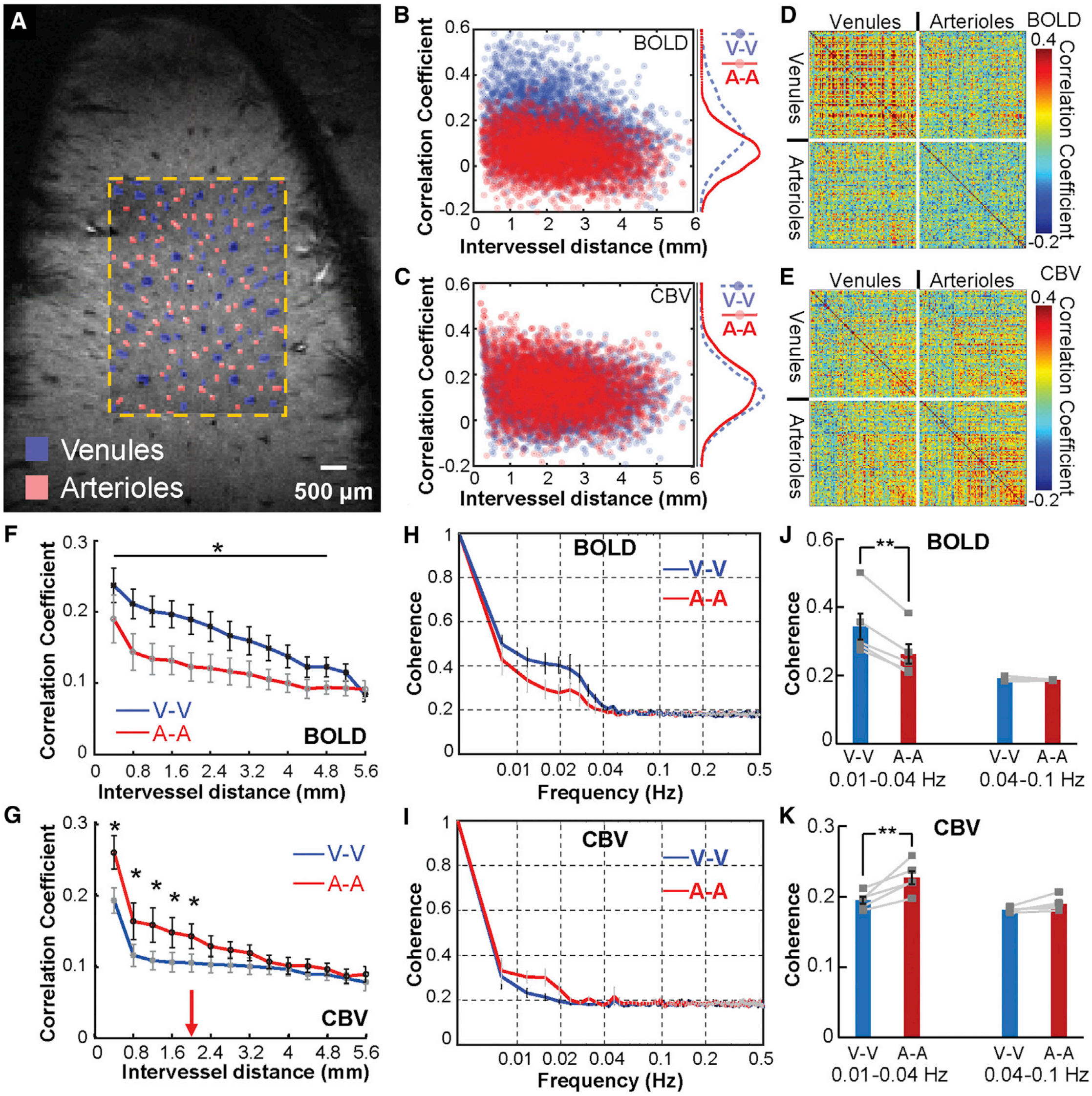

Figure 3. Vascular Dynamic Network Connectivity in Rats at 14.1T

(A) The A-V map of one representative rat (arteriole ROIs in red and venule ROIs in blue).

(B and C) Scatterplots of the correlation coefficient (CC) of BOLD (B) and CBV (C) fMRI from venule-to-venule (V-V) pairs, arteriole-to-arteriole (A-A) pairs as the function of the inter-vessel distance from one representative rat.

(D and E) The correlation matrices of all vessel pairs for the BOLD (D) and CBV (E) fMRI from one representative rat.

(F and G) The mean CC value of the BOLD signal from the venule pairs is significantly higher than that of the arteriole pairs with large spatial inter-vessel distance (>5 mm) (F, n = 5, mean ± SEM, *, paired t test, $p < 0.03$). In contrast, the mean CC value of the CBV signal from the arteriole pairs is significantly higher than that of the venule pairs with small spatial inter-vessel distance (~2 mm) (G, n = 5, mean ± SEM, *, paired t test, $p < 0.03$).

(H and I) The averaged coherence graph of paired venules and arterioles from BOLD/CBV fMRI (H), BOLD fMRI, n = 5, (I), CBV fMRI, n = 5 rats, mean ± SEM.

(J) The mean BOLD coherence coefficient of the venule pairs is significantly higher than that of arteriole pairs at the low-frequency range (0.01–0.04 Hz) (n = 5, paired t test, **p = 0.0009).

(K) The mean CBV coherence value of paired venules is significantly lower than that of paired arterioles at the low-frequency range (0.01–0.04 Hz) (n = 5 rats, paired t test, **p = 0.007).

See also Figures S2 and S3.

calcium signal and hemoglobin-based intrinsic optical signal (Du et al., 2014).

We next considered the correlation of the calcium signal in the 0.01–0.1 Hz band with the single-vessel CBV-weighted fMRI signal obtained after the injection of iron oxide particles. Similar to the arteriole-seed based CBV correlation maps (Figure 4I), the highly correlated voxels with changes in intracellular [Ca^{2+}] were located mainly at arterioles, but with negative values of the correlation coefficient (Figure 4J); the time courses of representative arterioles (A1, A2) and the calcium signal are shown in Figure 4K.

Please cite this article in press as: He et al., Ultra-Slow Single-Vessel BOLD and CBV-Based fMRI Spatiotemporal Dynamics and Their Correlation with Neuronal Intracellular Calcium Signals, Neuron (2018), https://doi.org/10.1016/j.neuron.2018.01.025

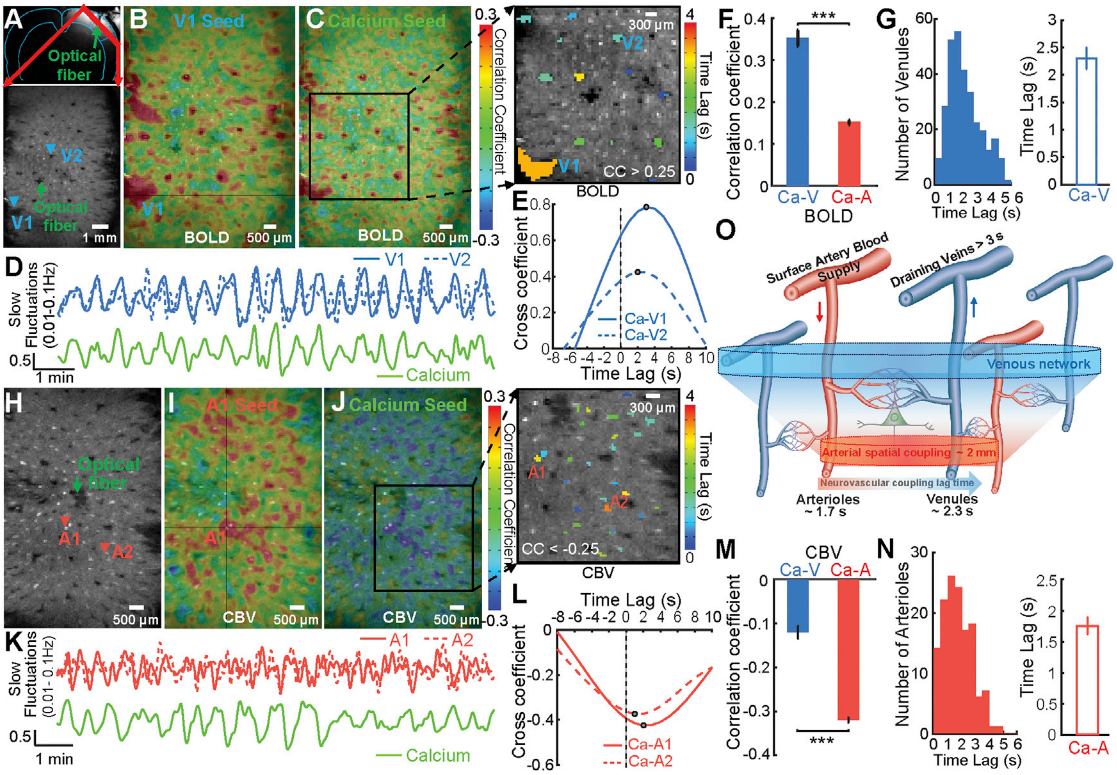

Figure 4. Correlation Analysis of the Single-Vessel BOLD/CBV fMRI with GCaMP6f-Mediated Calcium Signal

(A) The coronal view of the anatomical MR image with the optic fiber targeting the vibrissa S1 (upper). The A-V map from a 2D slice covering the deep cortical layer (lower).

(B) The seed-based BOLD correlation maps from one representative venule voxels (V1) overlaid on the A-V map.

(C) The correlation map between the BOLD fMRI signal and the calcium signal (band-pass filter: 0.01–0.1 Hz). Inset is a representative color-coded lag time map between the calcium signal with the BOLD fMRI of individual venules (CC > 0.25).

(D) The time courses of the BOLD fMRI signal from vessel voxels (V1: blue, solid line; V2: blue, dotted line) and the slow oscillation calcium signal (green).

(E) The cross-correlation function of the calcium signal and BOLD fMRI signal of two representative venules (Ca-V1 and Ca-V2) with positive peak coefficients at the lag time 2–3 s.

(F) The mean correlation coefficient of the calcium signal with the BOLD fMRI signal of venules is significantly higher than that of arterioles (n = 7 rats, mean ± SEM, paired t test, ***$p = 2.5 \times 10^{-5}$).

(G) The histogram of venules with lag times varied from 0.5 to 6 s (CC > 0.25) and mean lag time at 2.30 ± 0.19 s. (n = 7, mean ± SEM).

(H) The A-V map with the markers of arterioles (arteriole 1: A1, arteriole 2: A2, red arrowheads) and optical fiber (green arrowhead).

(I) The seed-based correlation maps of CBV fMRI from one arterioles voxel (A1) overlaid on the A-V map.

(J) The correlation map between the CBV fMRI and calcium signal (band-pass filter: 0.01–0.1 Hz). Inset is a representative color-coded lag time map between the calcium signal and the CBV fMRI signal of individual arterioles (CC < −0.25).

(K) The time course of the CBV fMRI signal from arteriole voxels (red, solid and dotted lines) and the slow oscillation calcium signal (green).

(L) The cross-correlation function of the calcium signal and CBV fMRI signal of two representative arterioles (Ca-A1 and Ca-A2) with negative peak coefficients at the lag time 1–2 s.

(M) The mean correlation coefficient of the calcium signal with the CBV fMRI signal of arterioles is significantly higher than that of venules (n = 4, mean ± SEM, paired t test, ***p = 0.0002).

(N) The histogram of arterioles with lag times varied from 0.5 to 5 s (CC < −0.25). The mean lag time is 1.76 ± 0.14 s (n = 4, mean ± SEM), which is significantly shorter than the lag times of the calcium and venule BOLD signal (BOLD, n = 7, CBV, n = 4, t test, p = 0.025).

(O) The schematic drawing of the spatial and temporal correlation patterns of the slow oscillation signal coupling from neurons to vessels.

See also Figures S4–S7 and S10 and Table S2

Quantitative analysis showed that the correlation between the intracellular [Ca^{2+}] and the CBV-weighted signal of arterioles (Ca^{2+}-A) was significantly higher than that of venules (Ca^{2+}-V) (Figure 4M). The oscillation in intracellular [Ca^{2+}] also led the arteriole-specific CBV-weighted signal fluctuations, as observed by the cross-correlations of two representative arterioles as the function of lag time (Figure 4L). Different arterioles showed varied lags with a mean value at 1.8 ± 0.2 s (Figure 4N). Cross-correlation of the intracellular [Ca^{2+}] with the arteriole CBV-weighted signal showed a shorter lag time than that with the venule BOLD signal (Figures 4G and 4N). Meanwhile, the oscillation in intracellular [Ca^{2+}] was found to be correlated with the CBV-weighted signal of a few venules with lag time of 5–10 s (Figure S5). This result indicates the passive venule dilation usually

Please cite this article in press as: He et al., Ultra-Slow Single-Vessel BOLD and CBV-Based fMRI Spatiotemporal Dynamics and Their Correlation with Neuronal Intracellular Calcium Signals, Neuron (2018), https://doi.org/10.1016/j.neuron.2018.01.025

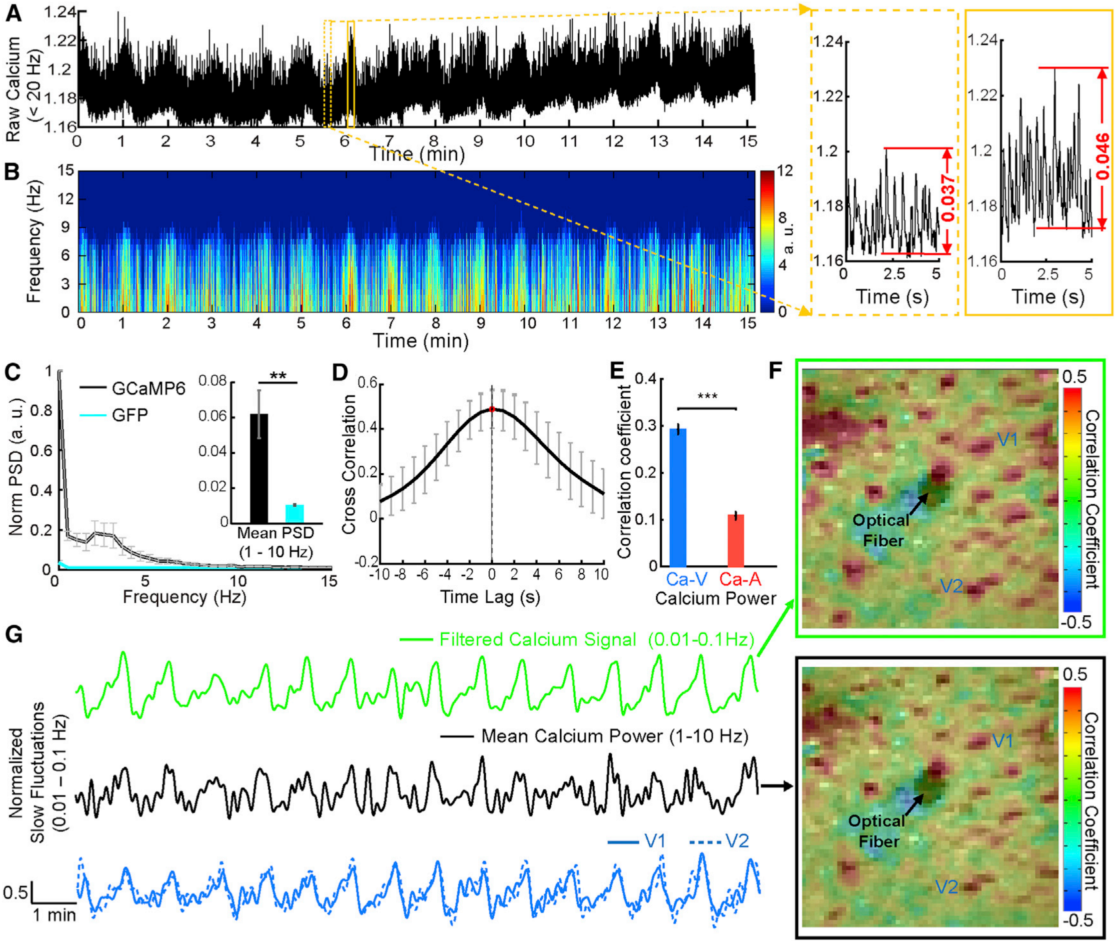

Figure 5. The Correlation between the Calcium Power Spectral Profile with Vessel-Specific fMRI Signal

(A) The time course of the calcium signal (low-pass filter: 20 Hz) from one representative rat at the resting state with enlarged 5 s windows of the calcium spikes identified at different periods (dotted and solid yellow boxes).

(B) The time-varying power spectrogram of the calcium signal is plotted as the function of time from 0.5 to 15 Hz (discrete Fourier transform in 1 s Hamming window; the sampling rate is 1 Hz to match the TR of fMRI signal).

(C) The normalized PSD from the rats with GCaMP6 (black, n = 5) or GFP (cyan, n = 4) indicates the mean PSD (1–10 Hz) of GCaMP6 is significantly higher than that of GFP (**p = 0.001, t test).

(D) The cross-correlation function of the calcium signal and the averaged power (1–10 Hz) profile from the calcium spectrogram (band-pass filter with 0.01–0.1 Hz) illustrates the peak cross-correlation coefficient at 0 s lag time (n = 4, mean ± SEM).

(E) The mean correlation coefficients of the averaged calcium power signal with the BOLD fMRI signal of venules are significantly higher than that of arterioles (***$p = 1.9 \times 10^{-4}$, pair t test, n = 4, mean ± SEM).

(F) The correlation maps between the SSFP-based BOLD fMRI signal and the slow oscillation calcium signal (band-pass filter: 0.01–0.1 Hz, upper) and the mean calcium power spectral profile (1–10 Hz, lower) show similar venule-specific correlation patterns.

(G) The time series (band-pass filter: 0.01–0.1 Hz) of the slow oscillation calcium signal (green), the mean calcium spectral power profile (1–10 Hz) (black), the BOLD fMRI signal from two venules (V1, V2; blue, solid and dotted blue lines).

See also Figure S6.

detected as the post-stimulus undershoot of the evoked BOLD signal results from increase blood flow following prolonged stimulation (Buxton et al., 1998; Silva et al., 2007; Drew et al., 2011).

Besides the ultra-slow oscillation, the GCaMP6-mediated calcium signal exhibited EEG-like rhythmic neuronal activity, showing significantly higher spectral power at the 1–10 Hz frequency range than that of the fluorescent signal detected from the GFP-expressing cortex of control rats (Figures 5A–5C). Cross-correlation of the spectral power in the 1–10 Hz and ultra-slow oscillatory calcium signal fluctuation (0.1–0.01 Hz) showed peak positive correlation coefficient at zero time lag (Figure 5D). In addition, the spectral power in 1–10 Hz was correlated to the vessel-specific BOLD signal, showing the correlation coefficient of spectral power with the venule BOLD signal is significantly higher than that of the spectral power with the arteriole BOLD signal, similar to the ultra-slow oscillatory calcium signal fluctuation (Figures 4B–4D and 5E–5G). This result further demonstrates the neuronal correlates of the vessel-specific fMRI

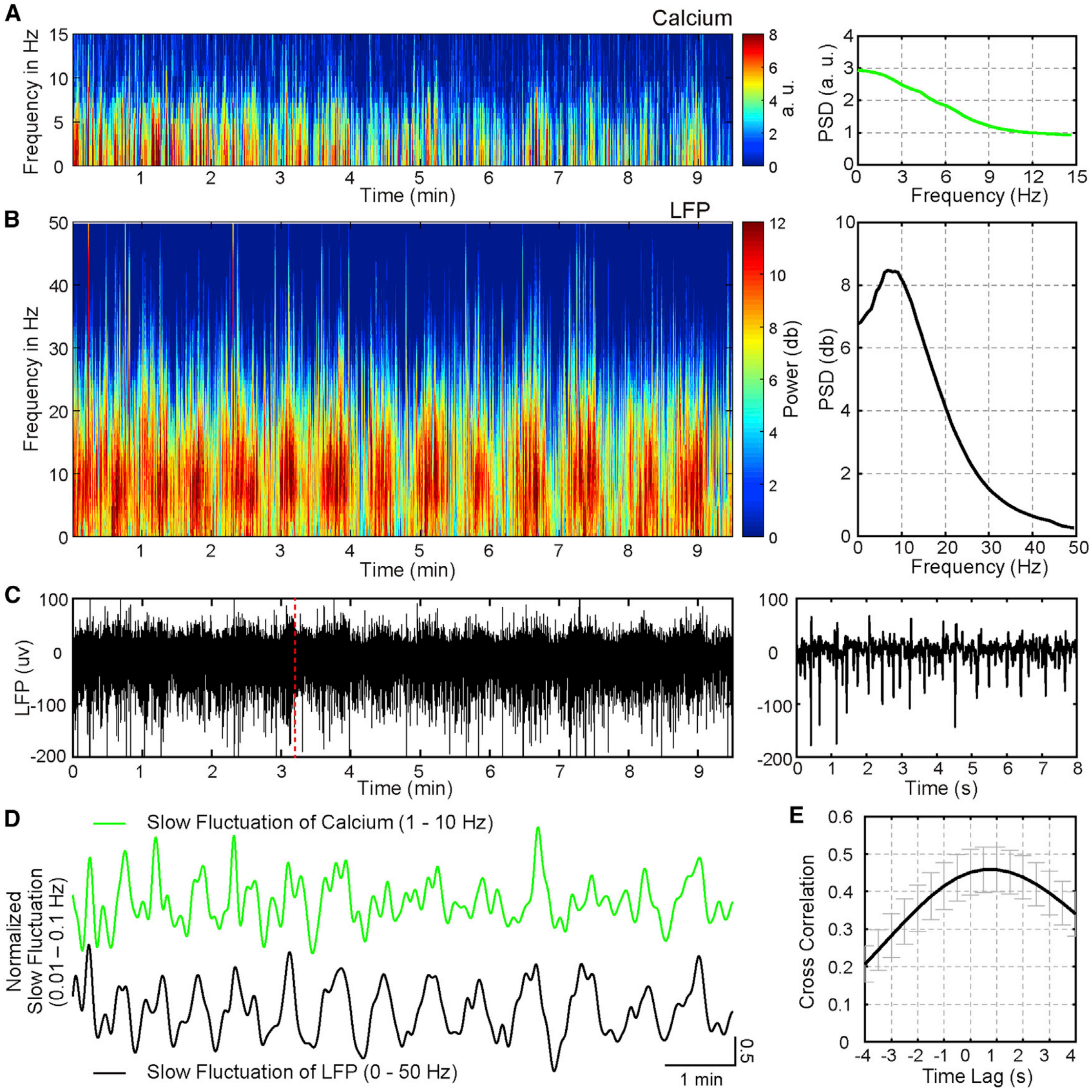

Figure 6. The Spectrogram of Simultaneous Calcium and Electrophysiological Signal under α-chloralose Anesthesia

(A) Spectrogram of calcium signal during light anesthesia.

(B) Spectrogram of local field potential (LFP) at light anesthesia from multi-taper spectral estimates (1 s sliding window with 0.1 s steps, 9 tapers). The right panel shows the averaged power spectral density (PSD).

(C) The time course of the LFP signal under light anesthesia.

(D) The mean calcium spectral power profile (band-pass filter: 0.01–0.1 Hz of 1−10 Hz, green) and the mean LFP spectral power profile (0–50 Hz, black) at light anesthesia.

(E) The cross-correlation function of the averaged LFP power (0–50 Hz) from LFP spectrogram and the averaged calcium power (1–10 Hz) profile from the calcium spectrogram (band-pass filter with 0.01–0.1 Hz) illustrates the peak cross-correlation coefficient at 0.8 s lag time at light anesthesia (n = 4, mean ± SEM).

See also Figures S5 and S6.

signal fluctuation in the cerebrovascular network. Finally, the cartoon of Figure 4O summarizes the spatial and temporal patterns of neurovascular hemodynamic signal fluctuation from arteriolar to venous networks.

Also noteworthy is that the power spectral density shows elevated power at frequencies below 0.1 Hz for the venule BOLD and arteriole CBV-weighted signal, as well as for the simultaneously acquired calcium signal at the light anesthesia (Figures 2D and S6). In contrast, at the deep anesthesia level with α-chloralose, the ultra-slow oscillation pattern was undetectable for both fMRI and changes in [Ca^{2+}] concentration in the same rats (Figure S6), but the evoked BOLD and CBV fMRI signals and changes in [Ca^{2+}] concentration remained (Figures S4E and S4F). This result further supports the neural correlates of the single-vessel fMRI signal fluctuation. Meanwhile, simultaneous LFP and intracellular [Ca^{2+}] recording was performed to specify the ultra-slow oscillatory signal at different anesthesia levels (Figures 6 and S7). The spectrogram of the spontaneous

Please cite this article in press as: He et al., Ultra-Slow Single-Vessel BOLD and CBV-Based fMRI Spatiotemporal Dynamics and Their Correlation with Neuronal Intracellular Calcium Signals, Neuron (2018), https://doi.org/10.1016/j.neuron.2018.01.025

LFP and intracellular [Ca^{2+}] signal showed similar ultra-slow oscillation patterns in rats under the light anesthesia level (Figures 6A–6D). Cross-correlation of the LFP and intracellular [Ca^{2+}] signal power profile showed positive correlation coefficients (0.46 ± 0.06) at the time lag (0.73 ± 0.13 s), showing the ultra-slow oscillatory LFP signal leads the intracellular [Ca^{2+}] signal (Figure 6E). Similar to the single-vessel fMRI data, these results showed consistent correlation features at the light anesthesia level (Figure 5) but not at the deep anesthesia (Figures S7A–S7E). In addition, the ultra-slow oscillatory correlation of the LFP power profile and intracellular [Ca^{2+}] fluctuations were detected in rats anesthetized with 1.2% (v/v) isoflurane (Figures S7F–S7I). These results suggest that the neuronal and vascular hemodynamic oscillations are highly correlated in the anesthetized brain and that the correlation is dampened when the neural activity is suppressed with deep anesthesia.

Mapping Vascular Network Connectivity in the Human Brain under 3T and 9.4T

The single-vessel mapping scheme was implemented to characterize the prospects for vessel-specific fMRI correlation patterns in awake human subjects. Although bSSFP shows great advantage for the high-field fMRI in the rat brain as a consequence of decreased distortion and reduced extravascular effect compared to the EPI method, the single-echo bSSFP method acquires single k-space line per echo and takes longer time than the EPI method to acquire multi-slice high-resolution images (Budde et al., 2014). We established single-vessel fMRI human brain mapping with the EPI method. First, the fMRI signal of sulcus veins in the occipital lobe was mapped using EPI-fMRI at 3T. Upon the checkerboard visual stimulation, the evoked BOLD signal was located primarily at venous voxels with a sparsely distributed patchy pattern that was previously reported (Menon et al., 1993) (Figures 7A–7C and 7F; Movie S3). Besides the task-related functional maps, the seed-based correlation maps from resting-state fMRI demonstrated vein-dominated correlation spatial patterns (Figures 7D and 7G; Movie S4). The coherence analysis of paired venous voxels showed coherent ultra-slow oscillation of the awake human subjects up to ~0.1 Hz (Figure 7H), which was much higher than the oscillation frequency detected in anesthetized rats (Figure 3H). The correlation coefficients of paired venous voxels were plotted as the function of the intra-hemispheric and inter-hemispheric vessel distances (Figure 7I). The values of the correlation decreased as the function of the intra-hemispheric vessel distance but showed significantly higher values for the inter-hemispheric venous voxel pairs (Figure 7J), similar to previously established spatial vasomotion correlation patterns in awake mice (Mateo et al., 2017). The low-frequency oscillation around 0.1 Hz has been previously reported in the visual cortex of the human brain with conventional resting-state fMRI method (Mitra et al., 1997). Also, when EPI images were spatially smoothed with different kernels from 1 to 5 mm, the vessel-specific spatial patterns merged to functional blobs similar to the conventional functional connectivity maps (Biswal et al., 1995; Smith et al., 2009) (Figures 7K and 7L).

The seed-based analysis was performed before and after the regression of respiration and heartbeat relevant temporal artifacts (Figures S8A–S8F), showing the little difference in the vessel-specific spatial patterns (Figures S8G–S8M). In addition, ICA analysis specified the highly correlated venous voxels at multiple slices, showing a 3D vascular dynamic correlation structure through the main branches of cerebral vasculature (Figures S9A–S9D; Movie S5). These results demonstrate that the hemodynamic fMRI signals from central veins through sulci or at the gyrus surface are highly correlated, representing large-scale vascular dynamic network connectivity detectable with the 3T MR scanner.

To characterize the hemodynamic signal fluctuation in vessels penetrating cortical gray matter, we mapped the single vessel-based resting-state fMRI signal at 9.4T. The multiple 2D EPI images were acquired with an in-plane resolution of 500 × 500 μm^2 and 800 μm thickness at a TR of 1 s. In parallel, a single-vessel A-V map was acquired to better characterize the location of individual sulcus arteries and veins, as well as a few intracortical veins (Figures 8A–8C). Similarly, the BOLD signal was highly correlated on venous voxels, but not on artery voxels (Figures 8D and 8E). In the enlarged correlation maps, a few intracortical veins penetrating the gray matter could be spotted on the A-V map, given their unique vascular orientation through the 2D slice, showing a strong correlation to each other (Figures 8B, 8C, S9E, and S9F). Furthermore, coherence analysis of paired veins showed a coherent frequency range less than ~0.1 Hz, which is consistent with previous brain ultra-slow oscillation studies (Obrig et al., 2000) (Figure 8G). This result provides a good example for the illustration of vascular correlation of the selected intracortical veins penetrating cortical gray matter at 9.4T. This result shows the translational potential of high-resolution single-vessel fMRI to associate anatomical vascular biomarkers with prognostic dynamic indicators of neurovascular disease and vascular dementia in the brain.

DISCUSSION

We have demonstrated that a single-vessel fMRI mapping scheme reveals the spatial and temporal features of vessel-to-vessel hemodynamic correlations in anesthetized rats and in awake human subjects. With regard to rats, BOLD-specific venous signals and the CBV-specific arteriolar signals evolve at ultra-slow timescales, with frequency components between 0.01 and 0.04 Hz (Figure 3). Both signals show a causal relationship to the simultaneously acquired calcium signal (Figure 4). With regard to humans, the ultra-slow oscillation was observed in the BOLD signal for frequencies up to 0.1 Hz and vessel-to-vessel correlations are strong (Figure 8). This work demonstrates the feasibility to apply a multi-modal fMRI platform to measure the neuronal correlates of resting-state hemodynamic signal fluctuation from arteriolar to venous networks at the scale of individual vessels.

Technical Advances

The attainment of single-vessel imaging with high SNR was achieved based on three factors: a high magnetic field to enhance the transverse signal; a bSSFP sequence with high SNR efficiency per time unit; and a small radio frequency coil with appropriate sample loading to optimize the detection from local cortical regions. These factors ensured that the temporal

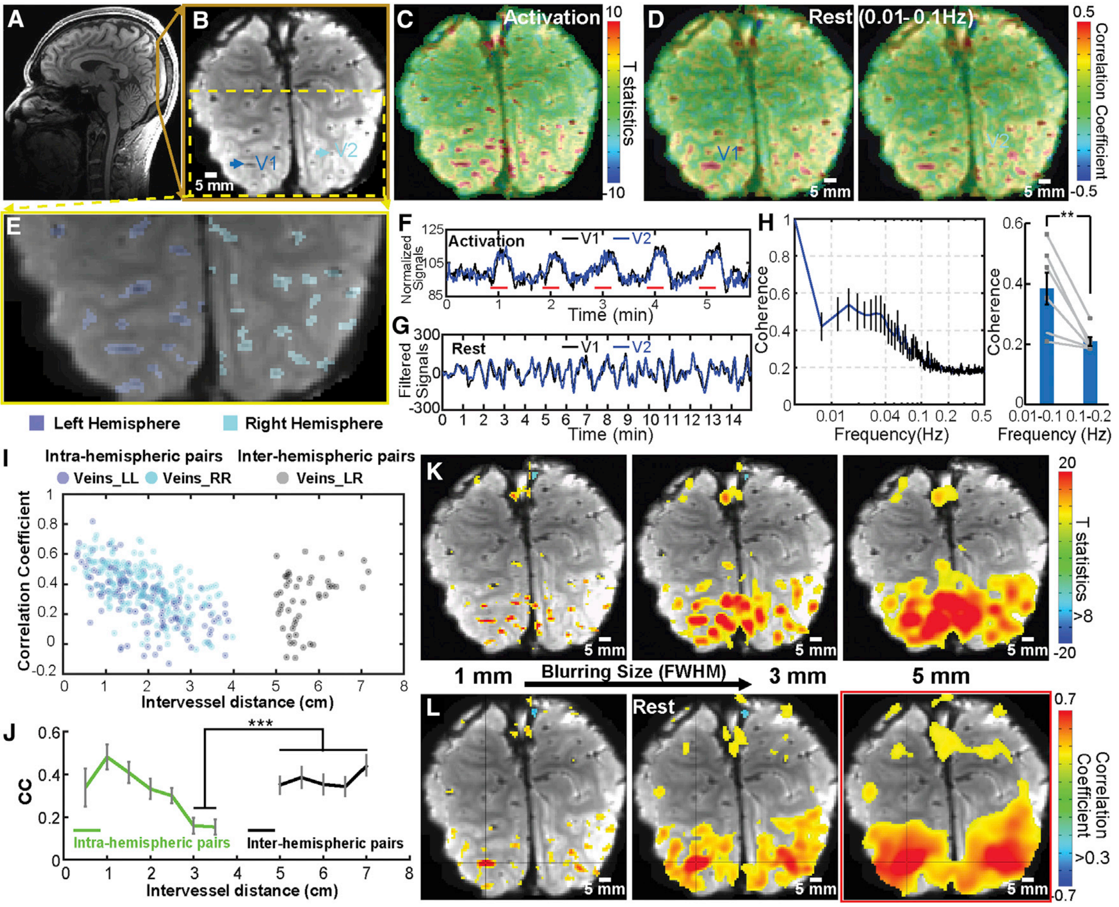

Figure 7. The Task-Related and Resting-State Single-Vessel fMRI Mapping in Awake Human Subjects at 3T

(A) A sagittal view of the human brain with a 2D EPI slice located in the occipital lobe.

(B) An averaged EPI image shows the pial veins in sulci as dark dots.

(C) The checkerboard visual stimulation-evoked BOLD functional map with peak BOLD signals located at pial veins.

(D) The seed-based BOLD correlation maps (0.01–0.1 Hz; seeds: two veins [V1 and V2]) demonstrate vessel-dominated patterns.

(E) The magnified view of the averaged EPI image from one representative subject (vein ROIs, left hemisphere, blue, right hemisphere, cyan).

(F and G) The time courses of two veins in the task-related (F) and resting-state (G) (0.01–0.1 Hz) conditions.

(H) The coherence graph of paired veins exhibits coherent oscillation at the frequency range of 0.01–0.1 Hz significantly higher than the higher frequency range (0.1–0.2 Hz; n = 6, mean ± SEM, **, paired t test, p = 0.008).

(I) The scatterplot of the correlation coefficient (CC) from intra and inter-hemispheric vein pairs.

(J) The mean CC of inter-hemispheric vein pairs with the intervessel distance between 5–7 cm is significantly higher than that of intra-hemispheric vein pairs with distance between 3–3.5 cm. (***, n = 6, mean ± SEM, t test, p = 0.0002).

(K and L) The evoked functional (K) and resting-state correlation (L) maps were smoothed from 1 mm to 5 mm (FWHM).

See also Figures S8 and S9.

fluctuation of the vessel-specific fMRI signal was not dominated by machine-based technical noise, but rather represented the physiological state of the brain. This issue was further verified by the anesthetic dose-dependent study, which indicated that the vessel-specific fMRI signal fluctuation could be dampened even though the SNR remained unchanged (Figure S6). Besides the technical noise, artifacts from physiological motion can be erroneously intrinsically linked to the functional connectivity (Hu et al., 1995; Murphy et al., 2013). Numerous strategies have been developed to regress out the potential artifacts, or identify the functional node-specific component using ICA analysis (Glover et al., 2000; McKeown et al., 2003). Nonetheless, a lack of standard criteria to distinguish the contribution from brain signal fluctuation versus physiological motion artifacts limits the reliability of functional connectivity. We nominally expect that the pattern of correlations should be insensitive to global motion artifacts. Further, the enhanced correlations in the BOLD response for pairs of venules versus arterioles (Figures 3F, 3H, 3J, and 8F) and the enhanced correlations in the CBV response for arterioles versus venules (Figures 3G, 3I, and K) as a function of frequency are highly unlikely to result from known artifacts.

The detected bSSFP signal change is a mixture of intravascular and extravascular contributions. The intravascular signal is given by the steady-state contrast of passband bSSFP, which

Please cite this article in press as: He et al., Ultra-Slow Single-Vessel BOLD and CBV-Based fMRI Spatiotemporal Dynamics and Their Correlation with Neuronal Intracellular Calcium Signals, Neuron (2018), https://doi.org/10.1016/j.neuron.2018.01.025

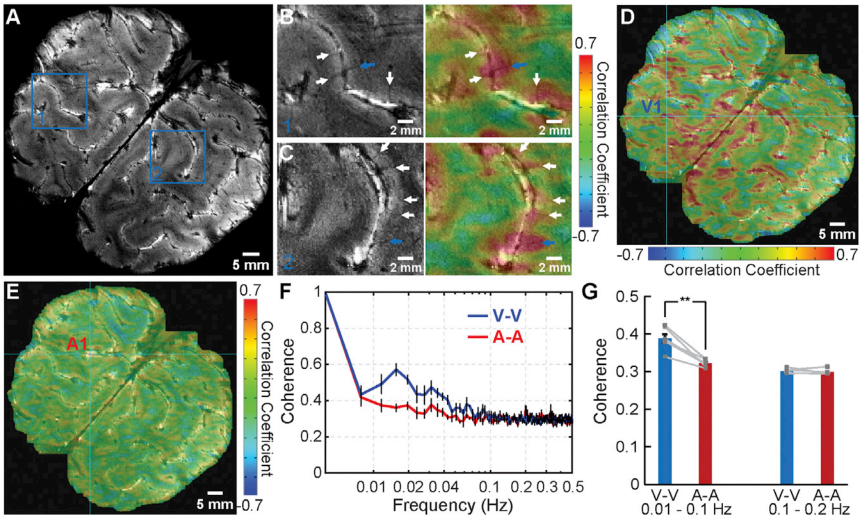

Figure 8. The Intracortical Vascular Dynamic Mapping with 9.4T

(A) The A-V map is acquired from a 2D slice across the occipital lobe.

(B and C) The intra-cortical veins (arrows) in the magnified view of region 1 and region 2 in the A-V map (left). The right panel shows the correlation map based on the selected seeds (the intracortical veins: blue arrows) with highly correlated voxels detected on the other intracortical veins (white arrows) in the gray matter.

(D and E) The seed-based correlation maps with vein 1 (V1), artery 1 (A1) as seeds, respectively (seeds: cyan crosshairs).

(F) The coherence graph of paired veins (blue) and arteries (red) identified by the AV map demonstrates the slow fluctuations from 0.01 to 0.1 Hz.

(G) The mean coherence coefficients of the paired veins are significantly higher than that of the paired arteries at low frequency (0.01–0.1 Hz) (n = 6, mean ± SEM, paired t test, **p = 0.0009).

See also Figure S9.

is proportional to $\sqrt{T_2/T_1}$ (Scheffler and Lehnhardt, 2003). Given the high spatial resolution of the bSSFP fMRI imaging, the BOLD contrast from venules and the CBV-based contrast from arterioles of vessel voxels remained highly T2-weighted because of the fast T2 decay of deoxygenated venule blood and iron oxide enriched arteriole blood (Lee et al., 1999; Blockley et al., 2008). The extravascular contribution depends on the vessel size. As for spin echoes, the rapid refocusing in bSSFP produces dynamic averaging that reduces the extravascular effects of the cortical penetrating vessels larger than 10–20 μm (Bieri and Scheffler, 2007; Scheffler and Ehses, 2016). Therefore, the observed signal changes with high spatial resolution bSSFP were mainly intravascular. It is noteworthy that the blood flow could contribute to the BOLD fMRI signal fluctuation based on the in-flow effect, given the short TR of the bSSFP sequence at a given flip angle (Kim et al., 1994). This is especially true for arterioles. However, the BOLD signal fluctuation in arterioles showed significantly lower correlation than that of venules, indicating that the in-flow effect is not the primary contributor to the vascular dynamic correlation patterns (Figures 2 and 3).

BOLD versus CBV-Weighted fMRI Signals

In contrast to the venus BOLD signal, for the CBV signal fluctuation, the arteriole-dominated CBV-signal results from vasomotor fluctuations in vessel diameter. The vasomotion signal shows ultra-slow oscillation with a broader frequency band centered at 0.1 Hz in the anesthetized rat brain (Mayhew et al., 1996; Kleinfeld et al., 1998) and 0.1 Hz in awake mice (Drew et al., 2010). Although in the present study arteriole CBV signal fluctuations were detected at a frequency band of <0.04 Hz in α-chloralose anesthetized rats, it is likely that this hemodynamic signal corresponds to vasomotion. Further to this point, beyond the neuronal effects of anesthetics (Brown et al., 2011; Mateo et al., 2017), anesthetics may directly affect vasomotion and directly contribute to the temporal dynamic patterns detected by fMRI in anesthetized animals (Colantuoni et al., 1984; Hundley et al., 1988). In addition, future studies will compare the arteriole-specific fMRI signal fluctuation in rat under anesthesia and wakefulness to specify the dynamic patterns driven by vasomotion. Lastly, our result is also consistent with the "bagpipe" model of active arteriole dilation with increased neuronal activity, where arteriole dynamics dominate both spontaneous and evoked blood volume changes in the brain (Drew et al., 2011). Following the net increase of the arteriole blood reservoir, venules drain the blood with a delayed passive dilation, which is consistent with undershoot of the evoked BOLD fMRI signal (Mandeville et al., 1999).

The ultra-slow passive venule dilation was detected by single-vessel CBV-bSSFP fMRI when iron oxide particles were delivered at a lower than normal dosage so that the venule fMRI signal was not completely dampened due to shortened T2* decay (Figure S5). This observation also explains the small number of venules highlighted by the arteriole-seed-based CBV correlation maps (Figure 2C), which showed much longer lag time than arterioles when analyzing the simultaneously acquired calcium ultra-slow oscillation signal via cross-correlation (Figure S5). All told, single-vessel bSSFP-fMRI detects distinct spatial and temporal patterns of vessel-specific dynamic connectivity in the anesthetized rat brain.

Correlates of Neuronal [Ca^{2+}] and Single-Vessel fMRI

A key observation was the correlation of ultra-slow calcium oscillation with single-vessel fMRI signal fluctuation. Prior combined fMRI and electrophysiological studies show that the resting-state BOLD signal correlates with neuronal activity oscillation (He et al., 2008; Shmuel and Leopold, 2008; Schölvinck et al., 2010; Pan et al., 2013). The present study extends the spatial resolution of resting-state fMRI down to single vessels. The coherence of the ultra-slow oscillations from both intracellular [Ca^{2+}] and vessel-specific fMRI signals demonstrates a potential link of the two events, with the calcium event leading the vascular fluctuation (Figures 4E and 4L). In particular, the BOLD signal from individual venules and the CBV-weighted signal detected primarily from arterioles showed varied lag times, ranging from 0.5 to 6 s, relative to the calcium signal (Figures 4G and 4N).

Previous studies reported only long, i.e., 5 to 6 s, lag times by cross-correlation of the change in γ-band power and the resting-state BOLD signal (Schölvinck et al., 2010). This long lag time could be caused by signal fluctuations in large voxels, with primary weighting on surface draining veins. In the present study, the fMRI signal from draining veins also showed longer lag time, which is consistent with the lag time between the calcium and hemoglobin signal oscillation ($\sim$0.1 Hz) detected from the cortical surface (Du et al., 2014). In contrast to surface draining veins, penetrating vessels at the deep cortical layers showed shorter lag times of 1.8 ± 0.2 s for the arteriole CBV signal and 2.3 ± 0.2 s for the venule BOLD signal (Figure 4), which is in coincordance with the signaling order of arteriole dilation followed by oxygen saturation changes in venules for neurovascular coupling (Devor et al., 2003; Iadecola, 2004).

The arterio-venous (A-V) transit time of the resting-state hemodynamic signal was calculated based on the cross-correlation lag times of the BOLD and CBV-weighted signals to the simultaneously recorded calcium signal (Figure S10 and Table S2). The resting-state A-V transit time of 0.61 s at the deep cortical layers is slighter shorter than the transit time of 0.8–1.2 s, calculated by the time to half-maximal, $t_{1/2}$, from surface arterioles to venules (Hutchinson et al., 2006). This further supports the vessel-specific hemodynamic signal propagation. Also noteworthy is that the variability of the measured resting-state transit time is relatively higher than that of the evoked A-V hemodynamic transit time (Yu et al., 2016) (Figure S10), indicating a more heterogeneous hemodynamic coupling during the resting state. Lastly, cortical calcium waves have been observed in the newborn and adult rodent brain (Adelsberger et al., 2005; Ma et al., 2016) and can propagate through the cortex at a fast speed (Stroh et al., 2013). It will be interesting to determine whether these drive propagating vascular events.

Single-Vessel Human Maps

Vascular dynamic network connectivity was directly mapped in awake human subjects to demonstrate the translational potential of single-vessel fMRI mapping. The vessel-specific ultra-slow oscillation shares a similar frequency range to that of the long-distance functional nodes detected by conventional resting-state fMRI, as well as the spontaneous oscillation of the cerebral hemodynamic signal detected by near-infrared spectroscopy (Obrig et al., 2000). In addition, the smoothed single-vessel correlation maps represented similar functional connectivity maps in the visual area as detected by the conventional resting-state fMRI (Smith et al., 2009) (Figures 7K and 7L). Together with the rat data that show highly correlated calcium and single-vessel fMRI signal fluctuation, the vascular dynamic network connectivity could represent the hemodynamic vascular correlation coupled to neuronal signal oscillation in both anesthetized and awake conditions. Interestingly, a recent resting-state fMRI study showed that the connectivity strength of a given voxel among the "default mode" and other networks is inversely proportional to its vascular volume fraction (Tak et al., 2015). This observation indicates that functional connectivity of long-range nodes in the brain may be driven independently of the vascular-specific hemodynamic fluctuation. Given the highly correlated calcium signal to the hemodynamic signal fluctuation, one possible explanation for this discrepancy is that vascular dynamic network connectivity represents the whole brain state fluctuation with less region specificity (Chang et al., 2016), but the functional connectivity may specify the network pattern of long-distance functional nodes (Biswal et al., 1995; Smith et al., 2009). Alternatively, because the vascular volume fraction was calculated from the largest extracerebral vessels detected by MRI images, it is also possible that the reduced connectivity may be caused by the low SNR of voxels occupied by these extracerebral vessels.

Given the cerebral folds and fissures of the human brain, single-vessel EPI-fMRI mapping mainly detects the central pial veins through the sulci with diameters of a few hundred micrometers based on the T2*-weighted partial volume effect. Single-vessel fMRI with 9.4T at high spatial resolution. i.e., 500 × 500 × 800 μm^3, showed the correlation patterns of the intracortical penetrating veins in the human brain (Duvernoy et al., 1981) (Figure 8). In contrast to studies focusing on excluding the venous BOLD signal to improve spatial specificity for brain function and connectivity mapping (Barth and Norris, 2007; Curtis et al., 2014), this work specifies the vascular network connectivity in gray matter of the human brain with the potential clinical application of illustrating hemodynamic features of vascular dementia (O'Brien et al., 2003; Iadecola, 2013). Specifically, the neural correlates of the vascular dynamic network connectivity detected in the rodent brain display great potential for clinical applications such as the diagnosis of cognitive impairments in patients with cerebral small vessel diseases or degenerative diseases such as Alzheimer's disease (Schaefer et al., 2014). The ability to specify the direct linkage of vascular pathology to dysfunction of the neurovascular network remains elusive (Stevens et al., 2014). The ability to map the hemodynamic origin of the BOLD signal from anatomically distinguishable vessels in human gray matter provides a key step to link vascular biomarkers, e.g., microbleeds (Poels et al., 2012) or cortical microinfarcts (van Veluw et al., 2013; van Rooden et al., 2014), with dynamic indicators in patients with small vessel or Alzheimer's disease.

Caveats Going Forward

We developed the single-vessel fMRI resting-state mapping scheme to characterize the spatial and temporal hemodynamic signals in arteriolar and venous networks, concurrent with photometric calcium recording. The high field MRI scanner, 14T for animals and 9.4T for humans, achieves sufficient SNR and high BOLD contrast for high-resolution fMRI imaging. A redesign of the radio frequency detection coil will be needed to extend the single-vessel fMRI method to broader application with lower magnetic field scanners. Toward this goal, a super-conducting coil has been developed to boost the SNR of MRI images (Ratering et al., 2008). Also, instead of the current 32- or 64-channel coils for human brain imaging, region-specific array coils can be developed to cover focal cortical areas with optimized geometry to increase the SNR. This step will help further resolve individual intracortical vessels in gray matter of normal human subjects as well as patients with neurovascular dysfunction due to vascular dementia.

STAR★METHODS

Detailed methods are provided in the online version of this paper and include the following:

- KEY RESOURCES TABLE
- CONTACT FOR REAGENT AND RESOURCE SHARING
- EXPERIMENTAL MODELS AND SUBJECT DETAILS
    - ○ Animals
    - ○ Human Subjects
- METHODS DETAILS
    - ○ Animal experiments
    - ○ MRI image acquisition from rats (14.1T)
    - ○ MRI image acquisition from humans (3 T)
    - ○ MRI image acquisition from humans (9.4 T)
    - ○ Data processing
    - ○ Immunohistochemistry
- QUANTIFICATION AND STATISTICAL ANALYSIS

SUPPLEMENTAL INFORMATION

Supplemental Information includes ten figures, three tables, and five movies and can be found with this article online at https://doi.org/10.1016/j.neuron.2018.01.025.

ACKNOWLEDGMENTS

This research was supported by Germany Research Foundation (DFG) SPP-1655 and internal funding from Max Planck Society for X.Y. and NIH grants R35NS097265 for D.K. and NIMH BRAIN grant R01MH111438 for D.K. and B.R.R. We thank Dr. H. Merkle and Dr. K. Buckenmaier for technical support, Ms. H. Schulz and Ms. S. Fischer for animal maintenance support, the AFNI team for the software support, and Dr. L. Looger and the Janelia Research Campus of HHMI for kindly providing viral vectors.

AUTHOR CONTRIBUTIONS

X.Y., D.K., and B.R.R. designed the research, Y.H., X.Y., M.W., and X.C. performed animal experiments, Y.H., X.Y., and R.P. acquired data, X.Y. supervised the research, Y.H. analyzed data, K.S., R.P., J.R.P., and M.W. provided key technical support, and X.Y., D.K., and Y.H. wrote the manuscript.

DECLARATION OF INTERESTS

The authors declare no competing interests.

Received: June 26, 2017
Revised: November 14, 2017
Accepted: January 10, 2018
Published: February 1, 2018

REFERENCES

Adelsberger, H., Garaschuk, O., and Konnerth, A. (2005). Cortical calcium waves in resting newborn mice. Nat. Neurosci. *8*, 988–990.

Aydin, F., Rosenblum, W.I., and Povlishock, J.T. (1991). Myoendothelial junctions in human brain arterioles. Stroke *22*, 1592–1597.

Barth, M., and Norris, D.G. (2007). Very high-resolution three-dimensional functional MRI of the human visual cortex with elimination of large venous vessels. NMR Biomed. *20*, 477–484.

Bell, A.J., and Sejnowski, T.J. (1995). An information-maximization approach to blind separation and blind deconvolution. Neural Comput. *7*, 1129–1159.

Bieri, O., and Scheffler, K. (2007). Effect of diffusion in inhomogeneous magnetic fields on balanced steady-state free precession. NMR Biomed. *20*, 1–10.

Biswal, B., Yetkin, F.Z., Haughton, V.M., and Hyde, J.S. (1995). Functional connectivity in the motor cortex of resting human brain using echo-planar MRI. Magn. Reson. Med. *34*, 537–541.

Blinder, P., Tsai, P.S., Kaufhold, J.P., Knutsen, P.M., Suhl, H., and Kleinfeld, D. (2013). The cortical angiome: an interconnected vascular network with noncolumnar patterns of blood flow. Nat. Neurosci. *16*, 889–897.

Blockley, N.P., Jiang, L., Gardener, A.G., Ludman, C.N., Francis, S.T., and Gowland, P.A. (2008). Field strength dependence of R1 and R2* relaxivities of human whole blood to ProHance, Vasovist, and deoxyhemoglobin. Magn. Reson. Med. *60*, 1313–1320.

Brown, E.N., Purdon, P.L., and Van Dort, C.J. (2011). General anesthesia and altered states of arousal: a systems neuroscience analysis. Annu. Rev. Neurosci. *34*, 601–628.

Budde, J., Shajan, G., Zaitsev, M., Scheffler, K., and Pohmann, R. (2014). Functional MRI in human subjects with gradient-echo and spin-echo EPI at 9.4 T. Magn. Reson. Med. *71*, 209–218.

Buxton, R.B., Wong, E.C., and Frank, L.R. (1998). Dynamics of blood flow and oxygenation changes during brain activation: the balloon model. Magn. Reson. Med. *39*, 855–864.

Chan, A.W., Mohajerani, M.H., LeDue, J.M., Wang, Y.T., and Murphy, T.H. (2015). Mesoscale infraslow spontaneous membrane potential fluctuations recapitulate high-frequency activity cortical motifs. Nat. Commun. *6*, 7738.

Chang, C., Leopold, D.A., Schölvinck, M.L., Mandelkow, H., Picchioni, D., Liu, X., Ye, F.Q., Turchi, J.N., and Duyn, J.H. (2016). Tracking brain arousal fluctuations with fMRI. Proc. Natl. Acad. Sci. USA *113*, 4518–4523.

Chen, T.W., Wardill, T.J., Sun, Y., Pulver, S.R., Renninger, S.L., Baohan, A., Schreiter, E.R., Kerr, R.A., Orger, M.B., Jayaraman, V., et al. (2013). Ultrasensitive fluorescent proteins for imaging neuronal activity. Nature *499*, 295–300.

Colantuoni, A., Bertuglia, S., and Intaglietta, M. (1984). Effects of anesthesia on the spontaneous activity of the microvasculature. Int. J. Microcirc. Clin. Exp. *3*, 13–28.

Cox, R.W. (1996). AFNI: software for analysis and visualization of functional magnetic resonance neuroimages. Comput. Biomed. Res. *29*, 162–173.

Curtis, A.T., Hutchison, R.M., and Menon, R.S. (2014). Phase based venous suppression in resting-state BOLD GE-fMRI. Neuroimage *100*, 51–59.

Delorme, A., and Makeig, S. (2004). EEGLAB: an open source toolbox for analysis of single-trial EEG dynamics including independent component analysis. J. Neurosci. Methods *134*, 9–21.

Devor, A., Dunn, A.K., Andermann, M.L., Ulbert, I., Boas, D.A., and Dale, A.M. (2003). Coupling of total hemoglobin concentration, oxygenation, and neural activity in rat somatosensory cortex. Neuron *39*, 353–359.

Drew, P.J., Duyn, J.H., Golanov, E., and Kleinfeld, D. (2008). Finding coherence in spontaneous oscillations. Nat. Neurosci. *11*, 991–993.

Drew, P.J., Shih, A.Y., Driscoll, J.D., Knutsen, P.M., Blinder, P., Davalos, D., Akassoglou, K., Tsai, P.S., and Kleinfeld, D. (2010). Chronic optical access through a polished and reinforced thinned skull. Nat. Methods *7*, 981–984.

Drew, P.J., Shih, A.Y., and Kleinfeld, D. (2011). Fluctuating and sensory-induced vasodynamics in rodent cortex extend arteriole capacity. Proc. Natl. Acad. Sci. USA *108*, 8473–8478.

Du, C., Volkow, N.D., Koretsky, A.P., and Pan, Y. (2014). Low-frequency calcium oscillations accompany deoxyhemoglobin oscillations in rat somatosensory cortex. Proc. Natl. Acad. Sci. USA *111*, E4677–E4686.

Duvernoy, H.M., Delon, S., and Vannson, J.L. (1981). Cortical blood vessels of the human brain. Brain Res. Bull. *7*, 519–579.

Fox, M.D., and Raichle, M.E. (2007). Spontaneous fluctuations in brain activity observed with functional magnetic resonance imaging. Nat. Rev. Neurosci. *8*, 700–711.

Glover, G.H., Li, T.Q., and Ress, D. (2000). Image-based method for retrospective correction of physiological motion effects in fMRI: RETROICOR. Magn. Reson. Med. *44*, 162–167.

He, B.J., Snyder, A.Z., Zempel, J.M., Smyth, M.D., and Raichle, M.E. (2008). Electrophysiological correlates of the brain's intrinsic large-scale functional architecture. Proc. Natl. Acad. Sci. USA *105*, 16039–16044.

Hirsch, S., Reichold, J., Schneider, M., Székely, G., and Weber, B. (2012). Topology and hemodynamics of the cortical cerebrovascular system. J. Cereb. Blood Flow Metab. *32*, 952–967.

Hu, X., Le, T.H., Parrish, T., and Erhard, P. (1995). Retrospective estimation and correction of physiological fluctuation in functional MRI. Magn. Reson. Med. *34*, 201–212.

Hundley, W.G., Renaldo, G.J., Levasseur, J.E., and Kontos, H.A. (1988). Vasomotion in cerebral microcirculation of awake rabbits. Am. J. Physiol. *254*, H67–H71.

Hutchinson, E.B., Stefanovic, B., Koretsky, A.P., and Silva, A.C. (2006). Spatial flow-volume dissociation of the cerebral microcirculatory response to mild hypercapnia. Neuroimage *32*, 520–530.

Iadecola, C. (2004). Neurovascular regulation in the normal brain and in Alzheimer's disease. Nat. Rev. Neurosci. *5*, 347–360.

Iadecola, C. (2013). The pathobiology of vascular dementia. Neuron *80*, 844–866.

Intaglietta, M. (1990). Vasomotion and flowmotion: physiological mechanisms and clinical evidence. Vasc. Med. Rev. *1*, 101–112.

Kim, S.G., Hendrich, K., Hu, X., Merkle, H., and Uğurbil, K. (1994). Potential pitfalls of functional MRI using conventional gradient-recalled echo techniques. NMR Biomed. *7*, 69–74.

Kleinfeld, D., Mitra, P.P., Helmchen, F., and Denk, W. (1998). Fluctuations and stimulus-induced changes in blood flow observed in individual capillaries in layers 2 through 4 of rat neocortex. Proc. Natl. Acad. Sci. USA *95*, 15741–15746.

Lee, S.P., Silva, A.C., Ugurbil, K., and Kim, S.G. (1999). Diffusion-weighted spin-echo fMRI at 9.4 T: microvascular/tissue contribution to BOLD signal changes. Magn. Reson. Med. *42*, 919–928.

Logothetis, N.K., Pauls, J., Augath, M., Trinath, T., and Oeltermann, A. (2001). Neurophysiological investigation of the basis of the fMRI signal. Nature *412*, 150–157.

Longden, T.A., Dabertrand, F., Koide, M., Gonzales, A.L., Tykocki, N.R., Brayden, J.E., Hill-Eubanks, D., and Nelson, M.T. (2017). Capillary K+-sensing initiates retrograde hyperpolarization to increase local cerebral blood flow. Nat. Neurosci. *20*, 717–726.

Ma, Y., Shaik, M.A., Kozberg, M.G., Kim, S.H., Portes, J.P., Timerman, D., and Hillman, E.M. (2016). Resting-state hemodynamics are spatiotemporally coupled to synchronized and symmetric neural activity in excitatory neurons. Proc. Natl. Acad. Sci. USA *113*, E8463–E8471.

Mandeville, J.B., Marota, J.J., Kosofsky, B.E., Keltner, J.R., Weissleder, R., Rosen, B.R., and Weisskoff, R.M. (1998). Dynamic functional imaging of relative cerebral blood volume during rat forepaw stimulation. Magn. Reson. Med. *39*, 615–624.

Mandeville, J.B., Marota, J.J., Ayata, C., Zaharchuk, G., Moskowitz, M.A., Rosen, B.R., and Weisskoff, R.M. (1999). Evidence of a cerebrovascular postarteriole windkessel with delayed compliance. J. Cereb. Blood Flow Metab. *19*, 679–689.

Mansfield, P., Maudsley, A.A., and Baines, T. (1976). Fast Scan Proton Density Imaging by Nmr. J. Phys. E Sci. Instrum. *9*, 271–278.

Mateo, C., Knutsen, P.M., Tsai, P.S., Shih, A.Y., and Kleinfeld, D. (2017). Entrainment of arteriole vasomotor fluctuations by neural activity is a basis of blood-oxygenation-level-dependent "resting-state" connectivity. Neuron *96*, 936–948.e3.

Mayhew, J.E., Askew, S., Zheng, Y., Porrill, J., Westby, G.W., Redgrave, P., Rector, D.M., and Harper, R.M. (1996). Cerebral vasomotion: a 0.1-Hz oscillation in reflected light imaging of neural activity. Neuroimage *4*, 183–193.

McKeown, M.J., Hansen, L.K., and Sejnowsk, T.J. (2003). Independent component analysis of functional MRI: what is signal and what is noise? Curr. Opin. Neurobiol. *13*, 620–629.

Menon, R.S., Ogawa, S., Tank, D.W., and Uğurbil, K. (1993). Tesla gradient recalled echo characteristics of photic stimulation-induced signal changes in the human primary visual cortex. Magn. Reson. Med. *30*, 380–386.

Mitra, P.P., Ogawa, S., Hu, X., and Uğurbil, K. (1997). The nature of spatiotemporal changes in cerebral hemodynamics as manifested in functional magnetic resonance imaging. Magn. Reson. Med. *37*, 511–518.

Moon, C.H., Fukuda, M., and Kim, S.G. (2013). Spatiotemporal characteristics and vascular sources of neural-specific and -nonspecific fMRI signals at submillimeter columnar resolution. Neuroimage *64*, 91–103.

Murphy, K., Birn, R.M., and Bandettini, P.A. (2013). Resting-state fMRI confounds and cleanup. Neuroimage *80*, 349–359.

O'Brien, J.T., Erkinjuntti, T., Reisberg, B., Roman, G., Sawada, T., Pantoni, L., Bowler, J.V., Ballard, C., DeCarli, C., Gorelick, P.B., et al. (2003). Vascular cognitive impairment. Lancet Neurol. *2*, 89–98.

Obrig, H., Neufang, M., Wenzel, R., Kohl, M., Steinbrink, J., Einhäupl, K., and Villringer, A. (2000). Spontaneous low frequency oscillations of cerebral hemodynamics and metabolism in human adults. Neuroimage *12*, 623–639.

Pan, W.J., Thompson, G.J., Magnuson, M.E., Jaeger, D., and Keilholz, S. (2013). Infraslow LFP correlates to resting-state fMRI BOLD signals. Neuroimage *74*, 288–297.

Poels, M.M., Ikram, M.A., van der Lugt, A., Hofman, A., Niessen, W.J., Krestin, G.P., Breteler, M.M., and Vernooij, M.W. (2012). Cerebral microbleeds are associated with worse cognitive function: the Rotterdam Scan Study. Neurology *78*, 326–333.

Poplawsky, A.J., Fukuda, M., Kang, B.M., Kim, J.H., Suh, M., and Kim, S.G. (2017). Dominance of layer-specific microvessel dilation in contrast-enhanced high-resolution fMRI: Comparison between hemodynamic spread and vascular architecture with CLARITY. NeuroImage. Published online August 16, 2017. https://doi.org/10.1016/j.neuroimage.2017.1008.1046.

Ratering, D., Baltes, C., Nordmeyer-Massner, J., Marek, D., and Rudin, M. (2008). Performance of a 200-MHz cryogenic RF probe designed for MRI and MRS of the murine brain. Magn. Reson. Med. *59*, 1440–1447.

Schaefer, A., Quinque, E.M., Kipping, J.A., Arélin, K., Roggenhofer, E., Frisch, S., Villringer, A., Mueller, K., and Schroeter, M.L. (2014). Early small vessel disease affects frontoparietal and cerebellar hubs in close correlation with clinical symptoms–a resting-state fMRI study. J. Cereb. Blood Flow Metab. *34*, 1091–1095.

Scheffler, K., and Ehses, P. (2016). High-resolution mapping of neuronal activation with balanced SSFP at 9.4 tesla. Magn. Reson. Med. *76*, 163–171.

Scheffler, K., and Lehnhardt, S. (2003). Principles and applications of balanced SSFP techniques. Eur. Radiol. *13*, 2409–2418.

Schölvinck, M.L., Maier, A., Ye, F.Q., Duyn, J.H., and Leopold, D.A. (2010). Neural basis of global resting-state fMRI activity. Proc. Natl. Acad. Sci. USA *107*, 10238–10243.

Schulz, K., Sydekum, E., Krueppel, R., Engelbrecht, C.J., Schlegel, F., Schröter, A., Rudin, M., and Helmchen, F. (2012). Simultaneous BOLD fMRI and fiber-optic calcium recording in rat neocortex. Nat. Methods *9*, 597–602.

Segal, S.S., and Duling, B.R. (1989). Conduction of vasomotor responses in arterioles: a role for cell-to-cell coupling? Am. J. Physiol. *256*, H838–H845.

Shajan, G., Kozlov, M., Hoffmann, J., Turner, R., Scheffler, K., and Pohmann, R. (2014). A 16-channel dual-row transmit array in combination with a 31-element receive array for human brain imaging at 9.4 T. Magn. Reson. Med. *71*, 870–879.

Shmuel, A., and Leopold, D.A. (2008). Neuronal correlates of spontaneous fluctuations in fMRI signals in monkey visual cortex: Implications for functional connectivity at rest. Hum. Brain Mapp. *29*, 751–761.

Silva, A.C., and Koretsky, A.P. (2002). Laminar specificity of functional MRI onset times during somatosensory stimulation in rat. Proc. Natl. Acad. Sci. USA *99*, 15182–15187.

Silva, A.C., Koretsky, A.P., and Duyn, J.H. (2007). Functional MRI impulse response for BOLD and CBV contrast in rat somatosensory cortex. Magn. Reson. Med. *57*, 1110–1118.

Smith, S.M., Fox, P.T., Miller, K.L., Glahn, D.C., Fox, P.M., Mackay, C.E., Filippini, N., Watkins, K.E., Toro, R., Laird, A.R., and Beckmann, C.F. (2009). Correspondence of the brain's functional architecture during activation and rest. Proc. Natl. Acad. Sci. USA *106*, 13040–13045.

Stevens, R.D., Hannawi, Y., and Sair, H. (2014). Small vessel disease and the resting functional architecture of the brain. J. Cereb. Blood Flow Metab. *34*, 1089–1090.

Stroh, A., Adelsberger, H., Groh, A., Rühlmann, C., Fischer, S., Schierloh, A., Deisseroth, K., and Konnerth, A. (2013). Making waves: initiation and propagation of corticothalamic Ca2+ waves in vivo. Neuron *77*, 1136–1150.

Tak, S., Polimeni, J.R., Wang, D.J., Yan, L., and Chen, J.J. (2015). Associations of resting-state fMRI functional connectivity with flow-BOLD coupling and regional vasculature. Brain Connect. *5*, 137–146.

van Rooden, S., Goos, J.D., van Opstal, A.M., Versluis, M.J., Webb, A.G., Blauw, G.J., van der Flier, W.M., Scheltens, P., Barkhof, F., van Buchem, M.A., and van der Grond, J. (2014). Increased number of microinfarcts in Alzheimer disease at 7-T MR imaging. Radiology *270*, 205–211.

van Veluw, S.J., Zwanenburg, J.J., Engelen-Lee, J., Spliet, W.G., Hendrikse, J., Luijten, P.R., and Biessels, G.J. (2013). In vivo detection of cerebral cortical microinfarcts with high-resolution 7T MRI. J. Cereb. Blood Flow Metab. *33*, 322–329.

Wang, L., Saalmann, Y.B., Pinsk, M.A., Arcaro, M.J., and Kastner, S. (2012). Electrophysiological low-frequency coherence and cross-frequency coupling contribute to BOLD connectivity. Neuron *76*, 1010–1020.

Yu, X., Wang, S.M., Chen, D.Y., Dodd, S., Goloshevsky, A., and Koretsky, A.P. (2010). 3D mapping of somatotopic reorganization with small animal functional MRI. NeuroImage *49*, 1667–1676.

Yu, X., Glen, D., Wang, S., Dodd, S., Hirano, Y., Saad, Z., Reynolds, R., Silva, A.C., and Koretsky, A.P. (2012). Direct imaging of macrovascular and microvascular contributions to BOLD fMRI in layers IV-V of the rat whisker-barrel cortex. Neuroimage *59*, 1451–1460.

Yu, X., Qian, C., Chen, D.Y., Dodd, S.J., and Koretsky, A.P. (2014). Deciphering laminar-specific neural inputs with line-scanning fMRI. Nat. Methods *11*, 55–58.

Yu, X., He, Y., Wang, M., Merkle, H., Dodd, S.J., Silva, A.C., and Koretsky, A.P. (2016). Sensory and optogenetically driven single-vessel fMRI. Nat. Methods *13*, 337–340.

Zhu, D.C., Tarumi, T., Khan, M.A., and Zhang, R. (2015). Vascular coupling in resting-state fMRI: evidence from multiple modalities. J. Cereb. Blood Flow Metab. *35*, 1910–1920.

Please cite this article in press as: He et al., Ultra-Slow Single-Vessel BOLD and CBV-Based fMRI Spatiotemporal Dynamics and Their Correlation with Neuronal Intracellular Calcium Signals, Neuron (2018), https://doi.org/10.1016/j.neuron.2018.01.025

STAR★METHODS

KEY RESOURCES TABLE

REAGENT or RESOURCE	SOURCE	IDENTIFIER
Antibodies		
Anti NeuN antibody	Merck	RRID: AB_2298772, Cat# MAB377
Secondary antibody (Goat Anti-Mouse)	Abcam	RRID: AB_10680176, Cat# ab97035
Bacterial and Virus Strains		
AAV5.Syn.GCaMP6f.WPRE.SV40	PENN Vector Core	Cat# AV-5-PV2822
Chemicals, Peptides, and Recombinant Proteins		
Isoflurane	CP-Pharma	Cat# 1214
Iron oxide nanoparticle: Molday ION	BioPhysics Assay Laboratory (BioPAL)	Cat# CL-30Q02-2
α-chloralose	Sigma-Aldrich	Cat# C0128-25G;RRID
pancuronium bromide	Inresa Arzneimittel	Cat# 34409.00.00
VECTASHIELD Antifade Mounting Medium with DAPI	Vector Laboratories	RRID: AB_2336790, Cat# H-1200
Phosphate Buffered Saline (PBS)	GIBCO	Cat# 10010-023
Experimental Models: Organisms/Strains		
Rat: Sprague Dawley rat	Charles River Laboratories	N/A
Software and Algorithms		
MATLAB	MathWorks	RRID: SCR_001622, https://www.mathworks.com/
AFNI	Cox, 1996	RRID: SCR_005927, http://afni.nimh.nih.gov
EEGLAB	Delorme and Makeig, 2004	RRID: SCR_007292, https://sccn.ucsd.edu/eeglab/index.html
Group ICA Of fMRI Toolbox (GIFT)	Medical Image Analysis Lab	RRID: SCR_001953, GIFT 4.0, http://mialab.mrn.org/software/gift/
Excel 2013	Microsoft	https://products.office.com/en-us/excel
Adobe Illustrator CC	Adobe	RRID: SCR_010279, http://www.adobe.com/products/illustrator.html
Other		
Biopac MP 150 System	Biopac	RRID: SCR_014829
AcqKnowledge Software	Biopac	RRID: SCR_014279, https://www.biopac.com/product/acqknowledge-software/
Master-9	A.M.P.I	N/A
Nanoliter Injector	World Precision Instruments	Cat# NANOFIL
Laser (473 nm)	CNI	Cat# MBL-III
Dichroic mirrors	AHF Analysentechnik	Cat# F48-487
Fiber launch	Thorlabs	Cat# MBT613D/M
Optical fiber	Thorlabs	Cat# FT-200-EMT
Optical power meter	Thorlabs	Cat# PM20A
Optical filter	AHF Analysentechnik	Cat# F37-516
Silicon photomultiplier	SensL	Cat# MiniSM-10035-X08
Voltage amplifier	Femto	Cat# DHPVA-100
Tungsten Microelectrode	FHC	Cat# UEWSDDSMCN1M

CONTACT FOR REAGENT AND RESOURCE SHARING

Further information and requests for resources and reagents should be directed to and will be fulfilled by the Lead Contact, Dr. Xin Yu (xin.yu@tuebingen.mpg.de).

Please cite this article in press as: He et al., Ultra-Slow Single-Vessel BOLD and CBV-Based fMRI Spatiotemporal Dynamics and Their Correlation with Neuronal Intracellular Calcium Signals, Neuron (2018), https://doi.org/10.1016/j.neuron.2018.01.025

EXPERIMENTAL MODELS AND SUBJECT DETAILS

Animals

All experimental procedures were approved by the Animal Protection Committee of Tuebingen (Regierungspräsidium Tuebingen) and performed in accordance with the guidelines. Thirty-five male Sprague-Dawley rats were employed in all experiments. Littermates of the male rats (age: 2 - 3 months) were randomly assigned to experimental groups. Both evoked and resting-state bSSFP-fMRI data with A-V maps were acquired from five of nine rats under alpha-chloralose anesthesia, of which both BOLD and CBV signals were acquired under the same A-V map. To verify the effect of different drugs on vascular dynamic network connectivity, five rats were utilized for resting-state BOLD bSSFP-fMRI data under isoflurane anesthesia. In addition, the rats (BOLD: seven of eight, CBV: four of eight) with calcium indicator were employed for the statistics of simultaneous BOLD/CBV rsfMRI and fiber-optic calcium recording studies. Some rats were excluded from statistical analysis due to the large SSFP image distortion introduced by the optical fiber insertion. In addition, seven rats were employed to acquire simultaneous local field potential (LFP) and calcium signal.

Human Subjects

All human subject experiments follow the guidelines of the regulation procedure in the Max Planck Institute, and the informed consents were obtained from all human volunteers. For 3T MRI image acquisition, six healthy adult subjects (female, n = 3; male, n = 3; age: 20 - 35 years) were employed to obtain rsfMRI. For 9.4T MRI image acquisition, six healthy adult subjects (female, n = 2; male, n = 4; age: 20 - 35 years) were examined with Echo-planar imaging (EPI) sequence.

METHODS DETAILS

Animal experiments

Animal preparation

All procedures were described in a previous study (Yu et al., 2010). Rats were initially anesthetized with isoflurane (5% induction, 1.5% maintenance). Each rat was orally intubated and placed on a mechanical ventilator (SAR-830/AP, CWE). Plastic catheters were inserted into the right femoral artery and vein to allow monitoring of arterial blood gasses and administration of anesthetics. Two different anesthesia treatments were delivered during fMRI (Table S3). For alpha-chloralose anesthesia, after surgery, each rat was given an intravenous bolus of α-chloralose (60 mg/kg) and isoflurane was discontinued. Anesthesia was maintained with two constant infusion rates of α-chloralose (15 and 26.5 mg/kg/hr) in combination with pancuronium bromide (4 mg/kg/hr) to reduce motion artifacts. For isoflurane anesthesia, the ventilator maintained the rats breathing under isoflurane 1.2% in the magnet. The rats' rectal temperature was maintained at around 37°C. To prevent head motion, rats were secured in a head holder with a bite bar. All relevant physiological parameters (end-tidal CO2, rectal temperature, heart rate, and arterial blood pressure) were continuously monitored during imaging (Figure S3, blood pressure and heart rate). The pulse sequence–based trigger and stimulation control were established using the BioPac system (Goleta, USA) and Master-9 A.M.P.I system (Jerusalem, Israel).

Viral vector injection and optical fiber implantation

The viral vectors (AV-1-PV2822 AAV5.Syn.GCaMP6f.WPRE.SV40) were procured from University of Pennsylvania Vector Core (Chen et al., 2013). Viral vectors were injected in the barrel cortex (BC) or the forepaw region of the primary somatosensory cortex (S1FL) of 3 to 4 week old rats. For the stereotactic injection procedure, rats were initially anesthetized with isoflurane. After exposing the skull, a small bur hole was drilled. A nanoliter injector (WPI, FL) was used to place a 35-gauge needle at the proper coordinates in the stereotactic frame. Injections were performed slowly over 5–6 min and the needle was slowly removed after being kept in the injection site for 10 min after finishing the injection. The injection sites of BC were as follows with stereotactic coordinates: AP = -2.35 mm; ML: 4.8 mm; DV = 2; injections each 400 nL at 1.2 mm and 0.7 mm. The injection sites of S1FL were as follows: AP = 0.2 mm; ML = 3.7 mm; DV = 2 injections each 400 nL at 1.2 mm and 0.7 mm. After 6-8 weeks of viral expression, a 200-μm optical fiber (7 m length) was inserted through the burr holes on the skull into the BC (stereotactic coordinates: AP = -2.7 mm; ML = 5.1 mm; DV = 1.3 mm; tilt, 4°) or S1FL (AP = 0.2 mm; ML = 4 mm; DV = 1.3 mm). The optical fiber was fixed on the skull with glue. Then, the skin was sutured to cover the glue with the optical fiber extending outside of the rat head.

Simultaneous rsfMRI and calcium recording

The optical setup for calcium signal recording was built up based on a previous study (Schulz et al., 2012; M.W., Y.H., T.J. Sejnowski, and X.Y., unpublished data). As shown in Figure S4A, a 473 nm laser (MBC-III, CNI) was set to deliver the fluorescent excitation light. The laser beam was first aligned by a reflection mirror to a correct angle better deflect off a dichroic beam-splitting mirror (BS R488: reflection 471 - 491 nm, >94%; transmission 500 - 1200 nm, >93%; AHF Analysentechnik), which was coupled into a multimode fiber (FT200EMT: NA = 0.48, 230 μm cladding diameter; Thorlabs) via amplifying lens (RMS4X; Thorlabs). Fluorescence excitation occurred in the vicinity of the fiber tip inside the MRI scanner and the emitted fluorescence light was collected and guided back to the optical setup through the same fiber. The emitted fluorescent signal from the fiber passed a lens, dichroic mirror, and an emission filter (Semrock Razoredge; 488 Long Pass; AHF Analysentechnik), and was finally focused by a tube lens (AC254-030-A1-ML; Thorlabs) onto a peltier-cooled silicon photomultiplier with transimpedance preamplifier (MiniSM-10035-X08; SensL). The signal from the photomultiplier was amplified by voltage amplifier (DHPVA-100; Femto) and acquired by the analog input module of a Biopac

Please cite this article in press as: He et al., Ultra-Slow Single-Vessel BOLD and CBV-Based fMRI Spatiotemporal Dynamics and Their Correlation with Neuronal Intracellular Calcium Signals, Neuron (2018), https://doi.org/10.1016/j.neuron.2018.01.025

MP 150 system (5-K sampling rate). Triggers from the MRI scanner were also recorded by the Biopac system and used to synchronize calcium to BOLD fMRI offline. Laser intensity was measured at the fiber tip for neuronal calcium (~5 uW) to avoid phototoxicity for long-term recording by optical power meters (PM20A; ThorLabs).

Simultaneous calcium with electrophysiology recording

The anesthetized rats were adapted in a stereotaxic device for *in vivo* recordings using similar anesthetics and surgical preparation to the fMRI experiments. Tungsten microelectrode (1 MΩ, ~100 μm, Tungsten, FHC) was bonded to an optical fiber with closely contacted fiber optic tip and electrode contacting point. The local field potential (LFP) was recorded through the EEG module of the Biopac system (gain factor, 5,000; band-pass filter, 0.02 - 100 Hz; sample rate, 5,000/s). In addition, calcium data and blood pressure were digitized and recorded with Biopac MP 150 system at a sampling rate of 5 kHz. The spectrogram of LFP was calculated through multi-taper spectral estimation. (Figure 6, and S7, 1 s sliding window with 0.1 s steps, 9 tapers)

MRI image acquisition from rats (14.1T)

All images from rats were acquired with a 14.1 T/26 cm horizontal bore magnet (Magnex) interfaced to an Avance III console (Bruker). A transceiver surface coil with a 6-mm diameter was used to acquire images.

bSSFP-fMRI

Balanced Steady-State Free Precession was implemented with the following parameters: TE, 3.9 ms; TR, 7.8 ms; flip angle (FA),12°; matrix, 96 × 128; FOV, 9.6 × 12.8 mm; slice thickness = 400 μm; in-plane resolution = 100 × 100 μm^2, resulting in one slice repetition time of 1 s. The block design was 2 s stimulation and 28 s inter-stimulus interval. The duration of each trial of rsfMRI was 15 min, and 2 - 5 trails of BOLD/CBV rsfMRI were acquired for each rat. CBV fMRI signals were acquired after intravenous injection of 15 - 20 mg of Fe/kg dextran-coated iron oxide (BioPAL, MA).

Single-vessel MGE imaging in rats

The imaging protocol was similar with our previous paper (Yu et al., 2016). To recognize individual arterioles and venules, we employed a 2D Multiple Gradient-Echo (MGE) sequence with the following parameters: TR = 50 ms; TE = 2.5, 5, 7.5, 10, 12.5 and 15 ms; flip angle = 40°; matrix = 192 × 192; in-plane resolution = 50 × 50 μm^2; slice thickness = 500 μm. We averaged the MGE images from the second echo to the fourth echo and created an arteriole-venule (A-V) map, where the venule voxels display as dark dots (blue marks) because of the fast T_2^* decay but arteriole voxels remain bright (red marks) owing to the in-flow effect (Figure 1A).

MRI image acquisition from humans (3 T)

All measurements were performed on a 3-T Siemens Prisma with a 20-channel receive head coil. Six healthy adult subjects (female, n = 3; male, n = 3; age: 20 - 35 years) were employed to obtain a BOLD signal using EPI with the following parameters: TR = 1,000 ms; TE = 29 ms; FA = 60°; matrix = 121 × 119; in-plane resolution = 840 μm x 840 μm; 9 slices with thicknesses of 1.5 mm. Parallel imaging (GRAPPA factor: 3) and partial Fourier (6/8) were employed to accelerate image acquisition. The visual stimulation consisted of a circular black and white checkerboard. For the resting state fMRI, the duration of each trial of rs-fMRI was 15 min with the eyes-closed condition. The Siemens physiologic Monitoring Unit (PMU) was used to monitor the respiration and pulse oximetry simultaneously. Both PMU physiological log files and EPI data contain time tags, which were utilized to synchronize the temporal profile for statistical analysis.

MRI image acquisition from humans (9.4 T)

All images were acquired with a 9.4-T MRI scanner (Siemens Healthcare, Erlangen, Germany) with a home-built 16-channel transmit/31-channel receive head coil (Shajan et al., 2014). All the imaging protocols follow those of the 3-T scanner but at a higher resolution. Six healthy subjects (female, n = 2; male, n = 4; age: 20 - 35 years) were examined with EPI sequence: TR = 1,000 ms; TE = 22 ms; FA = 50°; matrix = 300 × 300; in-plane resolution = 500 μm × 500 μm; 9 slices a thicknesses of 0.8 mm. Parallel imaging (GRAPPA factor: 4) and partial Fourier (5/8) were utilized to accelerate image acquisition.

Single-vessel MGE imaging in humans

We utilized a 2D MGE sequence with the following parameters: TR = 61 ms; TE = 5.99, 10.39, 14.79, 19.19, 23.59, 27.99, 32.39, 36.79, 41.19, 45.59 ms; flip angle = 60°; matrix = 896 × 896; in-plane resolution = 19 × 19 μm^2; slice thickness = 1,000 μm. An arteriole-venule (A-V) map was acquired by averaging of the MGE images from the second echo to the ninth echo (Figure 8A).

Data processing

All data processing was performed using Analysis of Functional NeuroImages (AFNI) software (Cox, 1996) and MATLAB. The relevant fMRI analysis source codes can be downloaded through https://www.afni.nimh.nih.gov/afni/. *A* detailed description of the processing procedure conducted is provided in a previous study (Yu et al., 2012). To register the single-vessel functional map with the A-V map, the tag-based registration method was applied, which carried out ten to twelve tags (venule voxels) of the averaged bSSFP fMRI images corresponding to those of the A-V map. No additional smoothing step was applied. For evoked fMRI analysis, images were normalized by scaling the baseline to 100. Linear regression analysis was applied to estimate the hemodynamic response function. The beta estimates were used to indicate the amplitude of the BOLD response in the beta maps.

Definition of the individual vessel

The individual vessel voxels in A-V map were identified by the following algorithm: the intensities of arteriole/artery voxels are higher than the mean signal intensities plus two times the standard deviation (s.d.) of the local area in a 5 × 5 kernel, while the intensities of venule/vein voxels are lower than the mean signal intensities minus two times the s.d. of local area, as shown in Figure 1A (Yu et al., 2016). The locations of individual vessel voxels defined in the A-V map were employed to extract the time courses from BOLD/CBV fMRI of individual vessels.

Resting state fMRI analysis

The preprocessing analysis was performed using a modified AFNI resting state fMRI processing protocol (afni_proc.py). The time courses of the vessel seed voxels were chosen for correlation analysis. The vessel voxels from both arteriole and venules were determined based on the A-V map. The detailed image processing procedure utilized was described previously (Yu et al., 2016). Then the 3dTcorr1D function in AFNI was employed to generate the correlation map. In addition, ICA analysis was also performed to characterize the vessel specific correlation maps with the Independent Component Analysis (ICA) Toolbox (GIFT 4.0, MIND Research Network). The ICA toolbox employed principal component analysis (PCA) to realign the data at a lower dimensionality (or reduced variance in a simplified dimensional space). ICA was utilized to generate ten independent components using Infomax algorithms, which specialize in the separation of super-Gaussian sources (Bell and Sejnowski, 1995). After the back reconstruction step, the spatial maps and time courses of components were scaled using Z-scores. Finally, a RETROICOR algorithm (Glover et al., 2000) was implemented to correct physiological motion effects (Figure S8).

Power spectrum analysis

Depending on data format, power spectrum analysis was performed in AFNI (image format) or MATLAB (text format). In AFNI, a 3dPeriodogram function was utilized to compute the power spectrum of time courses in all individual voxels. Then the averaged power spectral density was calculated in venule voxels or arteriole voxels, respectively (FFT length: 256, Figures S6B and S6D). In MATLAB, we employed Fast Fourier Transform (FFT) to calculate the power spectral density of the physiologic data (respiration/pulse oximetry) (Figure S8F) and calcium data (Figure S6F). The calcium signals under light/deep anesthesia were sampled at 1 Hz and calculated by Welch's power spectral density estimate method (FFT length: 256, the overlap: 50%).

Coherence analysis

Previously, coherence analysis was implemented to identify the functional connectivity between different brain areas (Drew et al., 2008; Wang et al., 2012). For this study, to investigate the interactions of paired vessels, coherence analysis was employed as an indicator of functional interactions and indicator of how well the seed vessel corresponds to other vessel voxels at different frequency ranges. The definition of coherence is as follows:

$$Coh_{xy}(f) = \frac{\left|P_{xy}(\mathrm{f})\right|^2}{P_{xx}(f)P_{yy}(f)}$$

where x indicates the fMRI signal from one seed vessel, y represents the fMRI time course from another vessel. $P_{xx}(f)$ and $P_{yy}(f)$ are the power spectral densities of x and y, respectively, and $P_{xy}(f)$ is the cross power spectral density of x and y. The coherence was calculated by using Welch's overlapped averaged periodogram method with FFT (256-point length) and a 256 s Hamming window, which divides x and y into equal overlapping sections (240-point overlap, >90% overlap). The frequency resolution of coherence is 1 / 256 s = 0.0039 Hz which provides enough resolution to observe the slow frequency range.

The calcium data analysis

The calcium signal was down-sampled to one TR per sample. Next, zero-phase digital filtering (0.01 - 0.1 Hz) was employed to obtain the slow fluctuation of the calcium signal (filtfilt function in MATLAB). In addition, a cross-correlation between the slow fluctuation of the calcium signal and individual venules was performed using the MATLAB function xcorr (Figures 4E and 4L). A 3ddelay function from the AFNI library was utilized to estimate the time lag map between the slow fluctuation of the calcium signal with BOLD fMRI of venules (CC > 0.25) (Figure 4C, inset) or CBV fMRI of arterioles (CC < −0.25) (Figure 4J, inset). For the spectrogram of the calcium signal, a function timefreq from EEGLAB (Delorme and Makeig, 2004) was employed to get the averaged power of the spontaneous calcium spikes (Figures 5B and 6A). A time-varying power spectrogram of calcium signal was computed by using the discrete Fourier transform with a sliding Humming window. The sliding window was 1000 ms without overlap to match one TR of BOLD fMRI data.

Immunohistochemistry

After the conclusion of the fMRI experiments, the rat brain tissues were perfused using a 4% paraformaldehyde fixative. The tissues were then transferred the to 15% sucrose in PBS and keep overnight at 4°C. Next, the prefixed tissues were moved to 30% sucrose in PBS. After sinking, the tissues were stored at −80°C until use. The tissues were also utilized to prepare coronal sequential brain sections (30-μm thickness, −20°C using Leica CM3050S microtome). The sections were incubated overnight at 4°C with primary antibodies: mouse anti-NeuN (1:200; Merck). Afterward, sections were washed five times with PBS and incubated for 60 min with the secondary antibodies: goat anti-mouse conjugated with CY3 (1:500; Abcam). Finally, mounting medium with DAPI (VectaShield, vector) was utilized to protect the fluorescence signal and reveal nuclei. The expression position of GCaMP was confirmed by colocalization with NeuN using a fluorescence microscope (ApoTome, Zeiss).

Please cite this article in press as: He et al., Ultra-Slow Single-Vessel BOLD and CBV-Based fMRI Spatiotemporal Dynamics and Their Correlation with Neuronal Intracellular Calcium Signals, Neuron (2018), https://doi.org/10.1016/j.neuron.2018.01.025

QUANTIFICATION AND STATISTICAL ANALYSIS

A paired Student's ttest was performed to compare the coherence values of paired venules/veins and paired arterioles/arteries in the rat and human resting-state fMRI data. The data with error bars are displayed as the means ± SEM. The p values < 0.05 were considered statistically significant. The sample size for animal experiments was not previously estimated. The sample size for human experiments was estimated based on the statistical parameters derived from the animal data using G* power analysis. No blinding and randomization design was needed in this work.

Neuron, Volume *97*

Supplemental Information

Ultra-Slow Single-Vessel BOLD and CBV-Based fMRI Spatiotemporal Dynamics and Their Correlation with Neuronal Intracellular Calcium Signals

Yi He, Maosen Wang, Xuming Chen, Rolf Pohmann, Jonathan R. Polimeni, Klaus Scheffler, Bruce R. Rosen, David Kleinfeld, and Xin Yu

Supplementary information

Title: Ultra-slow single vessel BOLD and CBV-based fMRI spatiotemporal dynamics and their correlation with neuronal intracellular calcium signals

Authors: Yi He, Maosen Wang, Xuming Chen, Rolf Pohmann, Jonathan R. Polimeni, Klaus Scheffler, Bruce R. Rosen, David Kleinfeld and Xin Yu*

Supplementary Figures: 10

Supplementary Table: 3

Supplementary Movies: 5

Corresponding Author: Xin Yu

Email: xin.yu@tuebingen.mpg.de

Address: Max-Planck-Ring 11, 72076 Tuebingen Germany

Phone: +49 7071 601-740

Fax: +49 7071 601-701

Supplementary Figures (10)

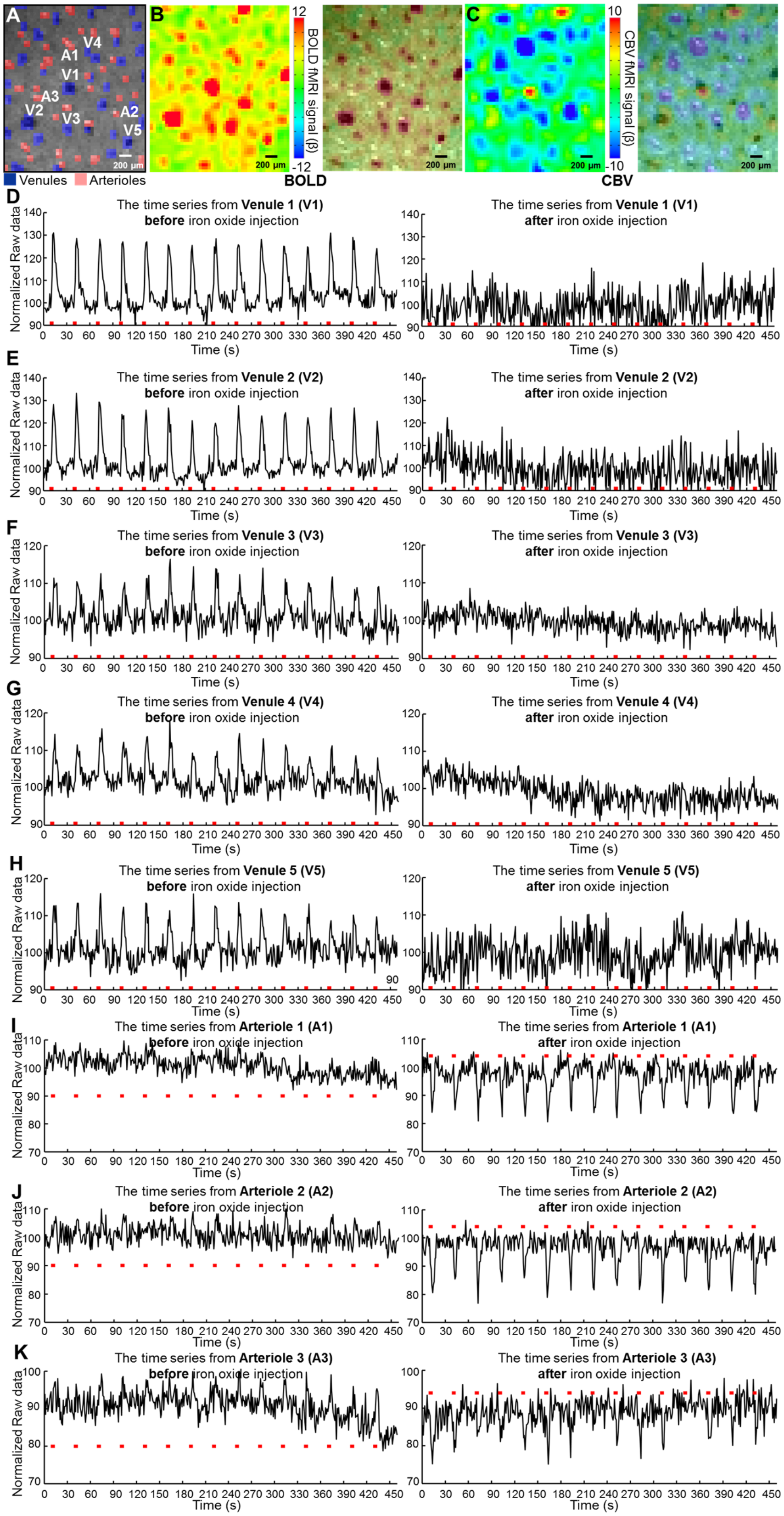

Figure S1. The bSSFP fMRI time courses of individual venules and arterioles before and after iron oxide particle injection (Related to Figure 1) (A) The A-V map shows the five venules and three arterioles. **(B)** The single-vessel bSSFP BOLD functional map (semi-transparent map on A-V map). **(C)** The single-vessel bSSFP CBV-weigthed functional map (semi-transparent map on A-V map **(D-H)** The time course of BOLD and CBV-weighted fMRI signal from five venules (V1-V5). **(I-K)** The time course of BOLD and CBV-weighted fMRI signal from three arterioles (A1-A3).

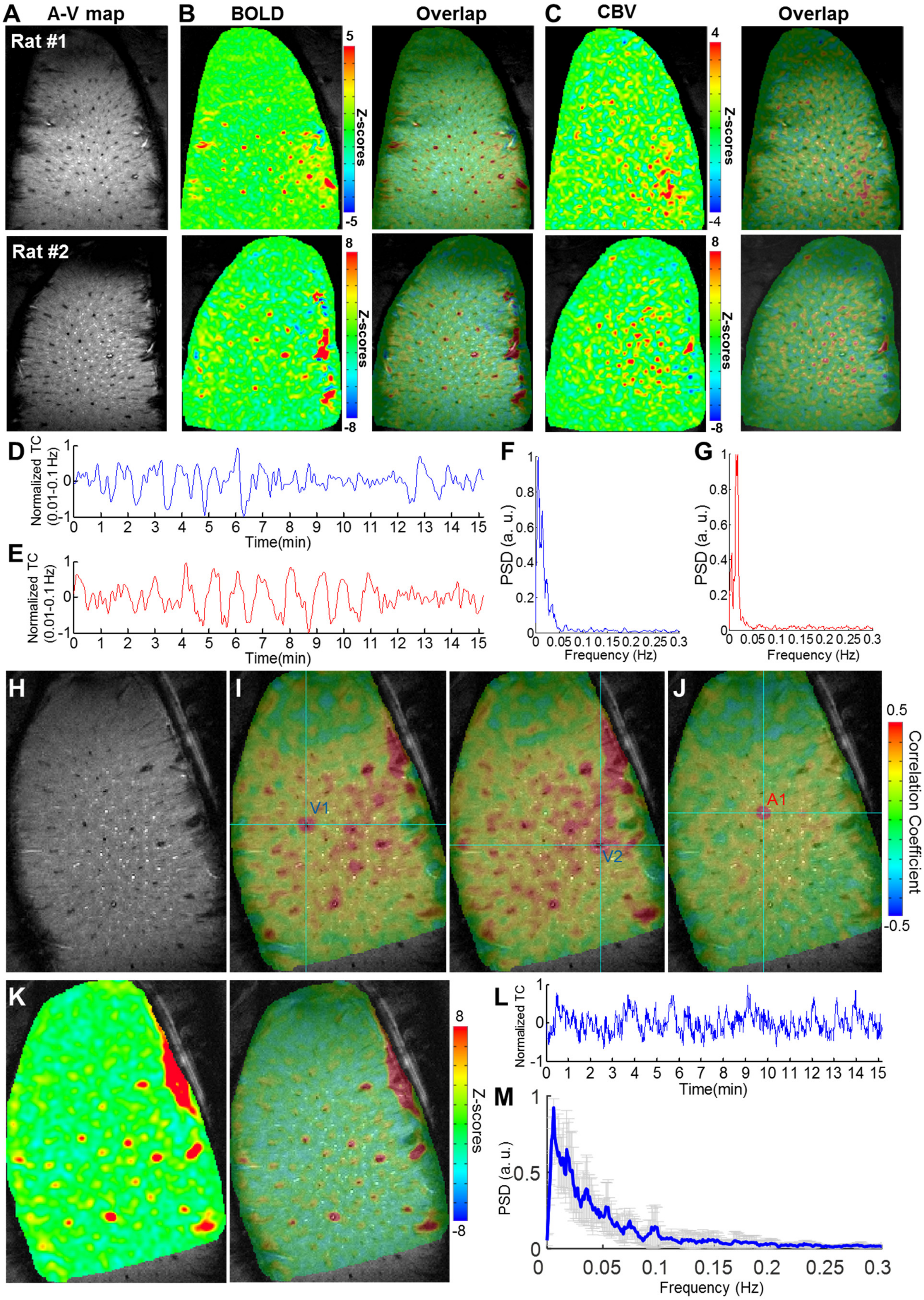
A
A-V map
B
BOLD
Overlap
C
CBV
Overlap
Rat #1
Rat #2
5
-5
Z-scores
4
-4
8
-8
D
E
Normalized TC (0.01-0.1 Hz)
Time(min)
0 1 2 3 4 5 6 7 8 9 10 11 12 13 14 15
F
G
PSD (a. u.)
Frequency (Hz)
0 0.05 0.1 0.15 0.2 0.25 0.3
H
I
V1
V2
J
A1
0.5
-0.5
Correlation Coefficient
K
L
Normalized TC
M
PSD (a.u.)

Figure S2. Part 1: Vascular dynamic network connectivity using Group ICA Analysis in two representative Rats. (Related to Figure 2-3) (A) The A-V maps of two representative Rats. **(B)** The correlation maps based on the designated ICA component show the venule-dominated BOLD correlation pattern in both rats (right panel, the correlation map overlapped on the A-V map). **(C)** The correlation maps based on the designated ICA component demonstrate the arteriole-dominated CBV correlation pattern in both rats (right panel, the correlation map overlapped on the AV map). **(D)** The BOLD time series of the designated ICA component showing high correlation on venule voxels in the rat #2. **(E)** The CBV time series of the designated ICA component indicating high correlation on arteriole voxels in the rat #2. **(F)** The power spectral density (PSD) of the designated ICA component for the BOLD fMRI signal from rat #2 exhibits slow fluctuations of BOLD fMRI from venule voxels vary from 0.01 to 0.04 Hz. **(G)** The power spectral density of the designated ICA component for the CBV fMRI signal from rat #2.

Part 2: Mapping the Vascular dynamic network connectivity under isoflurane anesthesia. (Related to Figure 2-3) (H) The A-V map shows the individual arterioles (bright dots) and venules (dark dots). **(I)** The venule-seed based correlation map from two venule seed voxels (seeds: cyan crosshairs) **(J)** The arteriole-seed based correlation map from one arteriole seed (seed: cyan crosshair). **(K)** The correlation maps based on the designated ICA component show the venule-dominated BOLD correlation patterns (right panel, the correlation map overlapped on the A-V map). **(L)** The normalized BOLD time series of the designated ICA component. **(M)** The power spectral density (PSD) of the designated ICA time series from 3 rats. (n = 3 rats, mean± s.e.m)

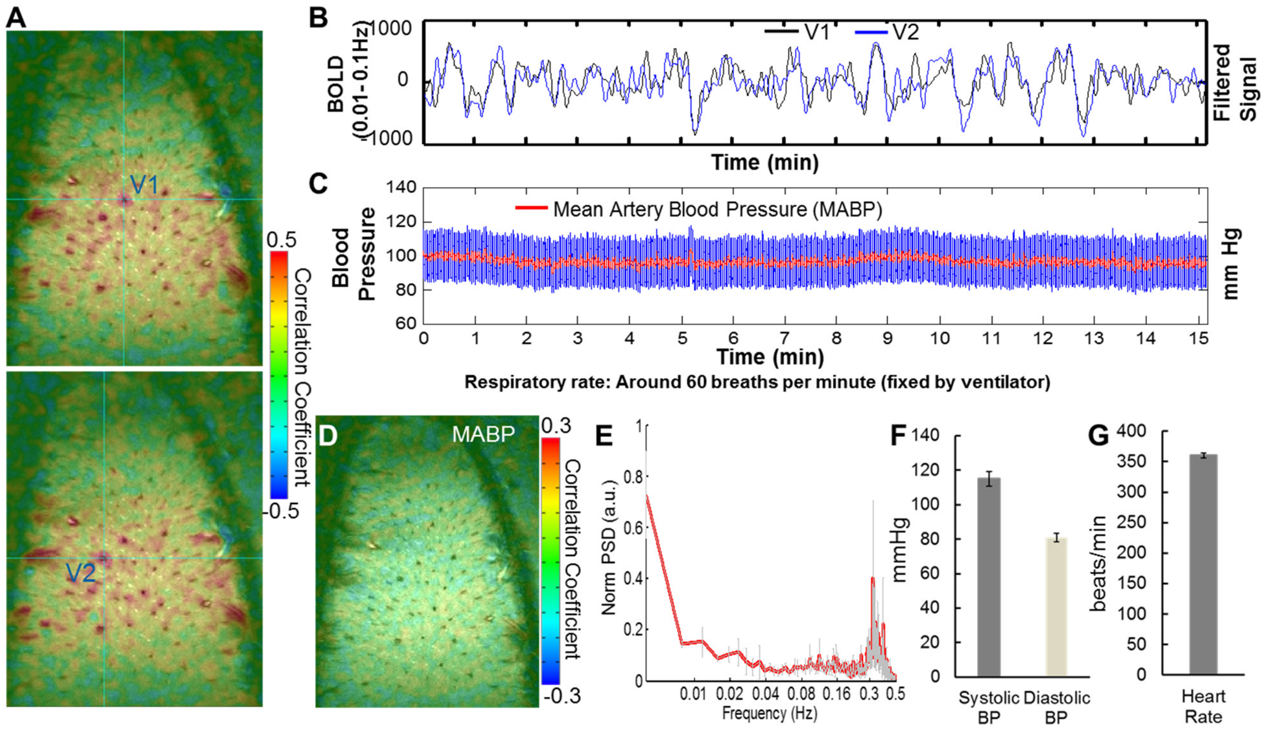

Figure S3. The simultaneously acquired physiological signals and the resting state SSFP-fMRI signal under α-chloralose anesthesia. (Related to Figure 3, STAR Methods) (A) The venule-seeds based correlation maps from two venule seed voxels (V1 and V2). **(B)** The time series of the BOLD signal slow fluctuations (0.01 - 0.1 Hz) from the two venule seeds. **(C)** The blood pressure signals were acquired simultaneously with the resting state fMRI, showing no clear variation correlated to the slow-frequency oscillations of the fMRI signal. **(D)** The correlation map between the mean artery blood pressure (MABP) time series (0.01 - 0.1 Hz) with rs-fMRI shows little correlation. **(E)** The mean normalized power spectral density (PSD) of MABP (n = 3 rats, mean± s.e.m, Welch's method, FFT length = 256, the overlap: 50 %). (**F)** The systolic BP (115.1 ± 4.2 mmHg) and the diastolic BP (81.1 ± 2.4 mmHg) from 6 rats **(G)** The heart rate (360.3 ± 6.6 beats/min) from 6 rats (n = 6 rats, mean ± s.e.m.)

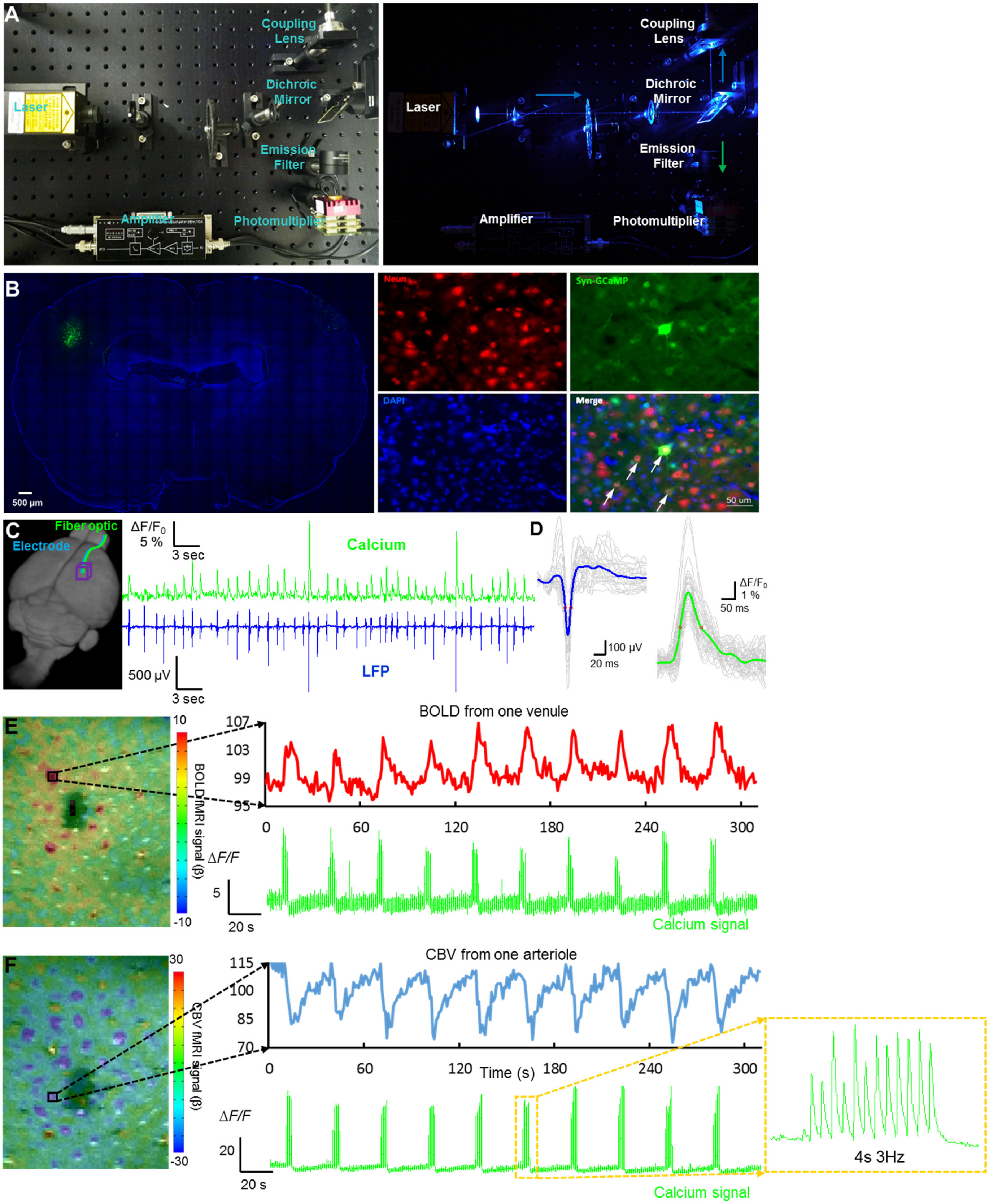
A
Coupling Lens
Dichroic Mirror
Laser
Emission Filter
Amplifier
Photomultiplier
Coupling Lens
Dichroic Mirror
Laser
Emission Filter
Amplifier
Photomultiplier
B
500 µm
NeuN
Syn-GCaMP
DAPI
Merge
50 um
C
Fiber optic
Electrode
ΔF/F0
5 %
3 sec
Calcium
500 µV
3 sec
LFP
D
100 µV
20 ms
ΔF/F0
1 %
50 ms
E
BOLD from one venule
10
-10
BOLD fMRI signal (β)
107
103
99
95
0
60
120
180
240
300
ΔF/F
5
20 s
Calcium signal
F
CBV from one arteriole
30
-30
CBV fMRI signal (β)
115
100
85
70
0
60
120
Time (s)
180
240
300
ΔF/F
20
20 s
4s 3Hz
Calcium signal

Figure S4. *In vivo* fiber optical calcium recording with simultaneous local field potential (LFP) recording. (Related to Figure 4) (A) The setup for the fiber-optic mediated florescent signal recording system. **(B)** The GCamp6f was expressed in the deep layer of the vibrissa cortex (left panel: the green region in the coronal section of the rat brain). Right panel is the enlarged immunostaining image with the NeuN in red, DAPI in blue, and GCaMP6f in green, which were merged to show the GCaMP6f expressed in neurons with NeuN positive stating in the nuclei (white arrows). **(C)** The left panel is the schematic drawing to show the fiber optic and electrode targeting the barrel cortex of a reconstructed 3D rat brain. The right panel shows the simultaneous acquired calcium and LFP signal traces. There is one-to-one correspondence between spontaneous calcium (green) and LFP spikes (blue). **(D)** The averaged LFP spike (blue, Full width at half maximum (FWHM): 10.89 ± 0.58 ms, mean ± s.e.m, n = 30) and the averaged calcium spike (green, FWHM: 78.9 ± 0.26 ms, mean ± s.e.m, n = 48). **(E)** The BOLD fMRI map is overlaid on the A-V map, showing the venule-dominated peak BOLD signal (dark hole, fiber optic). The on/off block time series (red) of BOLD fMRI signal from one single venule ROI (marked in the left panel) and the calcium signal (green) was recorded simultaneously (forepaw stimulation: 3 Hz, 4 s, 1.5 mA). **(F)** The CBV fMRI map is overlaid on the A-V map, indicating the arteriole-dominated peak CBV signal. The on/off block time series (blue) of the CBV fMRI signal from one single arteriole ROI (marked in left panel). The simultaneous calcium signal was recorded with an enlarged image, showing the evoked calcium spikes upon stimulation.

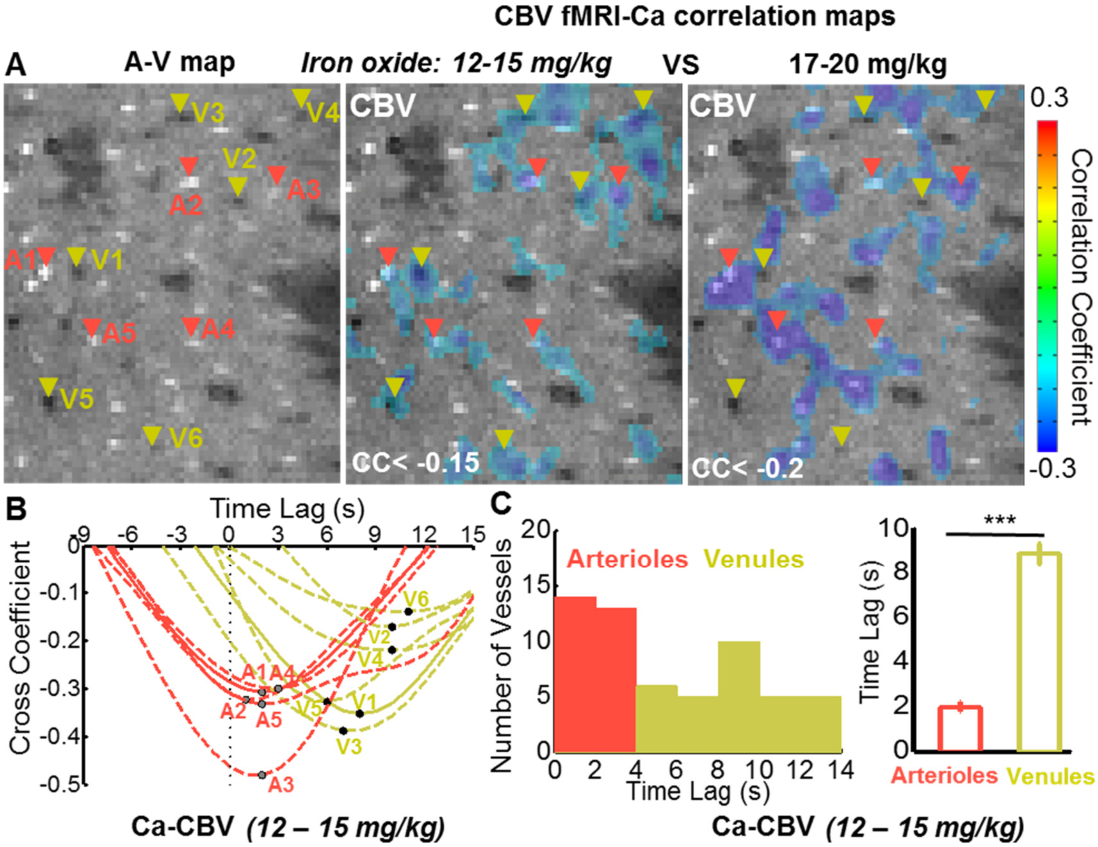

Figure S5. The correlation analysis of the venule CBV fMRI signal with the calcium signal. (Related to Figure 4) (A) The A-V map (the left panel) shows the location of five representative arterioles (A1 - A5) and six representative venules (V1 - V6). The correlation maps between the calcium signal and the SSFP-based CBV fMRI signal acquired at two different dosage of iron oxide particles show negative correlation in the venule voxels (V1 - V6) detectable at low dose (middle panel, 12 - 15 mg/kg), and arteriole dominated negative correlation with increased iron particle concentration (right panel, 17-20 mg/kg). **(B)** At the lower dose of iron oxide particles, the cross-correlation function of the calcium signal and CBV fMRI signal demonstrate the negative peak of the venules (V1 - V6) coefficients at the lag time 6 - 12 s and the negative peak of the arterioles (A1 - A5) at the lag time 1-3 s. **(C)** The histogram of the number of vessels with lag times varied from 0.5 to 14 s (the threshold of the cross-correlation coefficient < -0.15). The mean lag time of arterioles are significantly lower than that of venules at the lower dose of iron oxide particles (***, $p = 5 \times 10^{-18}$, t-test, Arterioles, n = 28 from 4 rats, 1.96 ± 0.22 s; Venules, n = 31 from 4 rats, 8.88 ± 0.48 s, mean ± s.e.m)

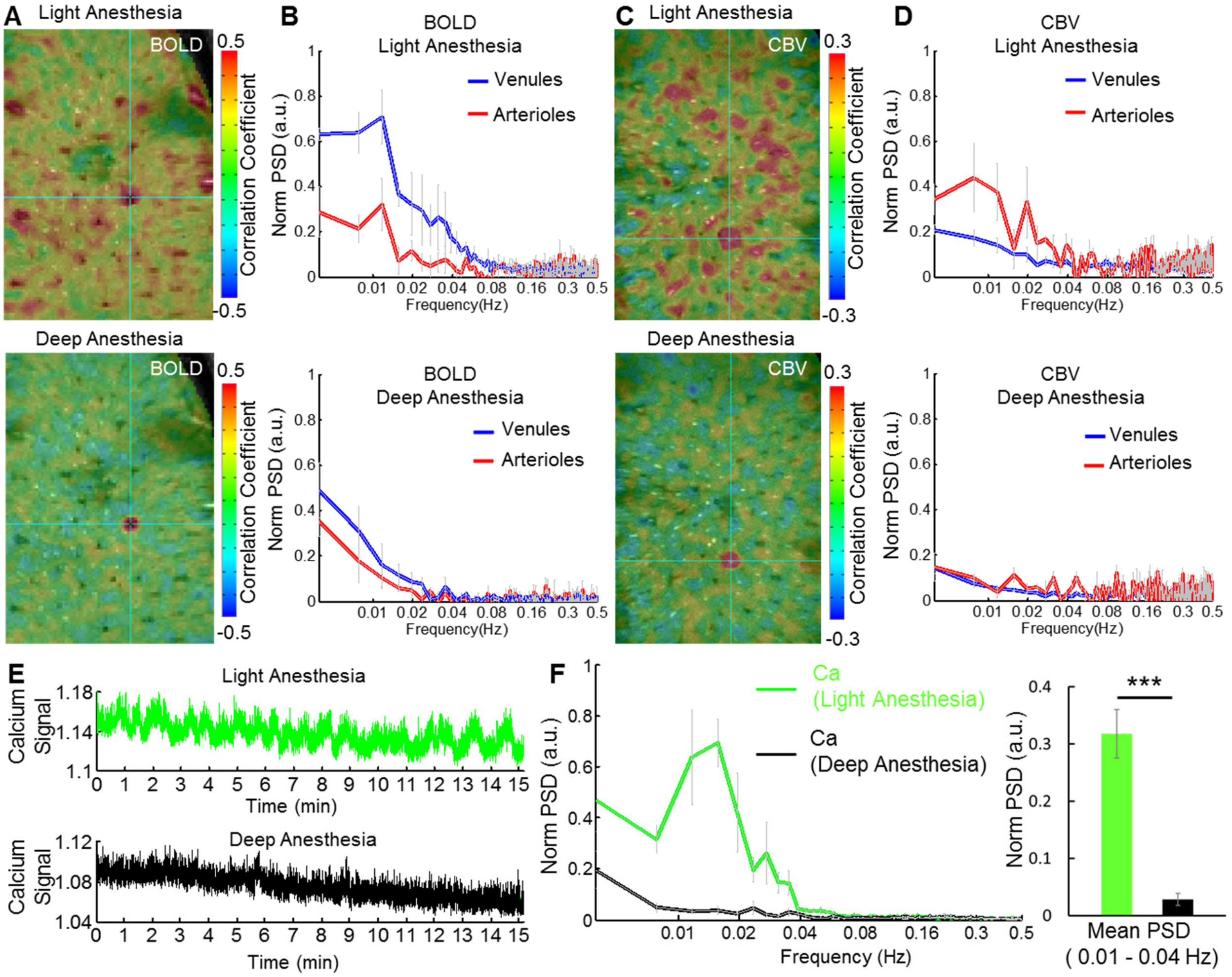

Figure S6. Mapping the vessel-specific fMRI signal fluctuation with simultaneous calcium recording at different anesthetic levels. (Related to Figure 3-6) (A) The venule-seed based BOLD correlation maps under light (upper panel) / deep (lower panel) anesthesia. **(B)** The normalized power spectral density (PSD) of venule (blue) and arteriole (red) voxels of BOLD fMRI under the light (upper panel) and deep (lower panel) anesthesia. (Deep, n =4 rats, light, n = 3 rats, mean ± s.e.m, FFT length = 256) **(C)** The arteriole-seed based CBV correlation maps under light (upper panel) / deep (lower panel) anesthesia. **(D)** The normalized power spectral density (PSD) of venule (blue) and arteriole (red) voxels of CBV fMRI under the light (upper panel) and deep (lower panel) anesthesia. (n = 3 rats, mean ± s.e.m, FFT length = 256) **(E)** The raw calcium signal simultaneously acquired with the rs-fMRI signal shows slow oscillation under the light anesthesia (upper panel, green curve), but not under the deep anesthesia (lower panel, black curve). **(F)** The normalized PSD of the calcium signal shows elevated power at the frequency bandwidth 0.01-0.04 Hz under light anesthesia, which is significantly higher than that under deep anesthesia. (***, p= 0.00047, paired t-test, n =5 rats, mean ± s.e.m, Welch's method, FFT length = 256, the overlap: 50 %).

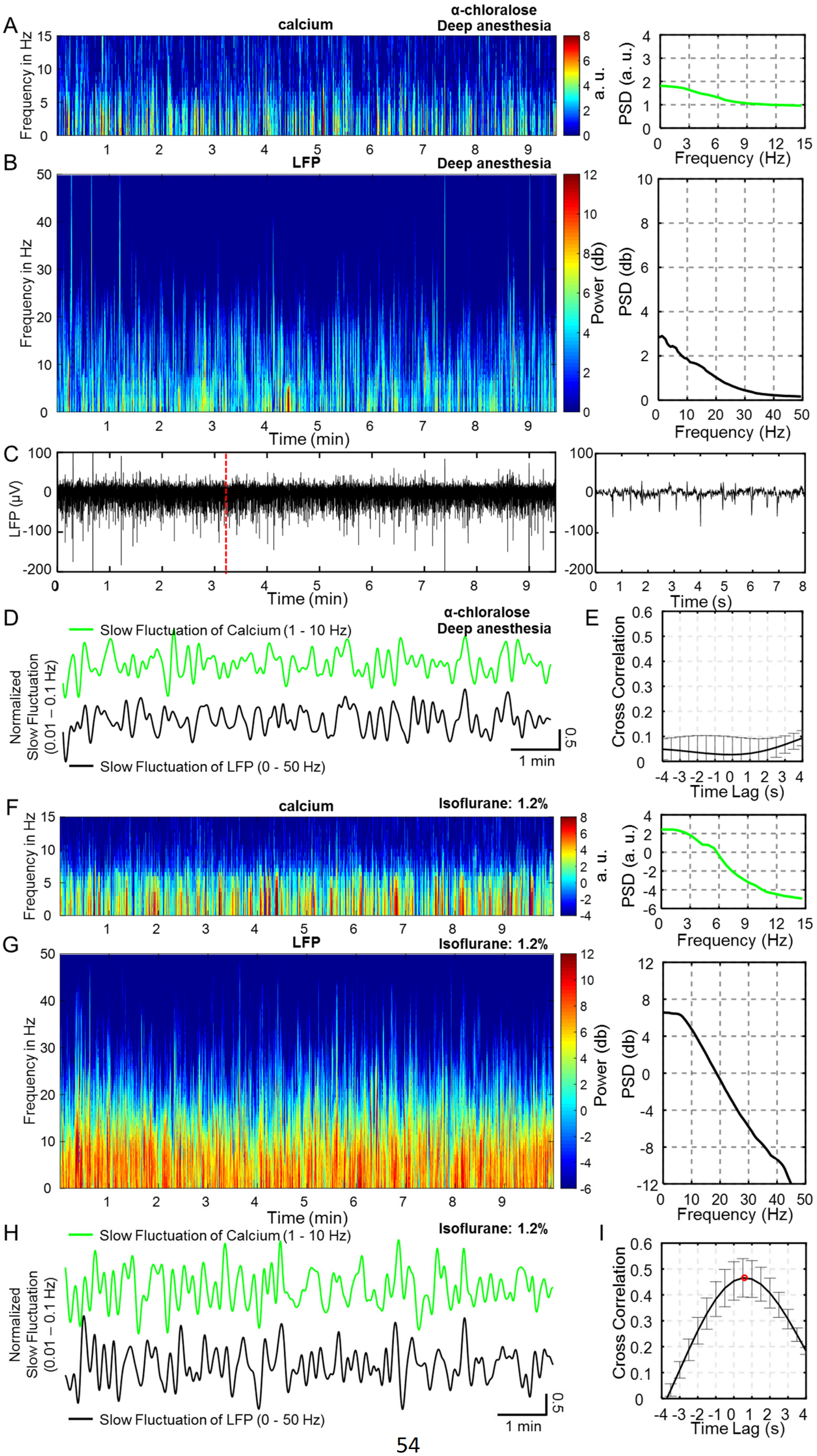
A
calcium
α-chloralose
Deep anesthesia
Frequency in Hz
a. u.
PSD (a. u.)
Frequency (Hz)
B
LFP
Deep anesthesia
Frequency in Hz
Power (db)
PSD (db)
Time (min)
Frequency (Hz)
C
LFP (μV)
Time (min)
Time (s)
D
Slow Fluctuation of Calcium (1 - 10 Hz)
α-chloralose
Deep anesthesia
Normalized
Slow Fluctuation
(0.01 – 0.1 Hz)
0.5
1 min
Slow Fluctuation of LFP (0 - 50 Hz)
E
Cross Correlation
Time Lag (s)
F
calcium
Isoflurane: 1.2%
Frequency in Hz
a. u.
PSD (a. u.)
Frequency (Hz)
G
LFP
Isoflurane: 1.2%
Frequency in Hz
Power (db)
PSD (db)
Time (min)
Frequency (Hz)
H
Slow Fluctuation of Calcium (1 - 10 Hz)
Isoflurane: 1.2%
Normalized
Slow Fluctuation
(0.01 – 0.1 Hz)
0.5
1 min
Slow Fluctuation of LFP (0 - 50 Hz)
I
Cross Correlation
Time Lag (s)

Figure S7. Part 1: The Spectrogram of simultaneous calcium and electrophysiological signal under α-chloralose anesthesia (Related to Figure 4-6) (A) Spectrogram of calcium signal during deep anesthesia. **(B)** Spectrogram of local field potential (LFP) at deep anesthesia from multi-taper spectral estimates (1s sliding window with 0.1s steps, 9 tapers). The right panel shows the averaged power spectral density (PSD). **(C)** The time course of the LFP signal under deep anesthesia **(D)** The mean calcium spectral power profile (band-pass filter: 0.01 - 0.1 Hz of 1 - 10 Hz, green) and the mean LFP spectral power profile (0 - 50 Hz, black) at deep anesthesia. **(E)** The cross-correlation function of the averaged LFP power (0 - 50 Hz) from LFP spectrogram and the averaged calcium power (1 - 10 Hz) profile from the calcium spectrogram (band-pass filter with 0.01 - 0.1 Hz) show little correlation at deep anesthesia (n = 4 rats, mean ± s.e.m).

Part 2: The spectrogram of simultaneous calcium and electrophysiological signal under 1.2% isoflurane anesthesia (Related to Figure 4-6). (F) The spectrogram of the calcium signal under isoflurane. **(G)** The spectrogram of local field potential (LFP) from multi-taper spectral estimates (1s sliding window with 0.1s steps, 9 tapers). The right panel shows the averaged power spectral density (PSD) **(H)** The slow fluctuation (band-pass filter: 0.01 - 0.1 Hz) of the mean calcium spectral power profile (1 - 10 Hz, green) and the mean LFP spectral power profile (0 - 50 Hz, black). **(I)** The cross-correlation function of the averaged LFP power (0 - 50 Hz) from LFP spectrogram and the averaged calcium power (1 - 10 Hz) profile from the calcium spectrogram (band-pass filter with 0.01 - 0.1 Hz) illustrates strong correlations during 1.2 % isoflurane anesthesia (n = 3 rats, mean ± s.e.m).

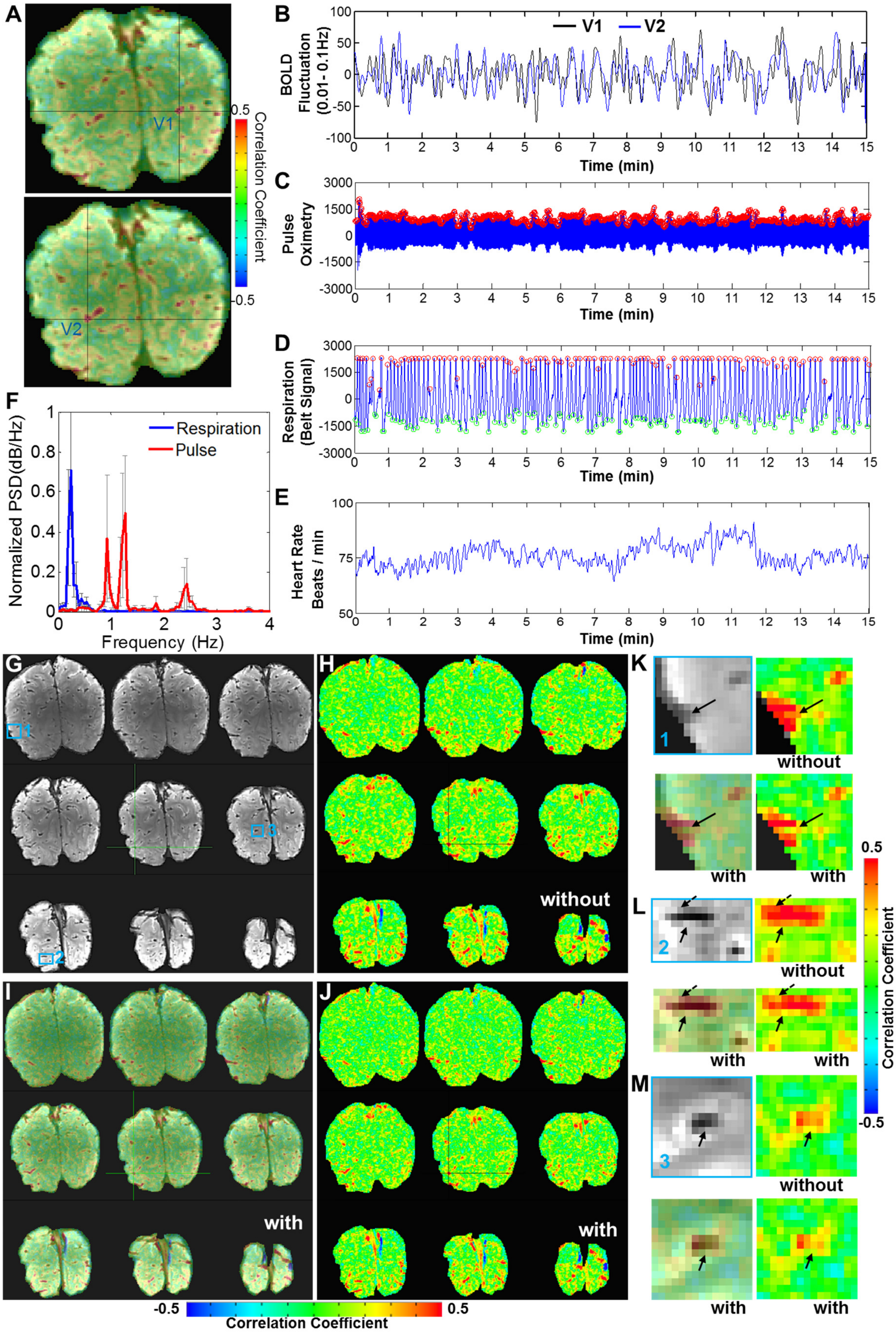
A
V1
V2
0.5
-0.5
Correlation Coefficient
B
BOLD Fluctuation (0.01- 0.1Hz)
V1
V2
100
50
0
-50
-100
0 1 2 3 4 5 6 7 8 9 10 11 12 13 14 15
Time (min)
C
Pulse Oximetry
3000
1500
0
-1500
-3000
Time (min)
D
Respiration (Belt Signal)
3000
1500
0
-1500
-3000
Time (min)
E
Heart Rate Beats / min
100
75
50
Time (min)
F
Normalized PSD(dB/Hz)
Respiration
Pulse
1
0.8
0.6
0.4
0.2
0
0 1 2 3 4
Frequency (Hz)
G
1
2
3
H
without
I
with
J
with
K
1
without
with
with
L
2
without
with
with
M
3
without
with
with
0.5
-0.5
Correlation Coefficient
-0.5
0.5
Correlation Coefficient

Figure S8. Part 1: The simultaneously recorded physiologic parameters for the resting-state fMRI of human subjects. (Related to Figure 7) (A) The seed-based correlation maps from two vein voxels (V1 and V2). **(B)** The time series of BOLD signal (0.01 - 0.1 Hz) from the two representative vein seeds are highly correlative. (V1, black line; V2, blue line) **(C-E)** The pulse oximetry (**C**), respiration (**D**) signals were simultaneously acquired with the BOLD fMRI signal by using Siemens physiologic monitoring unit (PMU). Heart rate (**E**) is derived from the pulse-oximetry time series. **(F)** The normalized power spectral density (PSD) represents the respiration signal (blue) with peak frequency at approximately 0.18 Hz and the pulse oximetry signal (red) covering the frequency range from 0.8 to 2.5 Hz (n = 3 subjects, mean ± s.e.m).

Part 2: The correlation maps with/without the regression of the physiological parameters. (Related to Figure 7) (G) The averaged multi-slices EPI images covering the occipital lobe of the human brain. **(H)** The seed-based correlation maps before the physiological parameter regression (seed: black cross-point). **(I-J)** The seed-based correlation maps after the physiological parameter regression (seed: black cross-point; (**I**) is the semi-transparent map overlapped on the EPI images.) **(K-M)** The enlarged views of three regions in multi-slices EPI images (blue square marks in **G**) illustrate the similar correlation patterns with/without the regression of the physiological parameters.

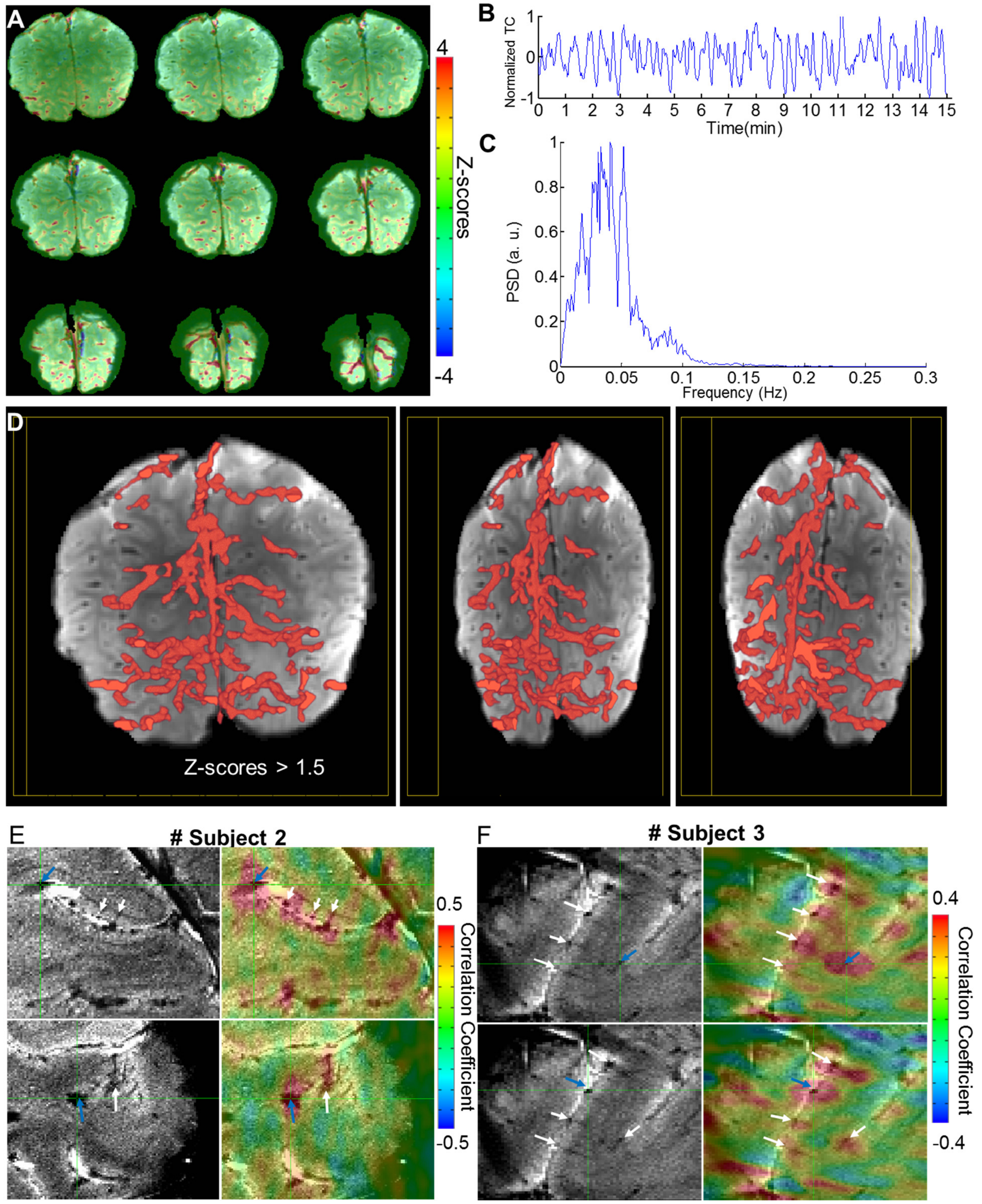

Figure S9. Part 1: The ICA-based vascular dynamic network connectivity mapping. (Related to Figure 7) (A) The correlation maps of the designated ICA component demonstrate venule voxels with highest correlation at multiple slices from one representative human subject. **(B)** The time series of the designated ICA component displaying the slow oscillation temporal feature. **(C)** The power spectral density (PSD) of the designated ICA component. **(D)** The 3D views of the reconstructed vascular dynamic network connectivity maps highlight the correlated cerebral vasculature at different angles ($z > 1.5$).

Part 2: The intracortical vascular dynamic mapping with 9.4T on the other representative subjects (Related to Figure 8) (E-F) Seed-based correlation maps based from intra-cortical venous voxels show highly correlated voxels on the other intracortical veins (white arrows) in the gray matter from Subject 2 (**E**) and Subject 3 (**F**).

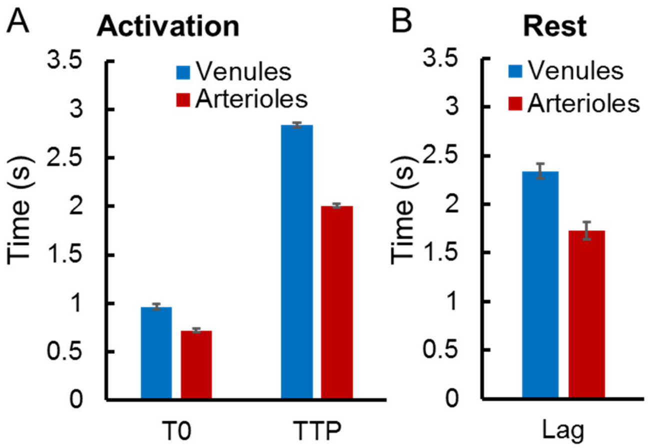

Figure S10. The transit time during activation and resting state (Related to Figure 4) A. The onset time (T0), time to peak (TTP) of BOLD from venules and CBV from arterioles during activation. (Data from the previous work (Yu et al., 2016)) **B.** The lag time of cross-correlation between the calcium signal and vessel-specific fMRI.

Supplementary Tables

	Rat #1	Rat #2	Rat #3	Rat #4	Rat #5	Rat #6	Rat #7	Rat #8
Arterioles	95	66	93	87	52	99	82	83
Venules	104	95	111	87	80	115	86	93
A-V ratio	0.85 ± 0.04							

Table S1. (Related to Figure 1-2) The number of cortical arterioles and venules in rat brain.

	Activation		**Resting State (s)**
	T0 (s)	**TTP (s)**	
Arterioles	0.719 ± 0.021	2.216 ± 0.048	1.727 ± 0.086
Venules	0.963 ± 0.029	2.868 ± 0.049	2.339 ± 0.073
The transit time	0.244	0.652	0.612

Table S2. (Related to Figure 4) The transit time during activation and resting state. (Activation: Arterioles, n = 61 from 5 rats, Venules, n = 69 from 5 rats; Resting State: Arterioles, n = 136 from 4 rats, Venules, n = 297 from 7 rats)

Anesthesia Type	α-chloralose anesthesia	isoflurane anesthesia
Figures	Figure 1-6, Figure S1, Figure S2A-G, Figure S3-S5, Figure S6A-E, Figure S7	Figure S2H-M, Figure S6F-I

Table S3. (Related to Figure 1-6) The anesthetic regimen in the results

Supplementary Movie Legends

Movie S1: The seed-based bSSFP BOLD rs-fMRI in the anesthetized rat brain. (Related to Figure 2)
The white arrow indicates the location of the seed (radius: 150 μm). When the seed is moved to dark dots (venule voxels), most venule voxels are highly correlated but less so for arteriole voxels.

Movie S2: The seed-based bSSFP CBV rs-fMRI in the anesthetized rat brain. (Related to Figure 2)
The white arrow indicates the position of the seed (radius: 150 μm). When the seed is moved to bright dots (arteriole voxels), most arteriole voxels are highly correlated but less so for venule voxels.

Movie S3: The evoked BOLD fMRI signal with voxel-wise time courses in the human brain. (Related to Figure 5)
With the visual stimulation (8 Hz checkerboard stimulation), the voxel-wise BOLD fMRI signal changes (left panel) are shown from 5 x 5 voxel matrix covering one individual vein through sulcus (the dark voxel in the green square, middle panel). The red cursor in the time course is corresponding to the color-coded BOLD functional movie time (right panel).

Movie S4: The seed-based rs-fMRI in the human brain. (Related to Figure 5)
The white arrow indicates the location of the seed (radius: 1 mm). The seed-based correlation maps by the resting-state fMRI demonstrates vein-dominated correlation spatial patterns.

Movie S5: Vascular dynamic network connectivity using ICA Analysis in human at resting state. (Related to Figure 5)
The left panel exhibits the ICA-based correlation maps with the averaged EPI images as the background (dark voxels as veins). The video demonstrates the highly correlated venous voxels at multiple slices, showing a 3D vascular dynamic correlation structure (Z-scores > 1.5) through the main branches of the cerebral vasculature.